Universidade do Minho
Escola de Engenharia

José Pedro Oliveira Fernandes

Developing an Ultrasound-based Water Treatment System

Outubro de 2023

Developing an Ultrasound-based Water Treatment System

José Pedro Oliveira Fernandes

UMinho | 2023

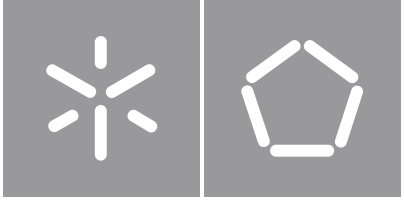

Universidade do Minho
Escola de Engenharia

José Pedro Oliveira Fernandes

Developing an Ultrasound-based Water Treatment System

Dissertação de Mestrado
Mestrado em Engenharia Mecânica
AE Sistemas Mecatrónicos

Trabalho efetuado sob a orientação do
Professor Doutor Hélder Jesus Fernandes Puga
Professor Doutor Paulo Jorge Ramisio Pernagorda

Outubro de 2023

DIREITOS DE AUTOR E CONDIÇÕES DE UTILIZAÇÃO DO TRABALHO POR TERCEIROS

Acknowledgments

I extend my deepest gratitude to all those who played a direct or indirect role in my academic journey.

To my family, whose unwavering support and unshakable belief in me have been my cornerstone. To my father, whose guidance, impassioned conversations about mechanical intricacies, and status as my initial muse upon hearing the word "mechanic" shaped my path.

To my brother, a perpetual source of youthful exuberance and, paradoxically, my primary motivation to strive for a brighter, better world. I hope I'm setting an example worth following. Live and enjoy.

To my grandparents, for nourishing me both physically and emotionally, and for being a steadfast presence even on the gloomiest or most stressful days.

To Bia, an inspiring figure to emulate, the Picasso of the graphic design, the most critical person and, the future's most annoying teacher.

To all my friends, thank you for sharing in every high and low, for the countless gatherings, melodies, and conversations that defined this journey.

To Bruno, Dário, and Tiago, my trusted mechanical comrades for the past five years, thank you for being my confidants and companions.

A heartfelt acknowledgment to my Society Loving the Planet Minho, for providing not only camaraderie but also purpose, and a platform for environmental consciousness at the University of Minho.

To all the players I had the privilege of coaching, who provided a welcome escape from the rigors of university life, I extend my heartfelt gratitude. Thank you for allowing me to be a part of your journey.

To Diogo, Grilo, and Inês, for their invaluable assistance and camaraderie in the laboratory these past six months. Grilo thank you for being always there to help.

A special mention to the laboratory technicians and researchers, particularly Catarina, Filipe, Marcos, Miguel, Sérgio, and Sónia, for their support and expertise.

To the University of Minho, the researchers, professors, and sponsors involved in the Res4Valor project, my heartfelt thanks.

To the Department of Textile Engineering, for the provision of ultra-filtrated water.

To Professor Vítor Monteiro for his invaluable electronic support.

To all the teachers from whom I had the privilege of learning

To my supervisors, Hélder Puga and Paulo Ramísio, you have not only been fountains of wisdom but also exceptional guides.

And finally, to the most vibrant butterfly and the brightest star in the night sky, it is done. I made it.

STATEMENT OF INTEGRITY

I hereby declare having conducted this academic work with integrity. I confirm that I have not used plagiarism or any form of undue use of information or falsification of results along the process leading to its elaboration.

I further declare that I have fully acknowledged the Code of Ethical Conduct of the University of Minho.

Abstract

This dissertation examined the effects of ultrasound in different stages of a Wastewater Treatment Plant (WWTP), focusing on adsorption and oxidation processes. Additionally, it provided guidance for the proper design of an ultrasound-assisted equipment aimed at water treatment.

Initially, the physical effects of ultrasound treatment on water were explored. The initial understanding of these phenomena guided the research in two distinct directions. On one hand, the feasibility of combining ultrasound treatment with existing adsorption mechanisms was investigated. On the other hand, the potential of this technology in isolation for wastewater treatment was examined.

In the context of wastewater treatment, sensors were developed to monitor acoustic cavitation within the ultrasound equipment. After validating the sizing of this equipment, a study was conducted at a WWTP to evaluate the effectiveness of ultrasound treatment in water contaminated with various pollutants and organisms.

The application of ultrasound proved impactful in the initial moments. When applied to ultra-filtered water, ultrasound treatment (I_s=20.7 $\pm$ 1.6 W·cm^{-2}) in the first 18 seconds resulted in a 2.7-fold increase in ORP and a 2.29-fold reduction in pH.

The combination of ultrasound treatment with the organic compound "Nutrimais da Lipor" in adsorption resulted in a Cu removal rate of 82%, surpassing conventional mechanical action by 4.3 times. The removal of CIP was accelerated, reaching the maximum adsorption capacity (70%) in 1 minute, being 1.75 times more effective than the mechanical approach. With the Kaolin adsorbent, both methods showed comparable results after 1 minute.

Regarding the treatment of contaminated water at the WWTP, the developed sensors for monitoring acoustic cavitation identified cavitation thresholds and transition zones, confirming the geometric dimensions of the ultrasound chamber.

Applying ultrasound treatment with different powers (200 W, 400 W, and 800 W) showed a significant variation in physicochemical parameters in the first 5 minutes, followed by stabilization and return to initial values. COD decreased in the first 2 to 5 minutes, then returned to initial values. These results highlight the potential of ultrasound treatment, especially in the initial stages of application, for accelerating processes and the possibility of integration with other methods.

Keywords Adsorption, Cavitation, Piezoelectric, Ultrasound, Wastewater

Resumo

A presente dissertação analisou os efeitos do ultrassom em diferentes fases de uma Estação de Tratamento de Águas Residuais (ETAR), com foco nos processos de adsorção e oxidação. Além disso, apresentou orientações para a conceção adequada de um equipamento auxiliado por ultrassom.

Inicialmente, exploraram-se os efeitos físicos do tratamento por ultrassons na água. A compreensão inicial desses fenômenos orientou a pesquisa em duas direções distintas. Por um lado, investigou-se a viabilidade da combinação do tratamento por ultrassons com mecanismos já existentes de adsorção. Por outro lado, examinou-se o potencial desta tecnologia, de forma isolada, no tratamento de águas residuais.

No âmbito do tratamento de águas residuais, foram desenvolvidos sensores para monitorizar a cavitação acústica dentro do equipamento de ultrassom. Após validar o dimensionamento deste equipamento, conduziu-se um estudo numa ETAR para avaliar a eficácia do tratamento por ultrassons em água contaminada por diversos poluentes e organismos.

A aplicação do ultrassom mostrou-se impactante nos momentos iniciais. Quando aplicado em água ultrafiltrada, o tratamento por ultrassons (I_s=20.7 $\pm$ 1.6 W·cm^{-2}) nos primeiros 18 segundos provoca um aumento de 2.7 vezes do ORP e numa redução de 2.29 vezes do pH.

A combinação de tratamento por ultrassons com o composto orgânico "Nutrimais da Lipor" na adsorção, resultou numa taxa de remoção de Cu de 82%, superando 4.3 vezes a ação mecânica convencional. A remoção de CIP foi acelerada, atingindo a capacidade máxima de adsorção (70%) num 1 minuto, sendo 1.75 vezes mais eficaz que a abordagem mecânica. Com o adsorvente Caulim, ambos os métodos apresentaram resultados comparáveis após 1 minuto.

Relativamente ao tratamento de água contaminada da ETAR, os sensores desenvolvidos para monitorizar a cavitação acústica permitiram identificar os limiares de cavitação e as zonas de transição, bem como confirmar as dimensões geométricas da câmara de ultrassom.

Aplicando o tratamento por ultrassons com diferentes potências (200 W, 400 W e 800 W), observou-se uma variação acentuada nos parâmetros físico-químicos nos primeiros 5 minutos, seguida de estabilização e retorno aos valores iniciais. A COD diminuiu nos primeiros 2 a 5 minutos, para então retornar aos valores iniciais. Estes resultados destacam o potencial do tratamento por ultrassom, nomeadamente nas fases iniciais de aplicação, no acelerar de processos e na possibilidade de integração com outros.

Palavras-Chave Adsorção, Águas Residuais, Cavitação, Piezoelétrico, Ultrassom

Table of Contents

Acknowledgments ii

Abstract iv

Resumo v

1 Introduction 1

1.1 Contextualization . . . 1
1.2 Motivation . . . 2
1.3 Objectives . . . 3
1.4 Structure of the Dissertation . . . 4

2 State of Art 5

2.1 Wastewater Treatment by Conventional Processes . . . 5
2.1.1 Characterization of Domestic and Industrial Wastewater . . . 5
2.1.2 Emergent Pollutants . . . 9
2.1.3 Wastewater Treatment Plant . . . 10
2.2 Wastewater Treatment by Ultrasound Assisted Systems . . . 17
2.2.1 Coagulation and Flocculation Enhanced by Ultrasound Treatment . . . 18
2.2.2 Adsorption Enhanced by Ultrasound Treatment . . . 19
2.2.3 General Wastewater Treatment Enhanced by Ultrasound . . . 22
2.3 Effects of Cavitation on Wastewater treatment . . . 23
2.3.1 Variables Affecting Sonochemical Reactions . . . 29
2.3.2 Ultrasound Components and Functioning . . . 33
2.3.3 Acoustic Cavitation Characterization . . . 39

3 Development of a Sensor for Characterization of Acoustic Activity 41

3.1 Equipment Design and Integration . . . 41
3.2 Piezoelectric Sensor Setup and Data Analysis . . . 48
3.3 Experimental Conditions . . . 54

4 Experimental Evaluation 59

4.1 Physical Analysis of Ultrasound Action on Water . . . 59

4.1.1 Piezoelectric Calibration and Protective Layer Impact 59
4.1.2 Cavitation Monitorization with Piezoelectric Sensors 63
4.1.3 Resonance Frequency Analysis of Piezoelectric Sensors 76
4.1.4 Ultrasound Effects on Water and Water-Oil Mixture 80
4.2 Ultrasound Effects on Water Characteristics and Adsorption 83
4.2.1 Impact of Ultrasound on ORP and pH 83
4.2.2 Ultrasound Impact on Adsorption Processes 85
4.3 Insights from the Experimental Analysis 90

5 Performance Assessment on a Wastewater Treatment Plant 93
5.1 Experimental Conditions and Setup 93
5.2 Analysis of Ultrasound Treatment Effects on Wastewater Parameters 95

6 Conclusions 105
6.1 Piezoelectric Sensor for Cavitation Characterization 105
6.2 Assessment of Impacts of Ultrasound on Wastewaterw 106
6.3 Future Works 107

References 107

Appendix A - Piezoelectric Datasheet 123

Appendix B - Calibration Extended Data of« Sensors 2 and 3 125

List of Figures

Figure 2.1– Three main groups of possibles wastewater treatment, physical, chemical or biological. During the conventional process, these can be combined between them.. 11

Figure 2.2– Diagram of a WWTP and the primary procedures carried out during each phase of liquid treatment. Image adapted from Shah et *al.* [45]. 12

Figure 2.3– Sequence of coagulation and flocculation as part of wastewater treatment. Image adapted from Teh et *al.* [52] 14

Figure 2.4– Mechanism of adsorption between a liquid and the absorbent. The process is characterize by three main layers: absorbent, adsorbate and absorptive. Image adapted from Ameri et *al.* [58]. 15

Figure 2.5– Water phase diagram. The passage from liquid to vapour can occur by decreasing the pressure like seen in cavitation (1-2) or increasing the temperature (1-3). Image adapted from Franc et *al.* [99]. 24

Figure 2.6– Process of bubble formation and growth in cavitation. Bubble nuclei form, grow, and reach a critical size, causing implosion and fragmentation. This cycle recurs. Image adapted from Ashokkumar et *al.* [103]. 25

Figure 2.7– Impact of the Pressure Variation on the Formation and Growing of Bubbles. The constant compression and rarefaction lead to nucleation, growth by rectified diffusion, ending with the implosion of the bubble. Image adapted from Mason et *al.* [105]. 26

Figure 2.8– Hotspot, gas-liquid interface and bulk solution regions and their characteristics during bubble implosion. Image adapted from Carpenter et *al.* [111]. 28

Figure 2.9– Sequence of Cellular Degradation by Cavitation. It begins with gas cavity formation due to increased water vapour. The ensuing collapse releases destructive radicals, leading to cellular destruction, augmented by mechanical stress from implosion. Image adapted from Fetyan et *al.* [97]. 31

Figure 2.10– Sound range along the spectrum and the position of the different types of ultrasound, low frequency ultrasound, high frequency ultrasound and ultrasonic spectrum used in medical diagnosis. Image adapted from Fetyan et *al.* [97]. 34

Figure 2.11– Typical configuration of an ultrasound device for water treatment application. (a) The ultrasound tip consist of a horn emitting waves perpendicular to the ultrasound axis. Alternatively, it may involve a waveguide and an acoustic radiator. Image adapted from Marin-Hernandez et *al.* [136]. 35

Figure 2.12– Piezoeletric disk response with two different exciting possibilities. Mechanical force yields voltage (direct effect for sensors); applied voltage induces dimensional change (indirect effect for transducers). Image adapted from Sikalidis et *al.* [139]. 37

Figure 3.1– Equipment main components with focus on the exterior section and structural parts. . . 42

Figure 3.2– Part of the equipment responsible for the generation and propagation of the sound waves and respective parts: Piezoeletric transducer, Waveguide, Flange, Booster and Acoustic Radiator. 43

Figure 3.3– System operation with water inlet and outlet for chamber cooling. The treated water outlet can be positioned at the (a) bottom valve if contaminants tend to rise to the surface, or at the (b) top if contaminants tend to settle. 43

Figure 3.4– Design Concept A employs two tubes for wire passage: (a) with a dual entry at the top for chamber access, and (b) a perpendicular tube for wire passage to the piezoelectric sensors. (c) A detailed view emphasizes the connection between the tubes, highlighting the wire passage hole and the superior plate securing the second tube. 45

Figure 3.5– Design Concept B employs a single curved tube for wire passage: (a) entering from the bottom of the cylinder in a straightforward operation, (b) utilizing a double inlet accessory connected with a threaded connection, and (c) establishing the wire connection to the piezoelectric sensors via the superior passage on top of the tube. 46

Figure 3.6– Structural component to guide and attach all the wires from the sensor (a) Specifications for tube dimensions and a technical drawing for manufacturing (b) Wended tube support for the wire passage to the piezoelectric sensors after manufacturing. 47

Figure 3.7– Piezoelectric sensor configuration after polarization. Image adapted from Puga et *al.* [156].. 49

Figure 3.8– Piezoelectric sensors for the acoustic reading with a (a) front view of sensors 1, 2 and 3 and (b) the back view of the three once they have all the same construction.. 49

Figure 3.9– Main Menu for the LabVIEW program with the Start, Help and Exit bottoms.. 50

Figure 3.10– LabVIEW code for the Main Menu with (a) sequence for the access to the Menu Start or Help and (b) for close the program. 51

Figure 3.11– Help Menu with all the explanations for utilization of the program and all the options possible.. 51

Figure 3.12– LabVIEW Code for the Help Menu With Sequences for the Buttons. 52

Figure 3.13– Data Acquisition Menu with the FFT graphic, Impact Load and Voltage acquisition. It is possible to set the recording time, the output file location, number of samples and rate and start and stop the record. 53

Figure 3.14– LabVIEW Code for Data Acquisition in the Recording and Acquisition Menu. 54

Figure 3.15– Test Positions 1 and 2. Position 1 is located at a distance of 50 mm from the water level, while Position 2 is positioned 250 mm above it. The acoustic sensors are fixed to the interior structure. 55

Figure 3.16– Experimental Setup for Impact Test. The positions 'zero' and 'rebounding' are characterized by their respective heights and velocities. Data acquisition from the presented piezoelectric element is facilitated by the NI cDAQ 9172 system connected to the computer. The rebounding height is captured using a slow-motion camera. 56

Figure 3.17– Tension Divider for Tension Reduction: (a) Breadboard utilized for electrical connections. (b) Electrical circuit for the tension divider.. 58

Figure 4.1– Voltage Measurement for Sensor 1 and its Respective Noise Threshold during the calibration process. 59

Figure 4.2– Calibration Curve for Sensor 2 with Voltage Variation in Response to Impact Load. 60

Figure 4.3– Calibration Curve for Sensor 3 with Voltage Variation in Response to Impact Load. 61

Figure 4.4– Voltage as a Function of Impact Load: Sensor 2 exhibits a higher voltage reading for each impact load. However, both sensors display similar temporal behavior, differing primarily in sensitivity.. 62

Figure 4.5– Piezoelectric sensors after 90 seconds of cavitation at varying ultrasound frequencies - from 100 W to 900 W, with 10-second intervals. (a) The three sensors were at the same level on the chamber, with 80 mm difference from the water level. (b) Sensor 1 exhibited damages only on areas with deficient epoxy cover. Sensors 2 and 3 displayed damages on the surface layer. 63

Figure 4.6– Magnitude variation of the sub-harmonic (f/2) for Sensors 1, 2, and 3 at Position 1. The analysis is divided into three zones, Zone 1 (0 W to 500±10 W), Zone 2 (Beginning of cavitation, 500±10 W to 600±10 W), Zone 3 (Developed cavitation, after 600±10 W).. 64

Figure 4.7– Analysis of sub-harmonic magnitude variation for Sensors 1 and 3 at Position 1. Standard deviation aside, line plots show consistent behavior, especially for lower values. Cavitation threshold lies between 500 W and 600 W, marked by a sharp increase. Value at 350 W is negligible, stemming from an instantaneous peak. 65

Figure 4.8– Fast Fourier transform graphics for the sensor 1 at position 1 for (a) 260±10 W (b) 500±10 W and (c) 700±10 W. 66

Figure 4.9– Fast Fourier transform graphics for the sensor 3 at the position 1 for (a) 260±10 W (b) 500±10 W and (c) 700±10 W. 67

Figure 4.10– Magnitude variation of the sub-harmonic for Sensors 1, 2, and 3 at Position 2. The analysis is segmented into three zones: Zone 1 (0 W to 410 W), Zone 2 (Beginning of cavitation, 410±10 W to 500±10 W), Zone 3 (Developed cavitation, after 500±10 W). 68

Figure 4.11– Analysis of sub-harmonic magnitude variation for Sensors 1 and 3 at Position 2. The cavitation threshold is between 400±10 W and 500±10 W, marked by a sharp increase. Beyond this threshold, the magnitude stabilizes with a slight decrease. 69

Figure 4.12– Fast Fourier transform graphics for the Sensor 1 at the Position 2 for (a) 260±10 W (b) 500±10 W and (c) 700±10 W. 70

Figure 4.13– Fast Fourier transform graphics for the sensor 3 at the position 2 for (a) 260±10 W (b) 500±10 W and (c) 700±10 W. 71

Figure 4.14– Bubble formation due to cavitation over 4 seconds. Cavitation flow changes in axial and radial positions may interfere with acoustic readings due to waves propagating in different directions within the same position. 72

Figure 4.15– Cavitation generation by the ultrasound acoustic radiator (a) Ultrasound induces cavitation with axial and radial movements, creating centrifugal flow. Axial movements at base generate cavitation-aligned acoustic waves. (b) Acoustic streaming distribution along wave guide, low and high center amplitude. (c) Conical bubble structure on ultrasound acoustic radiator tip. . . . 74

Figure 4.16– Analysis of the distribution of the noise on the voltage acquisition and it relation with the sub-harmonic, harmonic and ultra-harmonic. 75

Figure 4.17– (a) Voltage Values Recorded by Piezoelectric Sensor 1. (b) Corresponding Impact Load Calculated Using the Previous Calibration Line and the mean voltage value.. 75

Figure 4.18– (a) Voltage Values Recorded by Piezoelectric Sensor 2. (b) Corresponding Impact Load Calculated Using the Previous Calibration Line and the mean voltage value.. 76

Figure 4.19– Piezoelectric sensors with two geometries. Piezoelectric A represents the unmodified piezoelectric, while Piezoelectric B denotes the final geometry and its corresponding Epoxy layer. . . 77

Figure 4.20– Impedance graphic for piezoelectric A with the Resonance t 44,550 Hz and anti-resonance at 45,480 Hz. 77

Figure 4.21– Impedance graph for Piezoelectric B, which includes the epoxy layer, two distinct resonances and anti-resonance are evident: (a) at 44,550 Hz and 46,500 Hz and at (b) 46,500 Hz and 47,520 Hz. 78

Figure 4.22– Ultrasound Resonance Test. (a) Conducted at different levels of submersion in water. (b) Resonance at minimal water contact measured at 19,700 Hz. Decreasing submersion depth led to a decrease in resonance frequency. 79

Figure 4.23– Flocculation and coagulation test on water-oil mixture: (a) Experiment: 500 mL beaker with 500 mL water and 10 mL SAE 10W40 oil. (b) Intermittent ultrasound treatment: 15 seconds on, 15 seconds off, for 2 minutes. 80

Figure 4.24– Mixture visual behaviour over 3 minutes. (a) Initial state pre-ultrasound. (b) Movement of water mixture in the first second after ultrasound, forming an inverted mushroom-shaped white mixture. (c)(d) By the second second, the mixture is entirely white. 81

Figure 4.25– Sequence of Water Flow Movements upon Contact with Ultrasound. (a) Initially, the wave propagates along the same axis as the ultrasound. (b) Upon reaching the bottom, the flow tends to dissipate towards the base, causing radial movement. (c) The flow now has two paths: it can ascend through the sides, escaping ultrasound, or remain at the bottom as refluxes. (d) Escaped molecules are recirculated to the bottom due to continued ultrasound action. 82

Figure 4.26– Effects of acoustic cavitation on the ORP and pH of ultra-filtered water. (a) The ORP increases 2.52 times fast with ultrasound action and then stabilize. (b) The decreases 2.29 times faster and then stabilize as well. 84

Figure 4.27– Effects of acoustic cavitation on the ORP and pH of ultra-filtered water. (a) The ultrasound action promotes an exponential decrease over the ORP values and (b) the same action promotes only a difference on pH after 70 seconds.. 85

Figure 4.28– Equipment used for the adsorption tests. (a) Ultrasound with the beaker with the solution to treat. The beaker is in a water cooling system with a tank with water. (b) Rotational machine for the mechanical action. 86

Figure 4.29– Experimental procedure for the adsorption tests. Each experiment has 500 mL of ultra-filtrated water, pollutant solution and adsorbent. In some cases, the adsorbent is not used. The time points for the samples removal it were 0, 1, 5, 15 and 30 minutes. 87

Figure 4.30– Hanna 83300 for the measurement of inorganic pollutants concentration on the samples. 88

Figure 4.31– Ciprofloxacine removal rate and it temperature during the exposition time, combining the ultrasound with (a) Kaolinite and with (b) Organic Compound. 89

Figure 4.32– Copper removal rate during the 30 minutes exposition time, combining the ultrasound with (a) Kaolinite and with (b) Organic Compound. 90

Figure 5.1– Experimental Setup for Ultrasound Cleaning in ETAR of Serzedo. The ultrasound unit is linked to both the power supply and a computer for system control. The transducer is cooled using compressed air supplied by an air compressor. 93

Figure 5.2– Experimental Study Scheme with Real Wastewater: A 500 mL sample is collected at 0, 2, 5, 10, and 20 minutes, followed by analysis using the HANNA HI98494. An 80 mL sample is extracted from the initial 500 mL for subsequent laboratory testing, while the remaining solution is returned to the chamber. 94

Figure 5.3– Variation of parameters that are indicators of chemical reactions on wastewater treatment with application of a acoustic power of 200 W. (a) pH and ORP (b) Temperature and Dissolved Oxygen. 96

Figure 5.4– COD removal with application of a acoustic power of 200 W. 97

Figure 5.5– Variation of parameters that are indicators of chemical reactions and biological and organic reaction along wastewater treatment with application of a acoustic power of 200 W. (a) $N^-NH_4^-$ and $N^-NO_3^-$ (b) N_{total} and PO_4^- 98

Figure 5.6– Variation of parameters that are indicators of chemical reactions on wastewater treatment with application of a acoustic power of 400 W. (a) pH and ORP (b) Temperature and Dissolved Oxygen. 99

Figure 5.7– COD removal with application of a acoustic power of 400 W. 99

Figure 5.8– Variation of parameters that are indicators of chemical reactions and biological and organic reaction along wastewater treatment with application of a acoustic power of 400 W. (a) $N^-NH_4^-$ and $N^-NO_3^-$ (b) N_{total} and PO_4^- 100

Figure 5.9– Variation of parameters that are indicators of chemical reactions on wastewater treatment with application of a acoustic power of 800 W. (a) pH and ORP (b) Temperature and Dissolved Oxygen. 101

Figure 5.10– COD removal with application of a acoustic power of 800 W. 101

Figure 5.11– Variation of parameters that are indicators of chemical reactions and biological and organic reaction along wastewater treatment with application of a acoustic power of 800 W. (a) $N^-NH_4^-$ and $N^-NO_3^-$ (b) N_{total} and PO_4^-. 102

Figure 5.12– COD removal comparison for the three powers of 200 W, 400 W and 800 W. 104

Figure A.1– Data-sheet of the piezoelectric device provided by the manufacturer. 124

List of Tables

Table 2.1– ORP ranges for each chemical reaction in water [31].. 7

Table 2.2– Water Quality Classification based on BOD_5 and COD [34]. 8

Table 3.1– Sensor requirements for the design and development of the acoustic sensor reading.. . . 44

Table 3.2– Data Acquisition Parameters for the NI cDAQ 9172. 58

Table 4.1– Resonance and Anti-Resonance comparison between Piezoelectric A and B. 78

Table 4.2– Insights provided by the data analysis from the chamber sensorization.. 91

Table 4.3– Insights provided by the data analysis from the application of Ultrasound on water. 91

Table 4.4– Insights provided by the data analysis from the aplication of Ultrasound with adsorption processes. 92

Table 5.1– Physical and Chemical Parameters of Wastewater Before the Ultrasound Assisted Treatment with each Different Power. 95

Table 5.2– Physical and chemical parameters for the wastewater treated with ultrasound along the experimental test. Parameters at 0, 2, 5, 10 and 20 minutes.. 95

Table B.1– Experimental data of sensor 2 and corresponding calibration results with the 0.30 g sphere.. 125

Table B.2– Experimental data from sensor 2 and corresponding calibration results with the 2.02 grams sphere.. 126

Table B.3– Experimental data from sensor 2 and corresponding calibration results with the 0.88 grams sphere.. 126

Table B.4– Experimental data from sensor 3 and corresponding calibration results with the 0.30 grams sphere.. 128

Table B.5– Experimental data from sensor 3 and corresponding calibration results with the 2.02 grams sphere.. 129

Table B.6– Experimental data from sensor 3 and corresponding calibration results with the 0.88 grams sphere.. 129

List of Symbols

Abbreviations, Initials, and Acronyms

A	Ultrasound Amplitude	μm
BOD	Biomechanical Oxygen Demand	-
BNR	Biological Nutrient Removal	-
CIP	Ciprofloxacin	-
COD	Chemical Oxygen Demand	mV
CO_2	Carbon Dioxide	-
DBPs	Disinfection by-products	-
EC	Emergent Pollutants	-
EPR	Electron Paramagnetic Resonance	-
H	Hydrogen	-
HO	Hydroxyl Radical	-
H_2O	Water	-
H_2O_2	Hydrogen Peroxide	-
MA	Mechanical Action	-
O_3	Ozone	-
OC	Organic Compound	-
OD	Oxygen Demand	mg/L
PAHs	Poly Aromatic Hydrocarbons	-
pH	Potential of Hydrogen	-
R	Resistance	Ω
TDS	Total Dissolved Solids	mg/L
TiO_2	Titanium Dioxide	-
TOC	Total Organic Carbon	mg/L
TN	Total Nitrogen	mg/L
US	Ultrasound	-
UV	Ultra-Violet	-
WWTP	Wastewater Treatment Plant	-
ZnO	Zinc Oxide	-

Roman Symbols

c	Speed of Sound	343 m/s
f	Frequency	Hz
I	Current	A
L	Length	m
L_I	Intensity of Sound	dB
M	Molar Mass	g/mol
m	Mass	kg
p	Pressure	MPa
P	Power	W
I_s	Ultrasound Intensity	W/m^3
T	Temperature	°C
t	Time	s
V	Volume	m^3
Z	Acoustic Impedance	Ω

Greek Symbols

γ	Surface Tension	N/m
λ	Wavelength	μm
ω	Angular Velocity	rad/s
σ	Electrical Conductivity	μS/cm

1. Introduction

1.1 Contextualization

Water, a vital global resource, has been facing escalating challenges in recent years. Access to clean water, recognized as a fundamental human right by the Union Nations, is indispensable for a healthy and dignified life [1]. However, increasing water scarcity poses substantial risks to communities worldwide, imperiling standards of food production, goods manufacturing, sanitation, and public health [2].

Over the past four decades, global water usage has been mounting at a rate of 1% annually, with emerging economies expected to sustain this trend until 2050 [3]. Concurrently, the availability of freshwater per capita is dwindling, with Africa and Asia experiencing the most pronounced declines at 41% and 30%, respectively, while Europe displays a more modest reduction at 3% [3]. Even in Europe, 30% of countries encountered water scarcity conditions during the Summer of 2015 [4]. Currently, 10% of the global population resides in regions facing high or critical water stress [3].

In tandem with these challenges, climate change presents a formidable obstacle for the future, precipitating various human and economic repercussions. Projections estimate a global population of 8.6 billion by 2030, potentially surging to 9.7 billion by 2050, intensifying pressure on water resources. Each additional person necessitates 1,300 m^3 of water annually [5].

Wastewater treatment stands at the forefront of critical global challenges. As industrial, domestic, and agricultural activities continue to generate wastewater laden with organic and inorganic pollutants, the need for effective treatment methods has become increasingly urgent [6]. Conventional approaches, including coagulation, biological oxidation, absorption, and ion exchange, are struggling to keep pace with the escalating release of organic compounds and the emergence of contaminants. These pollutants, derived from an array of sources such as medical and recreational drugs, personal care products, industrial chemicals, and more, have infiltrated wastewater treatment plant effluents, surface water, groundwater, and even drinking water [7–9].

Moreover, the inadequacies of current treatment methods are evident in their limited ability to ensure total disinfection of wastewater. The high toxicity and carcinogenicity of certain pollutants pose a significant challenge, necessitating the breakdown of refractory molecules into smaller, more amenable forms for further oxidation through biological methods [10]. Chlorination, a common method for disinfection due to its cost-effectiveness and ease of implementation, falls short in eliminating persistent toxic by-products. It is also ill-suited for addressing wet weather pollution and urban runoff [11].

1.2 Motivation

As wastewater treatment facilities emerge as major (indirect) emitters of organic micro pollutants into the aquatic environment, there is an evident and pressing need for the implementation of new technologies to ensure the comprehensive removal of contaminants [12, 13]. In this context, Advanced Oxidation Processes (AOPs) have gained prominence. These processes, characterized by numerous radical reactions that target recalcitrant organic compounds, offer a potential solution with their low selectivity and ability to mineralize contaminants into harmless compounds [7, 14].

In light of the pressing challenges in wastewater treatment outlined above, the exploration of innovative and effective solutions has become paramount. One such promising avenue lies in the integration of ultrasound technology. Ultrasound, known for its versatility and non-invasive nature, has demonstrated remarkable potential in enhancing wastewater treatment processes. It offers a clean and chemical-free alternative, steering clear of the production of toxic compounds often associated with traditional treatment methods [7, 15].

The potential of ultrasound in revolutionizing wastewater treatment is underscored by its capacity to efficiently remove a wide range of contaminants. From bacteria to pharmaceuticals, ultrasound's efficacy in eliminating pollutants is a testament to its versatility [16–18]. Its simplicity and lack of reliance on chemical interactions, which can lead to the formation of harmful by-products, set ultrasound apart as a sustainable and environmentally conscious solution [13, 15].

This research is further motivated by its integration into the larger "Res4Valor" project. This project delves into the adsorption behavior of organic compounds, aiming to evaluate the efficiency of various filter media in retaining pollutants. The insights gained from this endeavor will not only contribute to the development of selection criteria and system designs for environmental protection but also form the foundation for a comprehensive comparison between adsorption and ultrasonic cavitation. The potential synergy between these wastewater treatment technologies holds promise for a more sustainable and effective approach to tackling water pollution.

In the face of escalating wastewater challenges, harnessing the power of ultrasound presents an opportunity to redefine the landscape of wastewater treatment. This research endeavors to unlock the full potential of ultrasound technology, offering a beacon of hope for a cleaner, more sustainable future.

1.3 Objectives

This work focuses on two main objectives related to wastewater treatment. The first objective is to evaluate the effects of ultrasound on various components of a wastewater treatment plant, with a specific focus on the adsorption process and oxidation. The second objective is to suggest the guidelines for a correct conception of an equipment assisted by ultrasound to auxiliary the wastewater treatment.

The primary objective is to study the impact of ultrasound waves on wastewater treatment processes. This entails an examination of acoustic cavitation across various phases of wastewater treatment, including flocculation, coagulation, oxidation and adsorption. Additionally, will be investigated the effects of ultrasonic cavitation on water and oil-water mixtures. The study will extend to water samples containing both organic and non-organic matter to assess pollutant removal. Special attention will be given to the adsorption process, particularly with respect to an organic compound and Kaolinite. This investigation aims to ascertain if ultrasound can effectively enhance adsorption processes.

In addition to the research on ultrasound effects, this work seeks to set the guidelines for develop an ultrasound equipment for wastewater treatment. The equipment will undergo validation through various tests, with a particular focus on developing mechatronic devices to monitor acoustic cavitation inside the ultrasound chamber. The success of the prototype is directly linked to sensorization. The instruments used to monitor acoustic cavitation will provide crucial insights into the functioning of ultrasound and the design of the chamber.

To establish a comprehensive perspective on the potential of ultrasound in wastewater treatment, it is intended to study diverse physical and chemical water parameters over varying duration and under different ultrasound power settings. This extensive analysis seeks to integrate the data garnered from the preceding experiments, allowing for a comprehensive understanding of ultrasound's impact on wastewater. Ultimately, this aims to offer valuable insights that will guide the development of future equipment. At the same time, the study intends to understand and validate the variation of acoustic cavitation over time.

This research aims to investigate the impact of ultrasound on wastewater treatment and analyze the key factors influencing its performance. The study seeks to evaluate the technology's potential for improving wastewater treatment processes and aims to achieve a comprehensive understanding of ultrasound and its associated mechanisms.

1.4 Structure of the Dissertation

This dissertation is divided into six parts, commencing with the Introduction addressing the wastewater treatment problem, its consequences, and the potential contribution of advanced oxidation processes to enhance the removal of emergent pollutants. The main objectives of this dissertation are also outlined.

The second chapter lays the foundation for the exploration of established knowledge. It begins with an overview of wastewater treatment plants and their characteristics. Parameters ensuring water quality are presented, alongside discussions on emergent pollutants. Subsequently, a comprehensive review of literature pertaining to the utilization of ultrasound as an assisting process for wastewater treatment techniques is provided. Special attention is given to coagulation, flocculation, adsorption, and general wastewater treatment with ultrasound.

The chapter culminates in a thorough investigation of cavitation phenomena, its introduction in chemistry, and the underlying principles governing its characterization.

The subsequent chapter introduces the equipment, detailing its features and the requisites necessary for developing the sensor for acoustic characterization, along with the sensor development process.

Following the equipment development chapter, the dissertation proceeds to the experimental evaluation of the sensors, as well as the effect of ultrasound on water. This chapter encompasses the calibration of sensors and their integration into the chamber to comprehend cavitation phenomena. Concurrently, it presents the results of cavitation on water, both with and without oil mixture. Additionally, the augmentation of adsorption processes is assessed. The chapter concludes with insights gleaned from the experimental tests.

Post the experimental evaluation, a real case study is presented involving the performance assessment of a wastewater treatment plant. Here, the impact of ultrasound cavitation on various water quality parameters is evaluated.

In the conclusions, the discussion is partitioned to address sensorization, the impact of water on water with contaminants, and culminates with prospective directions for future research.

The dissertation concludes with an appendix containing piezoelectric characteristics and calibration data, followed by the list of references for this work.

2. State of Art

This chapter serves as a comprehensive bibliographic overview of wastewater and its treatment processes. It encompasses the definition and key quality parameters for wastewater assessment, as well as the conventional treatment methods. Additionally, it delves into the integration of ultrasound to enhance these processes. Furthermore, the chapter provides a thorough exploration of ultrasonic cavitation phenomena and the underlying principles governing its characterization.

2.1 Wastewater Treatment by Conventional Processes

Decree-Law No. 152/97 outlines water quality standards, notably for surface water, distinguishing between domestic and industrial wastewater [19]. Decree-Law No. 236/98 further refines these categories, introducing urban wastewater [20].

Domestic wastewater arises from residential and service buildings, primarily from human metabolism and household activities. Industrial wastewater encompasses non-domestic activities, including manufacturing and commercial processes. Urban wastewater encompasses a blend of domestic, industrial, and rainwater sources in urban areas [20].

2.1.1 Characterization of Domestic and Industrial Wastewater

A wastewater treatment plant should possess the capacity to receive wastewater from diverse sources, highlighting the importance of employing standardized quality parameters to comprehensively assess the composition of the wastewater at both the inlet and throughout the treatment process.

Substances found in water can have diverse origins. Wastewater constitutes a complex mix of dissolved or suspended substances, alongside a variety of microorganisms. These substances can be classified into four types based on their particle size: those above 10^{-3} μm are dissolved or in molecular dispersion, from 10^{-3} to 1 μm are in dispersion or colloidally suspended, up to 10 μm in fine suspension, and up to 100 μm in coarse suspension [21, 22].

Qualitative characterization of wastewater is divided into three main groups: physical, chemical, and microbiological. This characterization is essential to ensure that the treatment process is adequate and systematic [21].

The quality and quantity of pollutants in wastewater vary greatly depending on the characteristics of different countries and populations. Worldwide, these parameters change due to social, economic, and cultural differences. A study by Tchobanoglous et *al.* [23] investigated various pollutants in different

countries, revealing that wastewater treatment plants need to be adjusted and flexible enough to adapt to the diverse types of wastewater found in each country and region. To assess water quality, it is necessary to consider various parameters. Among the important physical properties that will be considered in this study, are solid concentration, turbidity, colour, and temperature [21].

Total solids in wastewater encompass both organic and inorganic substances. The organic portion is referred to as total volatile solids (TVS), while the other suspended solids are retained by wastewater filtration. **Turbidity** measures the inverse of the transparency characteristic, indicating the penetration of light into water. **True colour** is defined as the colour observed after the filtration of suspended particles. The colour can be influenced by both inorganic and organic substances. **Temperature** is another critical parameter, as it affects density, viscosity, solubility, and can accelerate biochemical processes [21, 24, 25].

Regarding chemical characteristics, there are countless sources of pollutants, resulting in millions of different chemical substances in wastewater. Characterizing water quality by identifying the specific present chemicals is virtually impossible. Instead, the chemical characterization of the pollutant is based on grouping the compounds according to their similar chemical properties, such as organic matter, total nitrogen and pesticides [21].

One of the primary parameters to evaluate is the **pH** value, which assesses the concentration of H^+ ions in the water. The pH is a measure of the potential of hydrogen ions (Hydronium) in the aqueous solution. Jensen et *al.* [26] defined pH as the negative logarithm of the hydrogen ion concentration, or in other words, the concentration of Hydronium ions, Equation 2.1.

$$pH = -\log[H_3O^+] \tag{2.1}$$

The pH measurement provides information about the balance between acidic and basic chemicals present in the analysed sample. It describes the concentrations of hydronium (H_3O^+) and hydroxide (OH^-) ions in the aqueous solution. The pH scale ranges from 0 to 14 and is logarithmic, meaning that each unit change represents a tenfold difference in acidity or alkalinity. The neutral point is at pH 7, below which the solution is considered acidic, and above which it is considered alkaline. Acidic reactions have more free hydronium ions (positively charged), while alkaline reactions have more negatively charged hydroxide ions. pH measures the activity of hydrogen ions in the solution [27]. By measuring pH, it is possible to identify the ongoing chemical reactions in the water [28].

ORP (Oxidation-Reduction Potential) measures how one substance can oxidize or reduce another substance. Essentially, it indicates the electric potential of a liquid at a specific temperature. ORP is measured using a chemical-inert platinum electrode immersed in the solution sample. The electrical

potential is then read relative to the reference electrode, and the value is presented in millivolts (mV) or Volts (V) [29].

The measurement values provided by ORP indicate whether a substance tends to undergo oxidation or reduction when in contact with another substance. In other words, ORP measures if a substance is more likely to lose or gain electrons during a chemical reaction. Oxidation refers to the loss of electrons, while reduction involves the gain of electrons. The ORP meter's measurement is a result of the relationship between oxidizing agents and reducing agents in the solution [30].

Biochemical reactions can be diagnosed by comparing the ORP value with the corresponding values in Table 2.1. ORP indicates the ability of wastewater to allow the occurrence of specific biological reactions. The lifespan of bacteria in water can be easily detected by ORP, making it a valuable tool in controlling water treatment processes and identifying prevalent reactions [31].

ORP is a crucial parameter in drinking water supply systems, helping maintain high oxidation levels through sanitization to prevent contamination. It's instrumental in evaluating water quality and the efficacy of sanitizing agents. Monitoring ORP enables the detection of potential issues that could affect water quality [28].

Table 2.1: ORP ranges for each chemical reaction in water [31].

Biochemical Reaction	**ORP range (mV)**
Nitrification	+100 to +350
cBOD degradation	+50 to +250
Biological phosphorus removal	+25 to +250
Denitrification	+50 to -50
Sulfide formation	-50 to -250
Biological phosphorus release	-100 to -250
Acid formation	-100 to -225
Methane production	-175 to -400

Organic matter in water can be classified into two main types: biodegradable and non-biodegradable. Biodegradable compounds are predominantly composed of proteins, carbohydrates, and lipids. Their degradation is facilitated by redox reactions, contingent on the final electron acceptor. This process can be further categorized as aerobic (in the presence of oxygen as the acceptor), anoxic (utilizing nitrate or nitrite as the acceptor), and anaerobic (with organic compounds serving as the acceptor) [21].

To assess the organic matter present in water, three commonly used parameters are **Biochemical Oxygen Demand** (BOD), **Chemical Oxygen Demand** (COD), and **Total Organic Carbon** (TOC). Together, these parameters provide a comprehensive evaluation of the oxidizable organic matter.

BOD (Biochemical Oxygen Demand) is a critical parameter that quantifies the amount of oxygen utilized during the biochemical oxidation of organic matter in water over a specified time period and at a particular temperature, typically for 5 days at 20 °C. This parameter indirectly assesses the biodegradable organic matter in water, including carbohydrates, proteins, and fats. The measurement is based on the consumption of dissolved oxygen, which is proportional to the amount of organic matter that undergoes biochemical oxidation [21, 22].

Chemical Oxygen Demand (COD), on the other hand, evaluates the amount of organic matter in water. It is determined by measuring the amount of oxygen required for the chemical oxidation of organic matter using potassium dichromate under standardized conditions [32].

Total Organic Carbon (TOC) measures the overall concentration of organic matter in water. It is used to determine the amount of carbon-containing compounds present in a sample [33]. These parameters, in combination, provide valuable information about the presence and extent of organic pollutants in wastewater, helping in wastewater treatment and environmental management.

In Table 2.2, it is possible to observe the information that COD and BOD provide regarding water quality, along with the acceptable ranges for each parameter [34].

Table 2.2: Water Quality Classification based on BOD_5 and COD [34].

Indicator Value Range (mg/L)	**Water Quality Classification**
BOD5 < 3	Excellent
3 < BOD5 < 6	Good
6 < BOD5 < 30	Acceptable
30 < BOD5 < 120	Contaminated
BOD5 > 120	Heavily Contaminated
COD < 10	Excellent
10 < COD < 20	Good
20 < COD < 40	Acceptable
40 < COD < 200	Contaminated
COD > 200	Heavily Contaminated

2.1.2 Emergent Pollutants

Emerging pollutants refer to new compounds or chemicals that lack regulatory status, and whose effects on the environment and human health remain unknown. Consequently, establishing a definitive maximum allowable concentration in sanitized water becomes a challenging task. Currently, the impacts of substances like phthalates, pharmaceutical compounds, PAHs, PCBs, and Bisphenol A remain uncertain, highlighting a significant gap in our understanding [35]. This category encompasses a broad spectrum of contaminants, ranging from pharmaceuticals and personal care products to plastic waste, pesticides, and metals. Detecting and characterizing these pollutants presents difficulties due to their varied sources, diverse forms, and complex behaviour [36, 37].

These emerging pollutants stem from a range of sources, including hospital wastewater discharge, illicit drug use, municipal sewage, discharges from wastewater treatment plants (WWTPs), landfill leachate, among others [38]. Their presence is particularly concerning considering their potential to contaminate soil, rivers, surface water, and even groundwater. Consequently, they may be transferred from soil to plants and ultimately reach consumers, leading to the presence of pollutants in crops and potentially impacting human consumption [39].

Ciprofloxacin (CIP) belong to te group of emergent pollutants, in this case from the pharmaceuticals. It belongs to the fluoroquinolone group of broad-spectrum antibiotics and finds extensive use globally in treating various bacterial infections, including those affecting the urinary, respiratory, gastrointestinal, skin, bone, and joints. With a chemical formula of $C_{17}H_{18}FN_3O_3$ and a molecular weight of approximately 331.34 g/mol [40], it is a pivotal drug in modern medicine.

Despite its therapeutic benefits, the environmental impact of CIP is a growing concern due to its low biodegradability, leading to its accumulation in ecosystems. This accumulation poses risks such as interference with non-target pathogens, plant photosynthesis, structural alterations in algae, and the emergence of antibiotic-resistant bacteria. Notably, CIP has been consistently detected in effluents from wastewater treatment plants, surface waters, and groundwater, with recorded concentrations reaching as high as 30 mg/L and 50 mg/L in pharmaceutical wastewater [40].

Copper, a prevalent heavy metal in wastewater, continues to be a major concern for wastewater treatment plants [41]. Its presence in wastewater is pervasive due to its extensive utilization across various industrial applications, establishing it as one of the most commonly employed metals in these processes. The prevalence of copper in wastewater arises from its inclusion in a wide array of industrial processes, ranging from electronics manufacturing to construction, plumbing, and even in agricultural practices as a key component in pesticides and fertilizers.

Notably, Copper is classified as a heavy metal due to its remarkably high density, exceeding that of water by fivefold. This characteristic, while contributing to its utility in industry, also underscores its potential environmental and health risks. Even at relatively low concentrations, copper poses a substantial toxic threat to both aquatic ecosystems and human health [42].

According to established guidelines from the World Health Organization and Portugal's regulatory framework, the allowable copper ion content in drinking water should not surpass 2 mg/L, underscoring the significance of controlling copper levels to safeguard human health [43]. This guideline is rooted in extensive research highlighting the potential harm posed by elevated copper concentrations.

The toxicity of heavy metals, including copper, is further compounded by their enduring presence and propensity to accumulate within living organisms. This phenomenon is not confined to a particular species but spans a broad spectrum of organisms, from microorganisms in the soil to aquatic plants and animals. The accumulation of copper can lead to a cascade of severe health issues, ranging from carcinogenic effects to disruptions in the nervous system and even renal failure, with potentially fatal consequences when present in elevated amounts [41].

2.1.3 Wastewater Treatment Plant

A wastewater treatment plant enclose unitary treatment processes and operations designed to eliminate pollutants and microorganisms, resulting in treated wastewater that meets specific quality standards [44].

There are three primary categories of wastewater treatment based on the process employed: Physical, Chemical and Biological. These are employed sequentially to eliminate toxic compounds from the aqueous solution. Figure 2.1 illustrates the key unitary processes utilized in each method. In a wastewater treatment plant, a selection of these processes is employed, either individually or in combination, to ensure the final effluent meets required standards [21].

Wastewater pollutants can exist in both dissolved and suspended forms. In an ordinary wastewater treatment plant, there are five levels of treatment: preliminary, primary, secondary, tertiary, and advanced treatment. Each level of treatment serves a purpose of removing pollutants and improving the quality of the effluent [21].

In Portugal, the regulation of wastewater treatment plants is governed by Directive No. 91/271/CEE and Decree-Law No. 152/97 [19]. These directives provide guidelines for the types of pollutants and the appropriate treatment levels required for wastewater treatment in the country. By following these regulations, wastewater treatment plants in Portugal can effectively treat wastewater and ensure that the discharged effluent meets the necessary environmental standards [19].

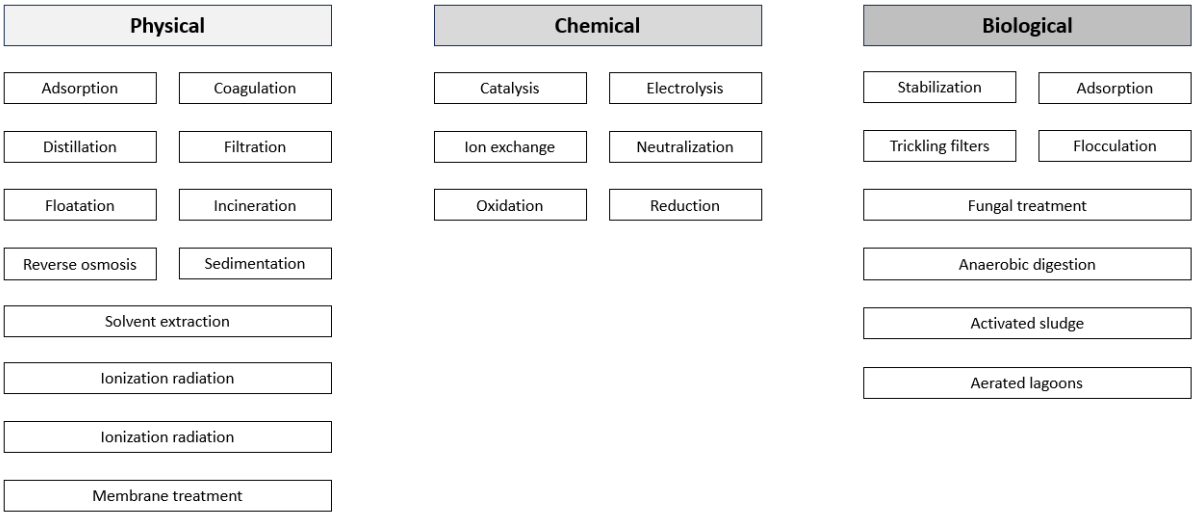

Figure 2.1: Three main groups of possibles wastewater treatment, physical, chemical or biological. During the conventional process, these can be combined between them.

The treatment comprises three phases: liquid, solid, and gas. The liquid phase encompasses preliminary, secondary, tertiary, and advanced treatments. The primary objective of preliminary treatment is the removal of solids, sand, and grease to optimize the effectiveness of subsequent treatments, preventing blockages and contamination. This phase achieves the elimination of suspended solids through sedimentation, decantation, or chemical coagulation [45].

After the secondary treatment, the effluent is expected to meet the quality requirements, with low biodegradable organic matter and colloidal suspension. Biological processes take on significant importance in this phase but are not the only ones. Following the biological reactor, there is a decanter assisted by coagulation-flocculation to separate the biological and chemical flakes [21].

When needed, the tertiary and advanced treatments further improve the quality of water provided by the last two. In the tertiary treatment, the main goal is to remove nutrients such as nitrogen and phosphorus. On the other hand, the advanced process refines the water quality even further by eliminating pollutants in residual concentrations [21].

Solid pollutants are removed in the preliminary treatment in grated, sieved, sand, and grease forms. In the gas phase treatment, the primary focus is to diminish the odour from methane emissions. However, for this study, only the liquid phase is of interest and will be addressed [46].

In Figure 2.2, it is possible to observe a schematic representation of a typical WWTP, focusing on the liquid phase treatment. Each unitary treatment leads to the separation of pollutants, resulting in a progressive cleaning of water and, during the processes, the release of some types of sludge.

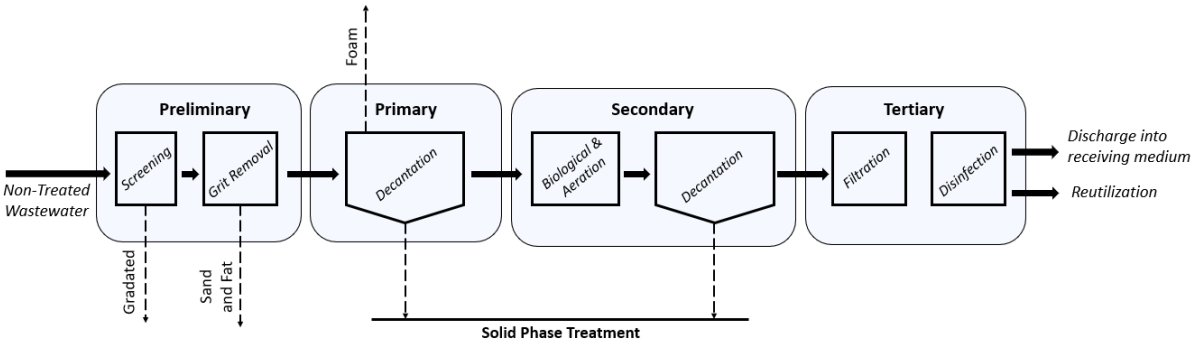

Figure 2.2: Diagram of a WWTP and the primary procedures carried out during each phase of liquid treatment. Image adapted from Shah et *al.* [45].

Preliminary treatment encompasses several mechanisms. The initial step is harrowing, responsible for segregating larger solid waste. The subsequent phase, known as screening, refines the process further with a more delicate retention mesh [22].

Once the major residues have been removed, the subsequent phases focus on extracting smaller pollutants such as sand, oil, and grease. Desandation, grease and oil removal can be achieved using the same equipment but serve distinct purposes. Desandation aims to extract sand from the effluent by combining reduced fluid velocity with gravity-induced sand deposition. Conversely, techniques are employed for oil and grease removal, primarily to accumulate grease on the surface [22].

Following the initial treatment of the wastewater effluent, the first treatment is implemented. Typically, this treatment involves three key unitary processes: sedimentation, decantation, and flotation. These processes lead to a reduction of TSS by approximately 50% to 70% and BOD by around 30% to 40% [47].

In the secondary treatment stage of wastewater treatment, the focus shifts towards the implementation of biological methods for a more thorough purification process, targeting the removal of a substantial amount of organic pollutants. This phase employs various processes, including activated sludge, trickling filters, and rotating biological contactors, all designed to significantly reduce both BOD and SST. Integral to this phase are microorganisms like bacteria and protozoa, crucial in breaking down remaining organic matter. The secondary treatment concludes with a secondary decantation. However, trace quantities of pollutants and biological matter persist in the treated water, necessitating tertiary and refinement treatments. These employ more sophisticated processes, paving the way for potential water reuse [22].

Tertiary treatment complements the preceding treatment stages by eliminating pollutants that persist in the water, including pathogens, nutrients like nitrogen and phosphorus, and particles that are

challenging to remove. Nitrogen and phosphorus can be removed through biological or chemical means, while disinfection aims to partially destroy or inactivate pathogens using chemical agents like ozone and chlorine, and UV radiation. Filtration is typically performed prior to UV disinfection to remove suspended particles. Additional treatments encompass coagulation, flocculation, sedimentation, activated carbon adsorption, ion exchange, and reverse osmosis, all designed to remove specific pollutants through physical and/or chemical processes [22].

Numerous techniques have been employed to extract pollutants from water, but many merely relocate the pollution to another phase, necessitating further processing of solid waste and regenerating adsorbents. To address this issue, alternative methods like biodegradation, ozonation, and advanced oxidation processes have been adopted. Among these, photocatalytic degradation and AOPs have emerged as promising techniques for completely mineralizing organic contaminants present in wastewater and effluent streams [48].

To contextualize this thesis proposal and provide a comprehensive analysis, it is essential to expand the examination of chemical coagulation, adsorption, and AOPs.

A crucial mechanism in water treatment is **flotation**. Its primary objective mirrors that of decantation, involving the separation of solid or liquid particles suspended in water. These particles rise to the surface, forming a buoyant layer. This process is commonly employed for grease treatment and is applied in preliminary, secondary, and solid-phase treatment stages [21].

Particles with a lower density than water tend to rise towards the liquid's surface. The viscosity of the liquid directly impacts the movement of these particles, making it a more challenging process. There are methods to improve efficiency, such as introducing compressed air, which adheres to suspended particles during their ascent [49].

Separating colloidal suspended particles in water poses a significant challenge. Chemical coagulation is the key process that destabilizes these particles, enabling subsequent flocculation. This step is integral to wastewater treatment, enhancing the removal of solid sediments in both primary and secondary processes and preparing for subsequent processes like filtration [50].

Flocculation follows coagulation, aggregating the micro-clots formed earlier. The underlying principles of this process, along with unitary processes, are depicted in Figure 2.3. After flocculation, it becomes necessary to separate the suspended solids from the water using various methods such as sedimentation, flotation, filtration, and more [21].

In Figure 2.3, a visual representation of the processes over time is provided. These are crucial for the effective treatment of water contaminants.

The initial step in this sequence involves the destabilization of colloidal particles through chemical coagulation. This process hinges on the electrical charge, typically negative, that surrounds these particles. The negative charge results in repulsion between particles, keeping them suspended in the water. The stability of particle suspension in water is primarily dictated by the electrical charge of colloidal particles and the double layer of ions enveloping them [21, 49].

To destabilize colloidal particles, it is imperative to neutralize the negative charges on their surfaces. Upon introducing coagulant agents into the water, these disrupt the particles' electrical charges, causing them to draw nearer and form micro-flocs. Among the most frequently employed coagulants are ferric chloride or alum, known for their positive electrical charge, which aids in effectively neutralizing the negatively charged colloidal particles [51].

Once the colloidal particles are destabilized and broken apart through coagulation, the subsequent step involves bringing them together to form larger aggregates or flakes. This crucial process is known as flocculation. It typically entails gentle stirring or agitation to promote collisions between the destabilized particles. This interaction allows the particles to adhere to one another, forming larger, easily removable aggregates. These larger particles can be efficiently eliminated through processes such as sedimentation or filtration [21].

The interplay between coagulation and flocculation is illustrated in Figure 2.3, providing a visual representation of these essential water treatment stages [52].

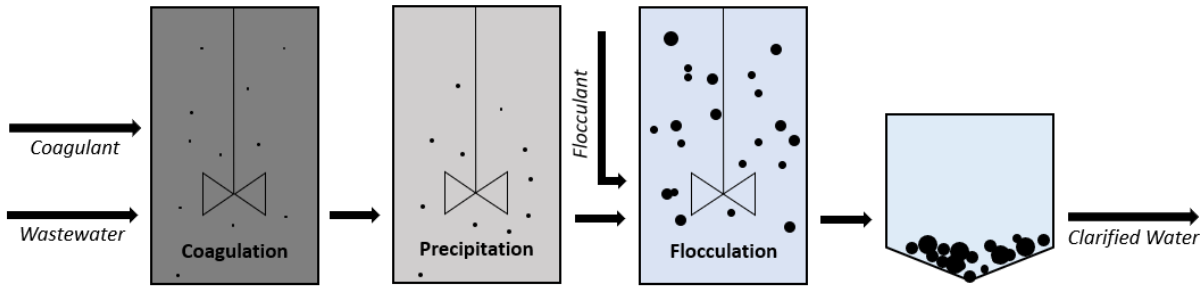

Figure 2.3: Sequence of coagulation and flocculation as part of wastewater treatment. Image adapted from Teh et *al.* [52] .

In the realm of tertiary wastewater treatment, a myriad of processes come into play to ensure the effective elimination of heavy metals, oil emulsions, as well as inorganic and organic compounds. Among the commonly employed methods are gravitational separation, centrifugation, coagulation, flotation, adsorption, biological treatments, filtration techniques, and thermal oxidation [53].

In recent years, there has been a growing focus on the development of novel adsorption processes

aimed at enhancing the removal of both organic and inorganic pollutants from water. **Adsorption** stands out as one of the most efficient, effective, and economically viable methods for water purification. This technology boasts a wide array of adsorbent categories and finds applicability across various research domains. Its appeal lies in its ability to provide cost-effective and highly efficient water treatment, characterized by rapid kinetics, straightforward operation, and the absence of residual by-products or sub-products. Adsorption plays a pivotal role in tasks such as separation, purification, detoxification, and the metabolism of medicinal drugs [54, 55].

The essence of adsorption processes can be summarized as mass transfer phenomena, where atoms, ions, or molecules migrate from a liquid phase onto a solid surface. This movement occurs due to interactions, whether chemical or physical in nature [56]. This approach offers significant advantages, including highly effective and rapid adsorption kinetics, compatibility with a wide range of target contaminants, and the potential for developing a diverse array of commercial products. However, it's worth noting that adsorption methods are generally non-selective, and some adsorbents can be relatively costly, with regeneration presenting certain challenges [57].

The process of adsorption involves the adherence of molecules or particles to the surface of a solid material, resulting in the formation of a thin layer, as illustrated in Figure 2.4 [58].

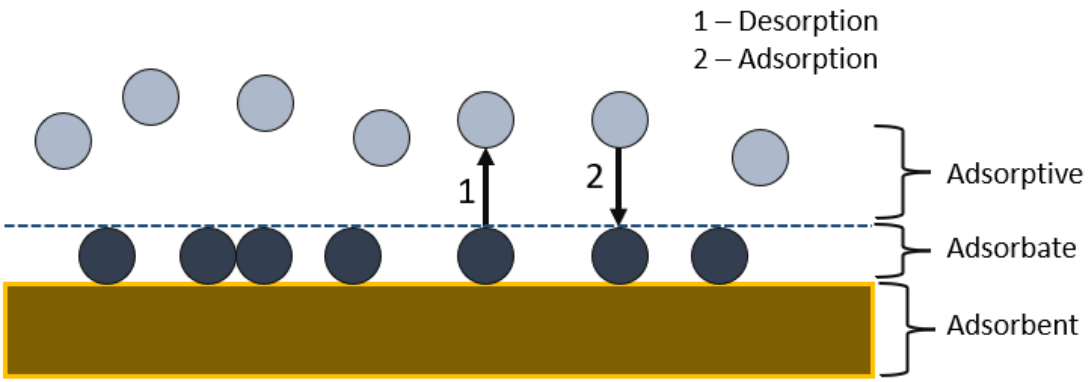

Figure 2.4: Mechanism of adsorption between a liquid and the absorbent. The process is characterize by three main layers: absorbent, adsorbate and absorptive. Image adapted from Ameri et *al.* [58].

At its core, adsorption involves the transfer of material from a fluid phase to a solid phase, making it a fundamental separation process for concentrating materials from a bulk vapour or liquid phase onto the surface of a porous solid [59].

There are two primary types of adsorption: physical adsorption and chemisorption, also known as activated adsorption. Physical adsorption is governed by van der Waals forces and occurs when an

absorbent with a solid surface interacts with an adsorbate, typically a pollutant. These forces are relatively weak and arise from temporary fluctuations in electron distribution within molecules. Generally, this process is reversible but less specific in its interactions. On the other hand, chemical adsorption involves ionic or covalent bonding between the adsorbate and the pollutant, resulting in more stable connections but requiring a higher activation energy [60].

Innovations in adsorption technology have led to the development of various efficient adsorbents. Clay-polymer composites, which combine natural clay minerals with polymeric materials, have demonstrated enhanced capabilities in removing metal ions from aqueous solutions. Additionally, industrial by-products like fly ash, iron slags, hydrous titanium oxide, and waste iron can be chemically modified to improve their heavy metal ion removal efficiency through adsorption. Furthermore, low-cost bio-sorbents, such as non-active biomass and non-living algae, have proven effective in removing heavy metal ions, including copper, from industrial wastewater [60].

The continuous advancement and diversification of adsorption technologies offer promising avenues for the efficient and environmentally responsible removal of pollutants from wastewater, contributing to the overall improvement of water quality and the protection of natural ecosystems.

In the same way, and to respond to the sludge generation and the inability to treat effluents containing high levels of recalcitrant compounds, other processes were developed.

Advanced Oxidation Processes (AOPs) are a class of treatments defined by their generation and utilization of powerful transient species, predominantly hydroxyl radicals [61, 62].

Within wastewater effluents, the compounds present have the potential to undergo oxidation, resulting in the formation of alternative species. Alternatively, a more favourable pathway involves complete mineralization, wherein the compounds are converted into carbon dioxide and water. This mineralization process is advantageous as it produces no secondary by-products or sludge [63].

As previously discussed, wastewater treatment plants (WWTPs) require upgrades to ensure the efficient removal and destruction of emerging contaminants like toxins, pesticides, dyes, and pharmaceuticals. Advanced oxidation processes (AOPs) encompass a range of powerful oxidative water treatment techniques applied in diverse settings, including industrial plants, hospitals, and wastewater treatment facilities. This category includes several methods, such as UV/O_3, UV/H_2O_2, Fenton and photo-Fenton reactions, non-thermal plasma treatments, sonolysis, photocatalysis, radiolysis, supercritical water oxidation, and others [48, 53]. These processes involve the reaction of hydroxyl radicals or other reactive oxygen species with pollutant species.

Organic pollutants commonly engage with hydroxyl radicals through either addition or hydrogen

abstraction pathways. This interaction leads to the creation of carbon-centred radicals, which subsequently react with molecular oxygen to produce peroxyl radicals. Additionally, hydroxyl radicals have the capacity to form radical cations by extracting an electron from electron-rich substrates. These cations can undergo hydrolysis in aqueous environments, resulting in the production of oxidized products. These oxidation by-products are generally less harmful and more readily amenable to bioremediation [48, 61].

However, AOPs are known for their high cost and are often used as a pretreatment step. The radicals mentioned earlier are highly effective oxidants but have a short lifespan and lower concentrations. AOPs can also serve as a quaternary treatment in WWTPs to eliminate micro-pollutants and enhance the disinfection process [48].

The hydroxyl radicals generated, exhibit characteristics such as being short-lived, easily produced, powerful oxidants, electrophilic behaviour, ubiquitous in nature, highly reactive, and practically non-selective. They have the ability to react with various organic compounds, leading to simpler and less complex organic compounds initially. In the case of complete mineralization, hydroxyl radicals result in the production of carbon dioxide, water, and inorganic salts, as demonstrated in Equation 2.2 [53, 61].

$$\text{Organic Species} + HO^{\cdot} \Rightarrow CO_2 + H_2O + \text{Inorganic ions} \tag{2.2}$$

AOPs offer several advantages over conventional methods, primarily the ability to convert complex organic compounds into simpler ones or even into CO_2 and H_2O without generating sludge. This eliminates the need for additional treatment stages. AOPs are also effective in treating wastewater with very low organic loads, containing dissolved organic compounds that are challenging to remove. However, their drawback lies in their high cost, particularly with reagents like ozone, and the energy requirements for ultraviolet technology. Consequently, AOPs are primarily considered for the alternative treatment of wastewater that cannot undergo biological treatment. They may be used as a preliminary treatment to convert recalcitrant pollutants into a form amenable to biological treatment or as a final treatment step before discharge [53].

2.2 Wastewater Treatment by Ultrasound Assisted Systems

Researchers conducted studies on the ultrasound's impact on various aspects of the wastewater treatment process. The obtained results demonstrate the potential of ultrasound in enhancing oxidation and organic degradation. As previously mentioned, the individual processes within a wastewater

treatment plant (WWTP) do not guarantee complete pollutant removal and have proven ineffective in eliminating certain contaminants like microorganisms, fine clay and Emergent Pollutants [7].

To assess the efficacy of ultrasound, whether used independently or in combination with other processes of treatment, the effects of ultrasound on pollutant removal at different points within the WWTP were investigated. The areas of focus included flocculation, sedimentation, coagulation, the removal of organic compounds and heavy metals, as well as the overall improvement of wastewater treatment facilitated by ultrasound.

2.2.1 Coagulation and Flocculation Enhanced by Ultrasound Treatment

In-depth investigations into wastewater treatment methods have highlighted the potential for significant improvements through the application of ultrasound treatment. In a study focused on sedimentation, Vikulina et *al.* [64] explored the enhancement of suspended solids settling by combining ultrasound (0.3 - 0.5 W/cm^2) with a coagulant. Experimental data demonstrated that the integration of ultrasound resulted in a decreased requirement for coagulant injection, thereby reducing the overall need for chemical additions.

This significant enhancement was reaffirmed by Ma et *al.* [65], where ultrasonic-flocculation sedimentation outperformed sole flocculation sedimentation in terms of removing total phosphorus, total nitrogen, reducing COD, BOD, and turbidity. Removal rates for TP, TN, BOD, COD Cr, and turbidity saw respective increases of 16.1%, 12.7%, 9.1%, 20.0%, and 18.3% with ultrasound power of 60 W, during two minutes and 10 g/L of flocculant.

Ultrasound treatment has demonstrated the capability to significantly enhance coagulation processes. Özyonar et *al.* [66] highlighted the effectiveness of coupling ultrasound (180 W and 40 kHz) with electrocoagulation in wastewater treatment applications. The combination with ultrasound treatment significantly enhanced the removal efficiency to 99.9% reduction in Chemical Oxygen Demand (COD). Additionally, it demonstrated remarkable colour removal rates for Reactive Red 241 and Disperse Blue 60, surpassing the rates achieved by electrocoagulation alone (87% and 92% respectively). Remarkably, these outcomes were achieved in less than a minute.

Additionally, Trujillo-Ortega et *al.* [67] investigated a method that effectively removed up to 90% of indigo dye and arsenic through the combined use of ultrasound treatment (300 W and 40 kHz) and electrocoagulation [68].

Moreover, ultrasound treatment applied with coagulation, has shown significant improvements. Fast et *al.* [69] examined turbidity removal efficiencies and found them comparable to conventional rapid mix

coagulation. Removal percentages ranged from 84.1% to 90.5% for Chitosan in the rapid mix process, and 84% to 97% for Chitosan in the ultrasound process (25 kHz and 100 W during 20 min).

Furthermore, researchers have explored the synergistic effects of ultrasound treatment when combined with other Advanced Oxidation Processes. In pretreatment, Duckhouse et *al.* [70] demonstrated enhanced E. Coli inactivation through the combination of sodium hypochlorite and ultrasound treatment at 20 kHz and 850 kHz. Another study revealed that ultrasound disinfection at 20 kHz and 500 W, when combined with chlorine dioxide, led to a 50% improvement in inactivation [71].

Ultrasound treatment has proven to be a versatile and effective tool with biocidal properties. Phull et *al.* [72] illustrated that 80% of chlorine removal is achievable with 15 minutes of sonication (20 kHz and 30 $W \cdot cm^2$). Additionally, ultrasound treatment on its own exhibited the power to reduce bacterial colonies in water. The study also emphasized that integrating ultrasound treatment into the disinfection process could lead to a reduction in the amount of required chlorine. The synergistic effect of combining sonication with normal chlorination was observed to result in a significant amplification of their individual effects, indicating that the combination is superior to sonication alone.

Stępniak *et al.* [73] examined the efficacy of ultrasonic coagulation assistance in the context of water treatment. The findings revealed that, under the conditions of a vibration amplitude of 16 μm and a frequency of 22 kHz over a period of 5 minutes, the removal of contaminants from water reached 29%. Furthermore, when combined with aluminum sulfate as a coagulant, the coagulation efficiency experienced a notable enhancement, exhibiting a 35% increase.

2.2.2 Adsorption Enhanced by Ultrasound Treatment

Researchers have delved into the augmentation of adsorption processes through ultrasound in wastewater treatment, showcasing a significant enhancement in efficiency. One crucial area of focus has been the study of emergent pollutants, with a particular emphasis on organic dyes. These dyes pose a significant concern due to their widespread industrial use and the escalating contamination caused by them in recent years.

In a similar study by Jun et *al.* [74], the role of ultrasound treatment in improving adsorbent dispersion in water was examined. Lower ultrasound frequencies, 28 kHz compared with 580 kHz, demonstrated superior performance in enhancing absorbent dispersion. Furthermore, the combination of ultrasound treatment with the adsorbent yielded remarkable results. In just 5 minutes, this approach achieved 60% removal of dye, more than double that achieved with conventional stirring assistance.

Dil et *al.* highlighted the influence of pH on the adsorption enhanced by ultrasound treatment,

demonstrating that higher values increased removal efficiency of heavy metals (Cadium and Cobalt) and azo dyes (Methylene Blue (MB)) [75]. Lower pH levels resulted in positive charges on both dyes and the adsorbent, leading to repulsion and reduced removal percentages. As pH levels increased from 2.0 to 5.0, removal efficiency improved. Above pH 5.0, dyes adhered more effectively, resulting in higher removal percentages. At pH 6.0 was identified as the optimal condition for maximum removal in the quaternary system.

The incorporation of copper-doped zinc sulfide nanoparticles loaded on activated carbon, assisted by ultrasound, enhanced the removal of Auramine-O (AO), Erythrosine (Er), and Methylene Blue (MB). Remarkably, this achieved total removal of the three dyes in just 2.5 minutes of application with a mere 0.04 g of absorbent and ultrasound parameters of 40 kHz and 130 W [76].

Numerous other studies have confirmed the effectiveness of acoustic cavitation in enhancing the removal of various dyes [77], including AB92 and DR80, AM and BB FCF, Crystal Violet, MB and EY, BR46, BB41, and MG, showcasing the broad applicability of this technique [55, 77–80].

Researchers have amassed compelling evidence supporting the use of ultrasound to enhance the removal and oxidation of ciprofloxacin from contaminated water samples. Advanced oxidation processes have proven effective in eliminating such pollutants, and when combined with ultrasound, their efficiency is significantly augmented. Furthermore, ultrasound treatment on its own demonstrates the ability to mineralize and eliminate ciprofloxacin from water.

In a study conducted by Olusholaet *al.* [81], the introduction of zinc oxide nanoparticles alongside ultrasonic treatment bolstered the degradation of the pollutant. Results showed that ultrasound treatment alone (20 kHz and 125 W) achieved a 30% degradation of CIP within just 20 minutes, with this efficiency increasing to 50% when zinc oxide nanoparticles were introduced, at the same time. After one hour, the ultrasound treatment alone, at low pH values, 1.75, reach a maximum removal of 76% and combined with absorbent it reached 96%. It was observed that lower initial concentrations of CIP favored degradation, same as low pH values.

Moreover, the utilization of a pulsing mode was found to be advantageous for degrading pharmaceuticals with high diffusivity or hydrophobicity. This mode allowed compounds to diffuse and accumulate at liquid-bubble interfaces during silent cycles, thereby facilitating the degradation process [82].

In a study by Sutar et *al.* [83], ultrasound treatment alone achieved only a 5% degradation of CIP. However, when combined with Laccase catalysis, the removal efficiency improved to 51%. The study also revealed that the duty cycle of ultrasound significantly influenced the removal rate, with a 50% duty cycle

proving more efficient than 40% and 60%. The same study mention that with the same power, 75 W, the ultrasound treatment with 22 kHz shows a better removal rate (50%) than 40 kHz (23%).

In the study by Kyzas et *al.* [84], complete removal of Ciprofloxacin was achieved by combining ultrasound treatment (20 kHz and 120 W/cm^2) with ferrous ions, hydrogen peroxide, and persulfate activation within 60 minutes. However, it was noted that high pH levels reduced the removal rate due to the destabilizing effect of ferrous ions on the structure, which in turn lowered the oxidation potential and hindered the reaction between ferrous ions and hydrogen peroxide, leading to increased sludge production.

Furthermore, Chakma et *al.* [85] examined ultrasound treatment effect on CIP, reaching a maximum removal rate of 38% (ultrasound treatment parameters: 37 kHz and 130 W) at the end of 30 minutes, with low pH values found to enhance CIP removal. This study also explore the mechanisms behind the CIP degradation, concluding that the ultrasound treatment is responsible for physical and chemical degradation.

In a study by Bel et *al.* [86], ultrasound treatment at a frequency of 520 kHz and a power density of 92 W/L resulted in a maximum removal rate of 25% after 30 minutes, with lower pH values identified as contributing to enhanced removal of CIP (initial concentration: 15 mg/L).

In another investigation, Igwegbe et *al.* [87] focused on a CIP concentration of 25 mg/L, revealing a removal rate of 25% after 30 minutes of ultrasound treatment (60 kHz, 10 minutes application, and 500 W). This study further validated the trend of increased CIP removal when ultrasound treatment was combined with another advanced oxidation process. The combined processes of US, US/ZnO, and US/ZnO/PS achieved removal rates of 35.93%, 70.48%, and 99.48%, respectively, at the end of 180 minutes.

In the context of ultrasound-enhanced adsorption for copper removal, in the study conducted by Gupta et *al.* [88], the removal rates after 1 minute reached 80% with the adsorbent beeing water melon shell and ultrasound treatment power of 90 W.

The study by Secondes et *al.* [89] focused on a hybrid process that combined ultrasound irradiation (35 kHz) with activated carbon adsorption to tackle emerging contaminants (ECs) in synthetic wastewater. This approach demonstrated enhanced adsorption capacity with ultrasound treatment. For consequence, the improved removal was attributed to the combined effects of enhanced adsorption and sonolytic degradation.

Like the case with Ciprofloxacin, ultrasonic treatment in conjunction with hydrous iron oxide proved effective in reducing the final solution concentration of copper species in the pH range of 7.5 to 9.5 [90].

Regarding the use of Kaolin as an adsorbent enhanced by ultrasound, specific studies in the literature are limited. However, previous research has confirmed the efficiency of kaolin in heavy metal removal

through adsorption, however there is a lake on the literature for the combination between acoustic cavitation and Kaolin [91].

2.2.3 General Wastewater Treatment Enhanced by Ultrasound

The research on ultrasound cavitation's impact on wastewater presents intriguing findings, particularly when combined with other Advanced Oxidation Processes (AOPs). In a study by Rossi et *al.* [92], the synergistic effect of ultrasound (24 kHz and 250 W) and ozone was explored in treating primary effluents. This combined process exhibited remarkable removal efficiencies for various contaminants, including soluble Chemical Oxygen Demand (sCOD) at approximately 60%, formaldehyde at about 50%, and Methylene Blue Active Substances (MBAS) at over 90%. Additionally, the process displayed significant disinfection capabilities, achieving a 4-log reduction for E. coli and a 5-log reduction for Total Coliforms.

In another investigation employing a sono-electrocoagulation system, Arka et *al.* [93] achieved removal rates of 97.5% for COD and complete color removal. The study highlighted that COD and color removal rates were enhanced at pH levels of 6, 7, or 8, but decreased in other pH ranges.

Serna-Galvis et *al.* [94] explored the cavitation effect of ultrasound (375 kHz and 88 W/L) on 17 emergent pollutants in water, both in isolation and in combination with other techniques. After 90 minutes, the concentrations of certain compounds increased when submitted to ultrasound treatment alone. However, when combined with other processes like sono-Fenton, sono-photo-Fenton, and sono-photo-Fenton/oxalic acid, the degradation of pollutants was enhanced. Similarly, Serna-Galvis et *al.* [95] with the same ultrasound treatment parameters, observed an increase in the concentration of certain pollutants (Ciprofloxacin, Norfloxacin and Carbamazepine) after applying ultrasound for 90 minutes. The combination of ultrasound treatment with Fe^{2+} and UVC light further increased pharmaceutical removal, leading to an average removal of the pollutants around 85%, with some of them reaching the total removal.

Chandak et *al.* [96] investigated the removal of pharmaceuticals from wastewater and studied the variation of COD removal across various processes. The study found that while ultrasound treatment alone (250 W and 22 kHz) achieved a COD removal of 14%, when combined with processes like hydrogen peroxide or ozone, the removal rate more than doubled (36%). The maximum COD removal percentage (92%) was achieved by combining ultrasound with ozone and copper oxide, highlighting the significance of an oxidizing process for process enhancement.

Finally, Vásquez-López et *al.* [34] focused solely on the effect of ultrasound treatment (26 kHz and 1333.3 W/L) on wastewater without combining it with other processes. After 30 minutes of application,

the study found significant removal rates: TOC removal at 68.7%, COD at 39.9%, BOD5 at 39.5%, TN at 50%, NH3-N at 67.8%, TP at 37.3%, and PO4-P at 42.5%. Notably, there were negligible variations in pH, a decrease in conductivity, and only a minor reduction in dissolved oxygen (0.8 mg/L).

The findings derived from the referenced literature indicate that acoustic cavitation enhances pollutant removal when combined with other Advanced Oxidation Processes (AOPs). A comparative analysis of the results obtained by Vásquez-López et *al.* [34] with those of Serna-Galvis et *al.* [94] and Serna-Galvis et *al.* [95] reveals a notable disparity in power intensity. Specifically, the power intensity in the former case is approximately 15 times higher than in the latter studies. Since that the acoustic cavitation is more intense, it leads to superior removal rates once that the cavitation is more intense.

While the results underscore the potential of acoustic cavitation as a valuable tool for wastewater treatment and pollutant removal, it is noteworthy that the ultrasound treatment parameters employed by Vásquez-López et *al.* [34] may pose scalability challenges. The parameters necessitate a substantial amount of energy, coupled with large transducers, or alternatively, result in a low quantity of treated water flow. A comparative examination of this study with the research conducted by Chandak et *al.* [96] reveals that ultrasound treatment, when combined with other AOPs, achieves high COD removal while utilizing less power. This combination leverages the advantages of both processes, offering a more sustainable and efficient approach to wastewater treatment.

2.3 Effects of Cavitation on Wastewater treatment

Cavitation encompasses the intriguing physical phenomenon wherein bubbles or voids are formed within a liquid due to exposure to significant negative pressure conditions. The size of these bubbles can range from nanometres to substantial centimetres. Cavitation can be induced through two primary methods, by generating considerable tension within a liquid or by introducing an amount of energy locally within the liquid. In this context, this study will lies on the former method, specifically acoustic cavitation and the effects of cavitation in liquids [97].

Cavitation can be associated with either liquid flow or acoustic conditions. When there is a rapid pressure fluctuation within a hydraulic system, the liquid's pressure drops until it reaches its vapour pressure, leading to the creation of bubbles. Subsequently, upon pressure restoration, the liquid swiftly moves away from the low-pressure zone, causing the bubbles to collapse. This collapse generates shock waves and elevates the surrounding liquid's temperature [98]. It is worth noting that cavitation becomes evident once the pressure falls below a certain threshold, signifying a loss of liquid cohesion [99].

The relationship between vapour pressure and cavitation finds elucidation through a phase diagram, Figure 2.5. This diagram expounds on the behaviour of water under specific temperature and pressure conditions. It becomes evident that by elevating the temperature of water (while maintaining constant pressure), the transition to the vapour state becomes attainable. Conversely, reducing the pressure, as observed in cavitation, pushes water below this delineated line, leading it into the vapour domain [100].

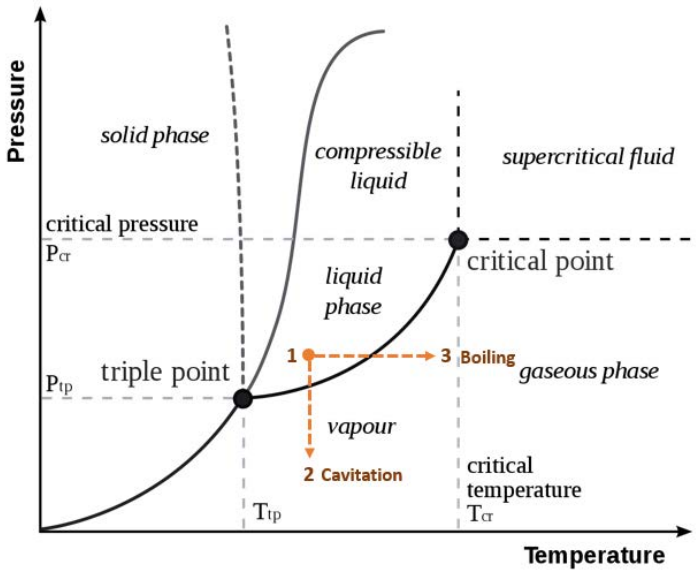

Figure 2.5: Water phase diagram. The passage from liquid to vapour can occur by decreasing the pressure like seen in cavitation (1-2) or increasing the temperature (1-3). Image adapted from Franc et *al.* [99].

Acoustic cavitation hinges on the emission of high-frequency sound waves through the liquid medium [101]. These waves are generated by ultrasound devices that acts on the liquid, leading to alternating compressive and tensile phases, fostering bubble formation and expansion [102]. The cavitation event itself occurs during the tensile or rarefaction phase, characterized by a negative pressure environment. Within this phase, the negative pressure surpasses a critical threshold, leading to the separation of liquid molecules. This occurs as the distance between adjacent molecules exceeds a critical value. This critical point, termed the "threshold," signifies the juncture at which the molecule distance becomes sufficiently extensive to induce bubble formation [13, 48, 101].

These bubbles emerge when the liquid's pressure declines to a level that encourages vaporization, known as the rarefaction phase. This phase leads to the creation of minuscule gas-filled pockets, often referred to as bubble nuclei [102]. Bubble nuclei can either grow if mechanisms support their expansion or dissolve if no sustaining process is present. These bubbles undergo oscillations in size due to the cyclical shifts between rarefaction and compression phases. As illustrated in Figure 2.6, bubble size experiences

continuous enlargement due to the gas's compressibility within [103].

Bubble or nuclei growth, is propelled by two primary processes: rectified diffusion and bubble coalescence. Research conducted by Ashokkumar [103] has explored bubble growth behaviour in diverse mediums. In solutions featuring active solutes, which will be further discussed in the context of wastewater, bubble growth is predominantly constrained to rectified diffusion. The presence of surface-active solutes retards bubble coalescence, amplifying the importance of rectified diffusion. However, it is important to note that water exhibits both processes simultaneously. Bubble coalescence pertains to the fusion of two or more bubbles into one. When bubbles amalgamate, their boundaries collapse, forming a fresh, larger boundary encompassing the merged bubble [103, 104]. This phenomenon is inherently connected to rectified diffusion, which signifies the migration of molecules in one direction due to external driving forces or gradients. Refer to Figure 2.6 for a visual representation of this process. After the initial appearance of nuclei, if multiple mechanisms exist, coalescence unites certain bubbles, leading to their growth. This coalescence process combines with rectified diffusion, accelerating bubble expansion. Once a bubble reaches its resonance size, it collapses and fragments into the liquid, seeding new nuclei that initiate the next cycle.

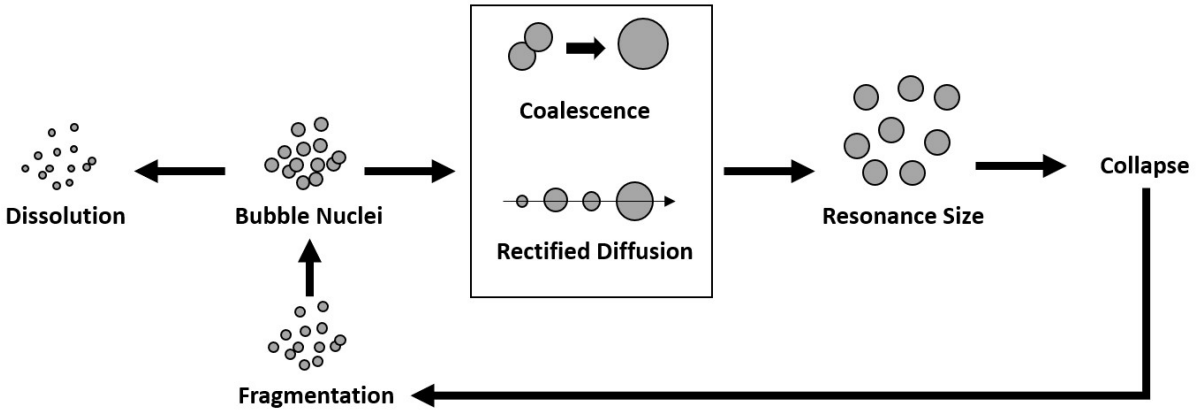

Figure 2.6: Process of bubble formation and growth in cavitation. Bubble nuclei form, grow, and reach a critical size, causing implosion and fragmentation. This cycle recurs. Image adapted from Ashokkumar et *al.* [103].

Diffusion takes the main paper in presence of some solute, which makes it the most interesting process to be studied. The rectified diffusion is connected to the gas inside the bubble. This last one, during the compression phase, has a pressure higher than at equilibrium and, consequently, gas diffuses out of the bubble. Amid the expansion phase, the gas diffuses inside the bubble. However, comparing the surface area of the bubble in compression and expansion, the expansion phase has a large area [105].

Therefore, the gas inside the bubble will increase because the amount of input or output flux is proportional to the surface area (exchange area). Another consequence of these size changes will be the increase of diffusion effect during the compression, as seen in Figure 2.7. In compression, the liquid shell will be more concentrated, which means that the diffusion is higher. In the expensive phase, the concentration is lower, thus, the diffusion will be reduced [106]. The rectified diffusion is the cause of the bubble growth along the cycles. This growth will be continuous until the bubble reaches its resonance size when the bubble oscillating frequency is in the same range as the driving ultrasound frequency. At this point the pressure is high, assisted by the compressive stress and the effect of surface tension, and the bubble will be forced to shrink or collapse. This process is approximately adiabatic, so it reaches a very high temperature in the compression phase [102, 104, 107].

The liquid will heat over the ultrasonic wave propagation through the liquid that will be scattering and attenuated. Liquid convection is a consequence of the two previously mentioned, micro-streaming and acoustic streaming. Micro-streaming is the consequence of the expansion and shrinking of the gas bubbles during the cavitation. When a bubble is vibrating, there are currants around it, generating the flow known as micro-streaming. Acoustic cavitation provokes convection once the wave sound propagation along the liquid causes the liquid to flow in the direction of the sound propagation. The propagated ultrasound pressure causes radiation forces, standing waves and acoustic streaming [108].

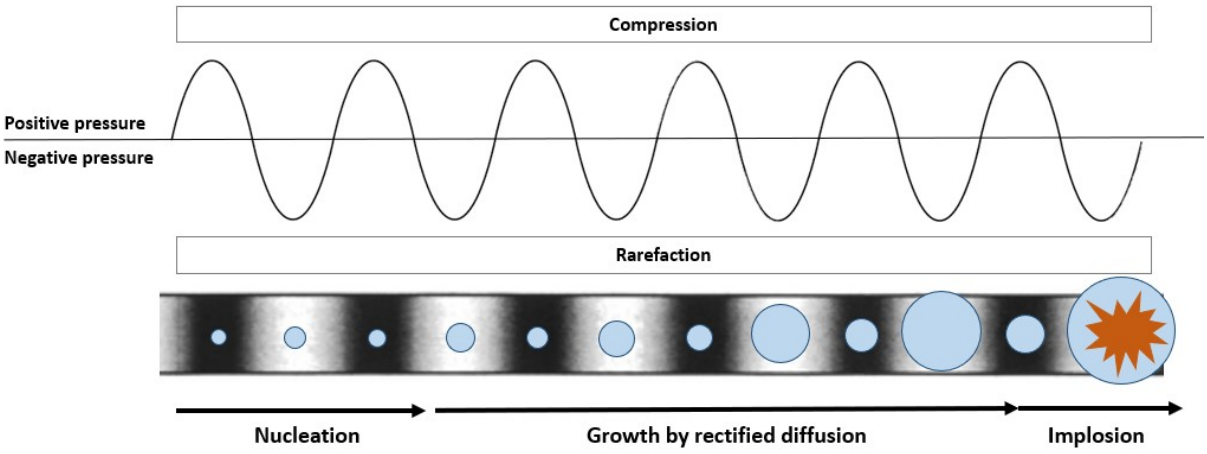

Figure 2.7: Impact of the Pressure Variation on the Formation and Growing of Bubbles. The constant compression and rarefaction lead to nucleation, growth by rectified diffusion, ending with the implosion of the bubble. Image adapted from Mason et *al.* [105].

Cavitation initiation occurs only when the surface tension of the liquid is overcome. As previously mentioned, the critical pressure, or cavitation threshold, is determined by the following equation:

$$P_{crit} = P_v - 2 \cdot \frac{\gamma}{R} \tag{2.3}$$

Where R (m) is the bubble size, P_v (Pa) is the vapour pressure of the liquid and γ (N/m) the surface tension [11].

Cavitation can be categorized into transient or stable [102]. Both occur at low ultrasound intensities, but transient cavitation exists for a limited number of cycles and is particularly efficient for inducing chemical reactions [109]. In contrast, stable cavitation transpires when bubbles oscillate consistently across many cycles, leading to micro-streaming within the surrounding liquid. These microbubbles, comprised solely of gas, such as air, exhibit a longer lifespan than one ultrasound cycle. As frequency increases, the bubbles are propelled toward the pressure antinode, sparking certain chemical reactions [110].

Bubble remnants are not entirely dissolved into the surrounding fluid, and the remaining gas from implosion ascends to the liquid interface. This process serves as a method for degassing the liquid. This phenomenon is observed in cavitation bubbles with modest dimensions, which induce robust flow (micro-streaming). Furthermore, if the bubbles don't reach resonance size, they will grow through the diffusion of gas molecules from the surrounding liquid, ultimately achieving a stable equilibrium size. This indicates the establishment of stable cavitation, commonly exploited in medical applications like ultrasound imaging and drug delivery [102].

On the contrary, transient cavitation entails bubbles filled with gas undergoing erratic oscillations and ultimately imploding. The duration of this phenomenon is shorter compared to stable cavitation. The cavity is rapidly formed and collapses energetically after just a few cycles, resulting in elevated local temperatures, pressures, and shear forces that can disintegrate biological cells or other organic materials present [102].

Within the context of cavitation, the collapse of bubbles can be delineated into three distinct phases, as illustrated in Figure 2.8 [7, 111]. The initial phase, centred at the thermolytic core, experiences extreme conditions with temperatures ranging from 4000 to 5000 K and pressures reaching approximately 500 atm. Remarkably, despite the elevated temperatures, this overheating stage persists for less than 10 μs [112]. During this phase, water molecules inside the bubble undergo pyrolysis, yielding $HO^{\cdot}$ and $H^{\cdot}$ radicals.

The subsequent phase occurs at the interface between the cavitation bubble and the surrounding liquid. In this region, analogous chemical reactions take place, alongside processes such as the dimerization of $HO^{\cdot}$ to form H_2O_2. The primary mechanism involves the attack of free radicals emanating from the implosion of cavitation bubbles [7].

The final phase encompasses the bulk region, where the increase in temperature is inferior due to the adiabatic nature of cavitation reactions. Within this bulk region, the radical attack on pollutants is anticipated to occur under the influence of H_2O_2. As depicted in Figure 2.8, these three phases exhibit distinct temperature and pressure conditions. The outermost bulk region experiences minimal impact, with the middle phase seeing a temperature rise to around 2000 K and negligible pressure changes. However, in the central region, known as the hotspot zone, temperatures and pressures reach remarkable values [109, 113].

As consequence, the chemical effects of cavitation manifest on the previous distinct regions, Figure 2.8. In the hot gas phase within the bubble, solvent or volatile compound sonolysis occurs, resulting in the formation of radicals. The high pressure and temperature in this phase lead to sonolysis of non-volatile compounds and subsequent heating of the liquid. At the liquid shell around the bubble, gradients in pressure, temperature, and the presence of an electrical field result from the sonolysis of non-volatile compounds. The chemical reactions observed are a consequence of the radicals originating from the interior of the bubble. In the surrounding liquid medium, the reactions occur as a consequence of the radical reactions expelled from the interior of the bubble. These processes encompass emulsion formation, mixing of bubble gas and liquid, mechanical effects on solids and metals, heat transfer and fluid flow [106].

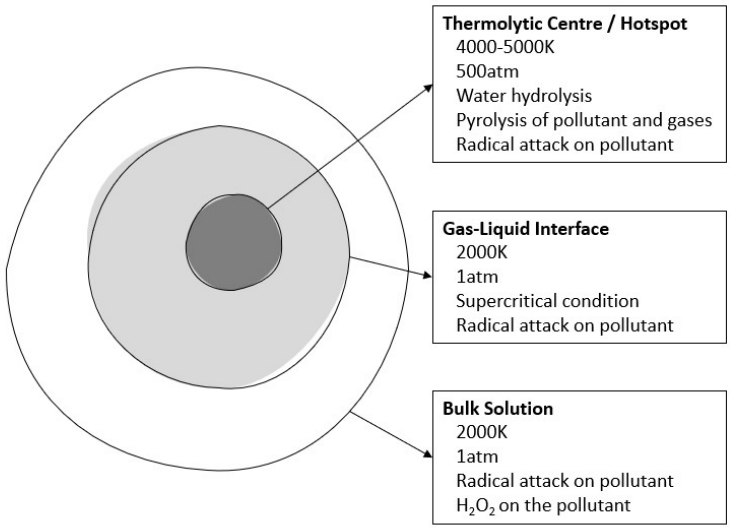

Figure 2.8: Hotspot, gas-liquid interface and bulk solution regions and their characteristics during bubble implosion. Image adapted from Carpenter et *al.* [111].

In the realm of cavitation, where bubbles collapse in three distinct phases, as depicted in Figure 2.8 [7, 111], it is essential to consider the dramatic contrast between initial and final bubble conditions. Starting with an initial radius of approximately 1 μm, the internal pressure at 1 atm, a temperature of 20

°C, and an energy density of around $10^6\ eV/\mu m^3$, these parameters can exhibit some variability under specific conditions. As the bubble collapses, its radius can range from 3 μm to 0.4 mm, the internal pressure can rise to 2500 atm, the internal temperature can peak at 6000 K, and the energy density can reach $2.8 \times 10^8\ eV/\mu m^3$ [114].

These elevated temperature conditions exert a considerable influence on the overall solution temperature. In a study by [115], the kinetic isotope effect was investigated, revealing a temperature range of 1000-4600 K. This range is attributed to specific regions within the cavitation hotspot. Furthermore, in a separate experiment involving multibubble sonochemistry and sonoluminescence, the same author proposed an extended temperature range of 750-6000 K [115].

The temperature-dependent radical production, influenced by frequency, is a critical factor in the chemical effects of cavitation. Radicals are generated during the collapse of the bubble from the solvent vapour or volatile compounds in the liquid. This initial radical acts as a catalyst, initiating a chain reaction of radical formation, ultimately leading to reactions with substrates or other radicals [106]. The reaction rate is slow, ranging from 10^{-4} to 10^{-5} mol/(L · min), and is not influenced by the ultrasound.

2.3.1 Variables Affecting Sonochemical Reactions

The implosion of bubbles, accompanied by intricate chemical and physical processes, underscores the significance of sonochemistry. This term succinctly encapsulates its essence: the study of chemistry in the presence of sound, specifically ultrasound waves. Sonochemistry employs high-frequency and high-power sound waves to infuse energy into a liquid reaction mixture, leading to both physical and chemical transformations within the liquid [109]. This field finds applications in diverse areas, including food processing, oil emulsion stabilization, particle size reduction, filtration systems for suspended particles, homogenization, atomization, and environmental protection [109].

As refereed before, when bubbles collapse during cavitation, they release a substantial amount of heat, reaching temperatures as high as 5000 °C, and generate extreme pressure conditions, often exceeding 1000 bar [109]. This phenomenon is known as the "Hot-spot theory," emphasizing the localized and drastic conditions created by bubble collapse.

At a frequency of 20kHz, transient bubbles form, with their maximum radius ranging from 10 to 50 μm, dependent on the acoustic pressure amplitude. Importantly, cavitation collapse is frequency-dependent, with bubble size decreasing as frequency increases [106, 109].

As bubbles collapse to their maximum radius, their shell velocity approaches the speed of sound. When bubble size reaches the sub-micron range, the gas inside the bubble decelerates the wall motion,

giving rise to the generation of awe-inspiring shock waves [106].

The collapse of bubbles also significantly influences the flow of liquid in aqueous environments. In cases where bubbles do not collapse uniformly, they generate liquid jets, causing liquid to rush into the bubble. This phenomenon becomes particularly pronounced at boundary areas where a liquid interfaces with a solid surface. Finding a perfectly spherical bubble with homogeneous collapse in practice proves to be a challenging endeavour [106].

To neutralize microorganisms, several mechanisms come into play, all stemming from acoustic cavitation in the aqueous medium. First, the collapse of bubbles generates shock waves and vortices, creating shear stress within the liquid bulk, which exceeds the shear rate throughout the liquid [13, 112].

Secondly, the physical and chemical consequences of bubble collapse, such as high temperature and pressure increases, result in changes to microorganisms. These changes are further influenced by the presence of hydroxyl radicals, which are formed as a consequence of the hot-spot hypothesis. During bubble collapse, free radicals are generated [13, 112].

The action of ultrasound leads to the disintegration of water molecules, forming hydroxyl radicals:

$$H_2O \rightarrow HO + H \tag{2.4}$$

These hydroxyl radicals, $HO^{\cdot}$, interact directly in the gaseous phase or at the liquid/gas interface. Their reaction with oxygen results in the formation of hydrogen peroxide [116]:

$$H_2O + H^{\cdot} \rightarrow HO^{\cdot} + H_2 \tag{2.5}$$

$$O_2 + H^{\cdot} \rightarrow HO_2^{\cdot} \tag{2.6}$$

$$2HO^{\cdot} \rightarrow H_2O_2 \tag{2.7}$$

$$HO^{\cdot} + H_2O_2 \rightarrow H_2O_2 + HO_2^{\cdot} \tag{2.8}$$

These chemical reactions lead to the formation of hydrogen peroxide, which further affects microorganisms:

$$H_2O_2 \rightarrow 2HO^{\cdot} \tag{2.9}$$

$$HO^{\cdot} + HO_2^{\cdot} \rightarrow H_2O + O_2 \tag{2.10}$$

$$H_2O_2 + H^{\cdot} \rightarrow H_2O + HO^{\cdot} \tag{2.11}$$

These intriguing chemical reactions culminate in the formation of hydrogen peroxide, exerting further influence on microorganisms. The radicals mentioned above infiltrate the chemical structure of bacterial cell walls, ultimately leading to their degradation. Furthermore, the physical, chemical, and mechanical effects discussed earlier also contribute to the disruption of bacterial cells and the de-agglomeration of clusters. The neutralization of microorganisms is driven by cell dilution and the growth of free radicals. One of the mechanisms responsible for cell neutralization is the physical disruption of the cell over time, a result of mechanical fatigue. Additionally, micro-stray shear forces, chemical attacks by free radicals, and the impact of bubble collapse near the cell wall all contribute to this process Moreover, hydroxyl radicals play a crucial role in the oxidation of pollutants. High rates of successful recombination of hydroxyl radicals lead to high rates of oxidation, making this process dependent on the cavitation process and chamber design [112].

These intricate processes within sonochemistry, from the generation of shockwaves and vortices during bubble collapse to the formation of hydroxyl radicals, culminate in the remarkable disruption and neutralization of microorganisms. This orchestration of physical, chemical, and mechanical effects, illustrated in Figure 2.9, demonstrates the profound potential of sonochemistry in applications such as wastewater treatment and environmental protection, where the targeted dismantling of cells plays a pivotal role 2.9.

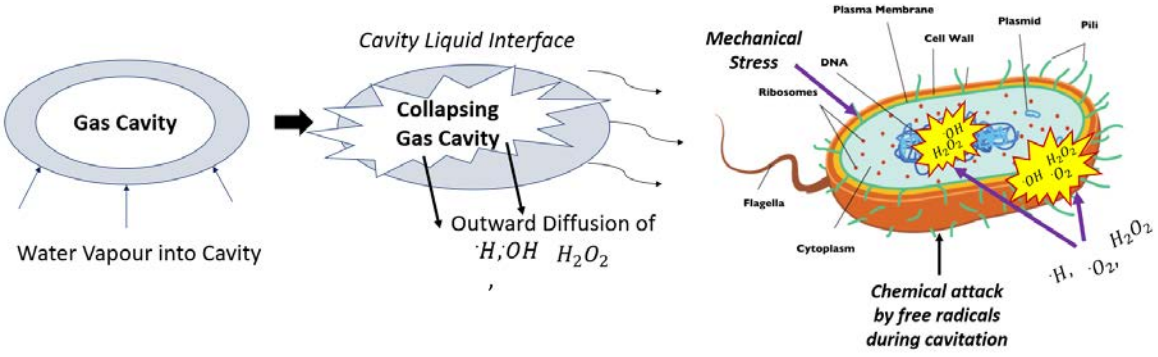

Figure 2.9: Sequence of Cellular Degradation by Cavitation. It begins with gas cavity formation due to increased water vapour. The ensuing collapse releases destructive radicals, leading to cellular destruction, augmented by mechanical stress from implosion. Image adapted from Fetyan et *al.* [97].

Numerous factors can influence cavitation and, consequently, the outcomes of sonochemical reactions. These factors include acoustic power, frequency, hydrostatic pressure, the nature and temperature of the solvent, the gas used, and the reactor's geometry [48].

Acoustic intensity, as indicated in Equation 2.12, varies with power input or the transmittance

area of the ultrasonic transducer. Higher intensities result in increased hydroxyl radical concentration and enhanced mass transfer, leading to greater degradation of organic substances [117].

However, this phenomena it is limited to a maximum power. Beyond a certain power threshold, bubble radius tends to stabilize, limiting degradation [48]. This behaviour holds for various types of pollutants, including hydrophilic [118], hydrophobic [119], and volatile compounds [120].

$$I_a = \frac{P_s}{A} \tag{2.12}$$

Where I_a is the acoustic intensity (W/m^2), P_s is the input power (W) and A is the transmittance area (m^2) of the ultrasound.

The behaviour of cavitation collapse hinges on the applied **frequency**, dictating bubble size and the maximum collapse temperature. Lower frequencies yield a modest temperature rise, akin to an isothermal collapse scenario. Conversely, elevating the frequency reduces bubble size, resulting in shorter collapse durations. Typically, the highest collapse temperature is observed around 300 kHz, signifying a shift towards nearly adiabatic collapse [106].

Research by Al-Bsoul [121] demonstrated the greater effectiveness of lower-frequency ultrasound (20 kHz) compared to higher frequencies (40 kHz) in wastewater treatment, achieving a COD removal of 30% versus 14%, respectively. Lower frequencies may be more efficient for wastewater treatment applications. Higher frequencies, between 200-350 kHz, lead to increased radical formation and greater hydrogen peroxide accumulation [122]. Highly hydrophobic or volatile substances require higher frequencies for efficient degradation [48].

In relation to frequency, ultrasound irradiation can be administered through two methods: continuous or pulsed. The continuous method is the most commonly employed due to its process simplicity. However, certain studies have reported that the pulsed technique exhibits greater efficacy in eliminating pollutants. Xiao et *al.* [123] and Xiao et *al.* [124] shows that using pulses, instead of continuous irradiation, allows to accumulate hydrophobic pollutants in the bubble interface, inducing higher levels of molecule degradation upon collapse.

Temperature significantly influences sonochemical reactions by altering fluid properties. Increasing temperature decreases viscosity and surface tension while increasing vapour pressure, reducing violent collapses due to increased vapour inside bubbles. The solvent's boiling point is another critical factor; solvents further from their boiling points generate more cavitation bubbles, but these dampen bubble collapses and hinder sonochemical effects [106].

Cavitation is more pronounced at lower temperatures, where high temperatures disrupt solute-matrix

interactions (hydrogen bonding, dipole interactions, and Van der Waal forces), resulting in faster diffusion rates and less violent collapses [109].

The smaller the thermal conductivity of the gas inside the bubble, the higher the maximum collapse temperature [106].

Generally, lower temperatures (25°C to 30°C) favour cavitation [10]. For applications emphasizing thermal effects, lower temperatures are advisable [125].

For an ultrasound intensity of 20 kHz, increasing temperature reduces pollutant degradation [126]. Studies on 2,4-Dichlorophenol, 4-Chlorophenol, Dextran, and Diazinon confirmed that higher temperatures lead to reduced degradation [126–129]. Lower initial temperatures (20°C) are more effective for decolorization compared to higher temperatures (30°C and 40°C) [18].

K. Brabec et *al.* [130] research indicated an inverse relationship between cavitation threshold and temperature; as temperature increases, cavitation threshold decreases. Additionally, the cavitation threshold tends to increase with higher viscosity.

While it is acknowledged that parameters such as pH and initial solvent concentration can exert influence on sonochemical behaviour, it is important to note that these factors will not be the focus of this study.

2.3.2 Ultrasound Components and Functioning

Before defining ultrasound is important to specify what is sound. Sound is a form of energy that is produced in consequence of disturbs or vibrations in a medium (air, water, solids), and may come from vibrating bodies, airflow changing, heat sources or supersonic flow. It is a mechanical energy transmitted in gas, liquid or solid form by pressurized waves [97]. These vibrations cause pressure waves that will propagate through the medium, generating series of compression and rarefaction. Waves have some interesting particularities that will impact the way how sound will be propagated. A wave can transport energy and information through a medium, without transport the medium itself [110, 131].

Ultrasonic waves belonging to the range between 20 kHz and 200 MHz. Above it, the ultrasonic frequencies are not able to produce acoustic cavitation. In normal conditions, the maximum listened sound range for humans, is from 16 kHz to 18 kHz. The ultrasound frequencies are considered from 20 kHz and dependent of the application can go to 2MHz. The conventional ultrasound frequencies for industrial applications are from 20 kHz to 100 kHz and are considered as low ultrasound frequencies. To sonochemistry, are used frequencies in the 100 kHz-2 MHz range and since 5 MHz to 10 MHz, it is nominated as low power high frequency ultrasound and it is used for medicals diagnostic purposes

[48, 106]. The intensities higher than 10GHz are mentioned as hyper sound. In Figure 2.10 can be seen the sound range along all frequencies.

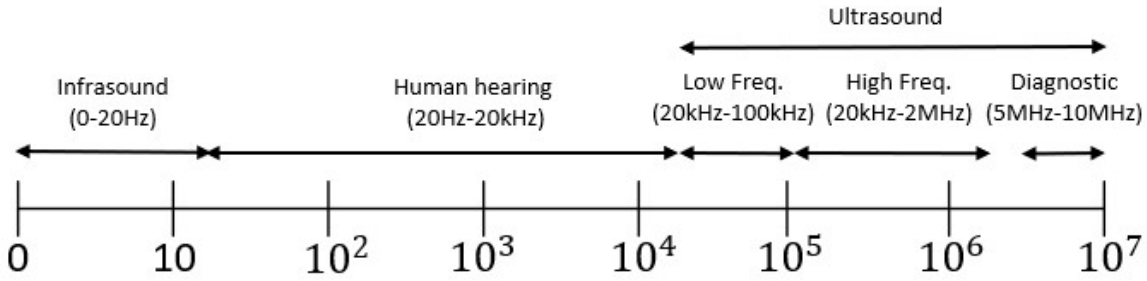

Figure 2.10: Sound range along the spectrum and the position of the different types of ultrasound, low frequency ultrasound, high frequency ultrasound and ultrasonic spectrum used in medical diagnosis. Image adapted from Fetyan et *al.* [97].

A sound wave, under ideal conditions, can be described as a sinusoidal plane wave characterized by several key parameters, including frequency, period, wavelength, and amplitude [131, 132]. These parameters help to understand the fundamental properties of sound waves. Frequency (f) in Hz, represents the number of cycles a wave completes per second and is the inverse of the period (T) in seconds, which is the time required to complete one cycle.

$$f = \frac{1}{T} \tag{2.13}$$

The amplitude characterizes the variation in pressure over time. It can be mathematically represented as:

$$A(t) = A_{max} \cdot \sin(2\pi t + \omega) \tag{2.14}$$

Here, A_{max} represents the maximum amplitude (μm), t represents time (s), and ω is the angular velocity (rad/s).

The propagation of sound waves is influenced by the distance they must travel through a medium, and two main factors come into play: scattering and absorption. Scattering refers to sound waves reflecting in various directions from their original path, while absorption involves the conversion of sound energy into other forms of energy [109]. Attenuation, which measures the reduction in ultrasonic intensity, help to understand the factors that decrease ultrasonic intensity as sound travels through a medium.

Pure water, without any other substance, possesses an attenuation coefficient of $2{\cdot}10^{-7}$ cm^{-1}, indicating that over a 1 km distance, the attenuation is only 2%. This low coefficient makes water an

excellent medium for transmitting acoustic signals over long distances. For instance, at 20 kHz, the typical length is 7.4 cm. Considering the Rayleigh scattering cross-section of wastewater particles, their presence has negligible effects on ultrasound attenuation in wastewater [11, 133].

Air bubbles in water create interfaces between air and water, making them highly reflective to ultrasound due to the substantial difference in acoustic impedance between these media. Bubbles reflect ultrasound waves effectively because this impedance difference spans approximately four orders of magnitude. However, bubbles can also attenuate sound transmission, especially in situations involving dense bubble clouds or resonance with the ultrasound frequency [11].

Ultrasound waves are introduced into the liquid medium either via direct contact with the ultrasonic source (direct sonication) or by immersing a vessel containing the solution to be treated (indirect sonication). Indirect sonication consists of a piece that includes a transducer coupled with a vibrating plate for the bath method [134].

The horn system is constituted by an ultrasonic electrical generator, an electro mechanical/piezoelectric transducer, an wave guide, an ultrasonic horn or acoustic radiator, a mounting flange, a reactor chamber and a working liquid inlet and outlet, Figure 2.11. In some cases, there are other components such a cooling system with their respective pipes [135].

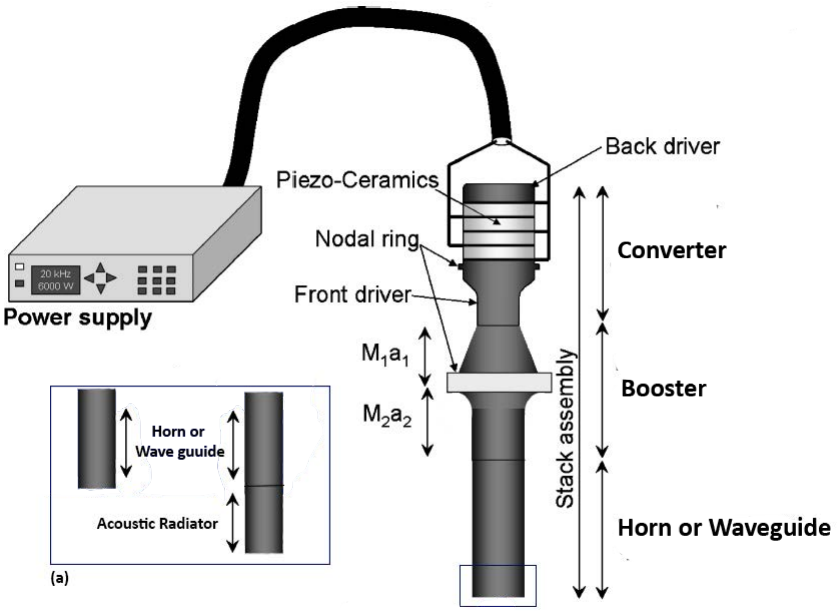

Figure 2.11: Typical configuration of an ultrasound device for water treatment application. (a) The ultrasound tip consist of a horn emitting waves perpendicular to the ultrasound axis. Alternatively, it may involve a waveguide and an acoustic radiator. Image adapted from Marin-Hernandez et *al.* [136].

Transducer or converter is the part responsible to convert the electrical energy into mechanical energy, vibration. The ultrasound basis is a source of high-energy vibrations. In practice, the source is one transducer that is capable of convert electrical energy into mechanical energy in the form of ultrasonic vibrations. There are three classic types of transducers, gas driven, liquid driven and, the most efficient, the electro mechanical. However, to high power vibrations, are considered two types: piezoelectric and magneto strictive [48, 136].

In this work will be focus on the use of piezoelectric transducers. Piezoelectric materials can respond in two different ways according to the stimulus applied. If there is a mechanical load, the material responds producing an electrical potential. However, if there is an electrical potential applied across faces there is the inverse piezoelectric effect [109, 137].

The transducer construction is normally made by the assembly of layers with blocks or discs of aluminium and with electrically active piezoelectric elements. This particular configuration can be thought of as a mechanical transformer and behaves similar to a bell when excited by a driving piezoelectric element at its resonant frequency. When appropriately stimulated, the system resonates and produces a characteristic "ringing" sound due to the transfer of mechanical energy between different parts of the configuration [137]. A screw or pin compress the two blocks of metal (superior and inferior layers) again the piezoelectric ceramic plates. This configuration it will be responsible for the introduction of a force into the piezoelectric ceramics [138].

When an external force is applied, the electric dipoles within the crystal align, creating a positive and negative face, resulting in an electric field across the crystal. This phenomenon occurs in a poled piezoelectric material, where subjecting it to tensile or compressive stress generates positive or negative voltage across its faces, respectively [139].

This crystal then converts electrical energy into mechanical vibration, producing sound through alternated potential at high frequencies. When the alternating potential reaches a sufficiently high frequency, it generates high-frequency sound waves, commonly known as ultrasound [109]. Essentially, a zirconium titanate piezoelectric transducer converts electrical pulses with periodic intervals into ultrasound pulses [133]. In this process, the application of an external voltage to a poled piezoelectric material causes the material to either extend or compress, depending on whether the voltage is positive or negative [139].

To achieve high-amplitude oscillations, certain physical properties of the ceramic material must be taken into account. Three key properties play a crucial role in ensuring the effective functioning of the piezoelectric ceramic. Firstly, a high Curie temperature, which is the temperature at which certain

materials transition from a ferromagnetic or ferroelectric state to a paramagnetic or paraelectric state [138]. Secondly, a low dissipation factor is essential to prevent overheating and prolong the ceramic's lifespan. Lastly, a high "d" constant, which signifies a high ratio of mechanical strain produced by an applied electromagnetic field [137]. In essence, a high d ratio implies that a small mechanical deformation in the material will result in a large electrical signal, and vice versa, enhancing the conversion of energy between electrical and mechanical domains.

The distinction between the direct and indirect piezoelectric effects lies in the direction of the electrical impulse as seen in Figure 2.12. When a mechanical impact occurs, the crystals generate a potential difference that can be read by a device. Conversely, the opposite effect results in the generation of ultrasound waves [138]. The former principle is employed in applications like acoustic and pressure sensors [140, 141]. The latter principle underlies the emission of ultrasonic waves [142].

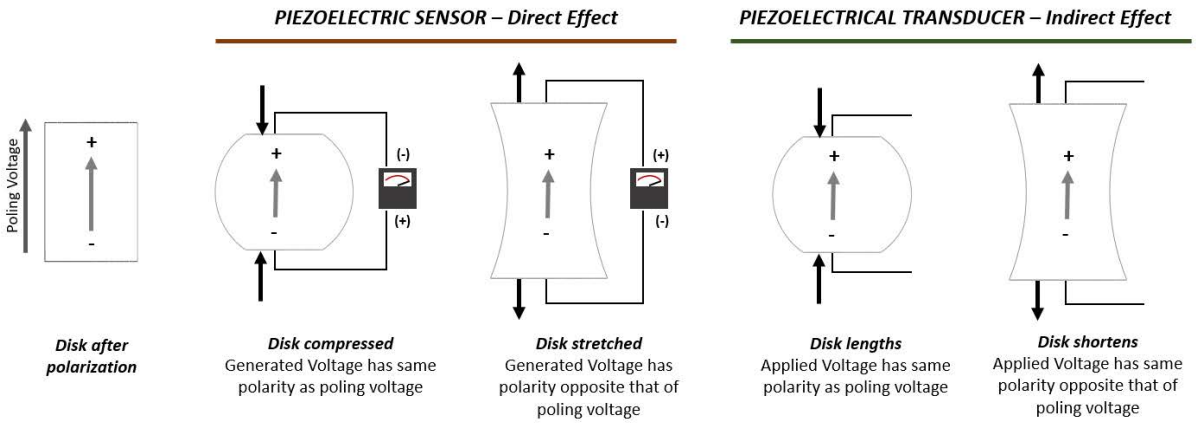

Figure 2.12: Piezoeletric disk response with two different exciting possibilities. Mechanical force yields voltage (direct effect for sensors); applied voltage induces dimensional change (indirect effect for transducers). Image adapted from Sikalidis et *al.* [139].

Guided waves are a category of waves that propagate along a defined path within a medium or structure, as opposed to radiating outward in all directions like free or unguided waves. Their propagation is confined by the geometry and boundaries of the medium itself, resulting in distinct characteristics. Ultrasonic guided waves serve as an exemplary instance of guided wave propagation and exhibit typical attributes [143].

One key feature of guided waves is their constrained path, determined by the medium's geometry. This confinement leads to reduced dispersion when compared to free waves over long travel distances. However, guided waves are not entirely immune to dispersion. Different frequencies within the wave can travel at varying velocities, which can result in mode separation and frequency-dependent behaviour [143].

In the context of wastewater treatment, the primary objective of utilizing **waveguides** is to channel ultrasonic waves along the z-axis towards the target structure, such as the acoustic radiator [144]. However, as the waveguide it is in contact with the fluid, it will works as a acoustic radiator too in certain point. These waveguides can take different forms: they can be either solid or perforated with holes.

Solid waveguides are characterized by their rigidity and inability to displace along the z-axis. They provide a stable and predictable path for the ultrasonic waves. However, they may involve some losses and dispersion during wave propagation. On the other hand, perforated waveguides feature holes that permit movement along both the negative and positive axes of the z-axis. The presence of these perforations offers advantages such as reduced losses and dispersion during wave propagation. Additionally, perforated waveguides enable the transmission of non-continuous waves, which can be particularly beneficial in various wastewater treatment applications.

Waveguides play a critical role in ensuring efficient and controlled delivery of ultrasound waves to target structures within wastewater treatment systems. They serve as conduits for these guided waves, allowing for precise energy deposition and effective treatment of contaminants. Understanding the properties and advantages of different waveguide designs is essential for optimizing the performance of ultrasound-based wastewater treatment processes.

The **booster** serves to amplify the amplitude generated by the preceding component, while the horn transmits mechanical energy in the form of ultrasonic waves into the aqueous medium. Both components are meticulously engineered to operate at specific frequencies, often designed to be half a wavelength in length, although alternative configurations, such as full-wavelength designs, are feasible and contingent upon the intended application [145].

In certain applications, the booster has the capability to alter the wavelength. However, in the context we are investigating in this study, it functions primarily as a waveguide, preserving the original wave characteristics. In this role, it acts as an integral structural element. Conversely, the booster plays a pivotal role in the structural integrity of the ultrasound system, as it facilitates the connection between the internal waveguide and the flange. Its responsibility is to ensure a secure and reliable linkage between these two crucial components.

The **acoustic radiator** is affixed to the waveguide with the sole purpose of extracting waves from the waveguide and transmitting them into the surrounding water. This component serves as the interface between the ultrasound system and the solution being studied, typically taking the form of a solid cylindrical object.

2.3.3 Acoustic Cavitation Characterization

The study of acoustic cavitation involves investigating its inherent consequences. Sutkar et *al.* [125], in their research, categorize the different types of effects that can be observed with acoustic cavitation. Understanding these effects enables the measurement of cavitation by assessing its resultant impacts. The quantification of primary effects involves measuring parameters such as pressure, temperature, and bubble activity.

In addition to the aforementioned classification, the various methods for detecting cavitation can also be differentiated based on their physical and chemical characteristics. Verhaagen et *al.* [146] categorized cavitation detection into basic tests, acoustic methods, optimal techniques [147, 148], chemical [149–151] and physical approaches [152].

The measurement of cavitation using acoustic methods involves monitoring the sub-harmonic frequency, a technique reliant on observing oscillations at these frequencies, rooted in understanding the dynamic behaviour of gas bubbles within a liquid subjected to the alternating pressure from an acoustic field. The motion exhibited by these bubbles closely resembles oscillations at certain frequencies (f), satisfying the following mathematical relation:

$$x \cdot f = y \cdot f_0 \tag{2.15}$$

where f_0 is the sound field frequency and n, m integers [153].

In the context of ultrasound application, energy transitions from the acoustical mode at frequency f_0 to an acoustical mode at frequency f. When investigating cavitation, the most crucial scenario occurs when m=1 and n=2. This configuration is particularly significant because it enables the straightforward detection and differentiation of the sub-harmonic signal from the fundamental frequency of the sound field, as detailed by Santis et *al.* [153].

Numerous investigations have focused on employing sub-harmonic frequency to study cavitation. The key findings emphasize that the sub-harmonic frequency can serve as an exceptionally sensitive and rapid method for detecting the onset of cavitation. Indeed, piezoelectric detectors only register a significant increase in sub-harmonic oscillation amplitude at the initial stages of acoustic cavitation. This phenomenon can be attributed to the presence of numerous pulsating bubbles within the liquid medium. Additionally, the amplitude of the acoustic field diminishes due to heightened absorption by the cavitation liquid and the subsequent transfer of power to the sub-harmonic mode, as proposed by Edmonds et *al.* [154].

In their research, Puga et *al.* [155] employed an acoustic detection system that marries a

piezoelectric detector with a molybdenum rod submerged within an aluminum-filled chamber. This approach to cavitation detection closely aligns with their intended methodology.

Apart from focusing on sub-harmonic detection, their article also delves into the study of ultra-harmonics to gain a clearer understanding of acoustic cavitation. The stabilization of ultra-harmonics, combined with an elevation in the first sub-harmonic, significantly enhances the precision of cavitation detection.

Similarly, and using a different approach, Brabec et *al.* [130] developed an acoustic measurement system that combines a piezoelectric sensor with an echocontrast agent, specifically a 5% solution of lyophilized egg albumin. This approach enhances the ultrasound field and, consequently, improves cavitation detection.

3. Development of a Sensor for Characterization of Acoustic Activity

This chapter aims to develop a system proficient in characterizing acoustic cavitation, with the ultimate goal of integrating a sensorization system into the existing equipment. Additionally, this chapter provides a comprehensive exposition of the equipment, elucidates the sensor requirements, explores available options, and outlines the methodology for their calibration and testing.

3.1 Equipment Design and Integration

The analysis of the equipment will consider as the ultrasound setup is composed of two primary component groups, each serving distinct functions. One group is dedicated to the generation and propagation of ultrasound, while the other is responsible for containing the wastewater within the chamber and at the same time responsible for the structural stability. The chamber itself possesses a total volume of 20 L, along with an interior diameter measuring 100 mm. Notably, the chamber is equipped with two separate inlets. The larger diameter inlets, regulated by spherical valves, facilitate the intake and outflow of water, boasting an inside diameter of 30 mm. A noteworthy feature of this chamber is its water-cooling capability, a characteristic that sets it apart.

In parallel, the smaller diameter inlets are instrumental in connecting water for cooling purposes, indirectly contributing to the temperature regulation of the liquid within.

Extending from the chamber, a supporting structure provides essential stability to the entirety of the ultrasound equipment. This structural framework is reinforced by a beam that establishes secure connections with the chamber at two key points, ultimately extending to an elevated base.

The base, equipped with four rubber feet, is designed to effectively dampen vibrations. To enhance its mechanical resilience, the lower section of the structure incorporates three sturdy ribs.

For a visual representation of all the exterior components and structural features, refer to Figure 3.1.

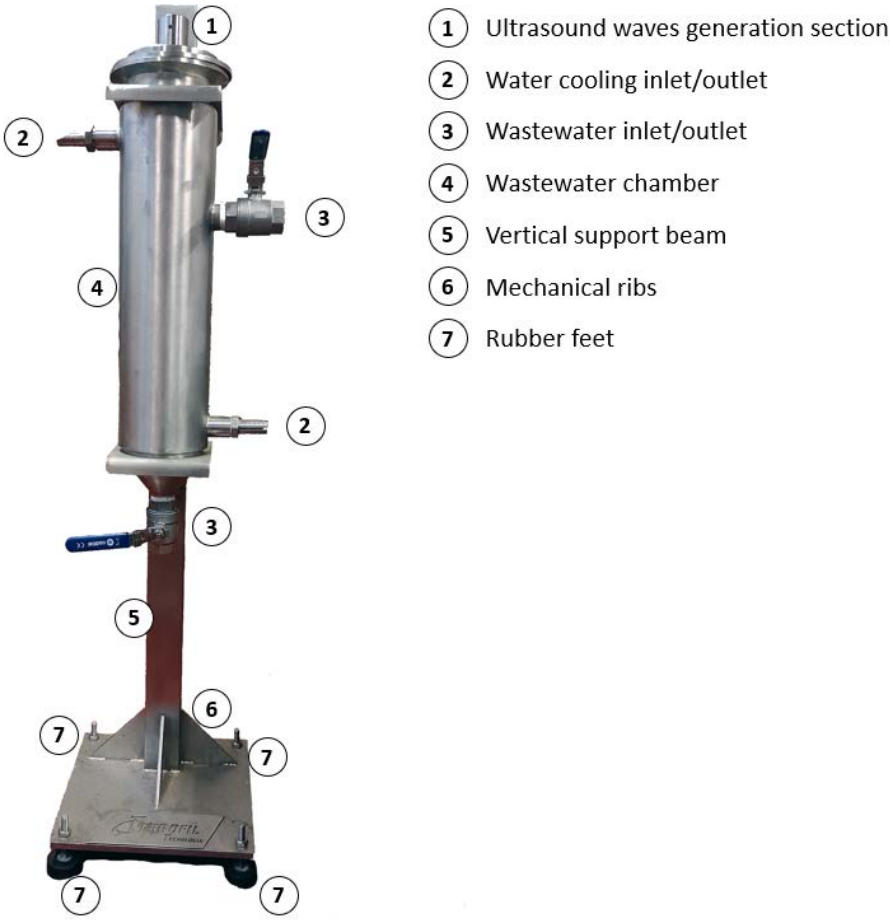

Figure 3.1: Equipment main components with focus on the exterior section and structural parts.

The counterpart of the equipment handles ultrasound generation and propagation, Figure 3.2. The piezoelectric transducer, responsible for generating ultrasound, is a 20 kHz transducer linked to the power generator. The first waveguide, positioned externally to the chamber, boasts a 25 mm diameter and connects the transducer to a 38 mm external diameter booster. A flange situated between the transducer and booster serves as the top chamber seal. Within the chamber, an internal wave guide, with a length of 364 mm and a diameter of 50 mm, facilitates the propagation of ultrasound within the water and until the acoustic radiator. As referenced before, the booster is the structural element that supports the flange and ultrasonic wave guide.

Additionally, the waveguide is equipped with strategically placed holes to accommodate dimensional variations along the vertical axis.

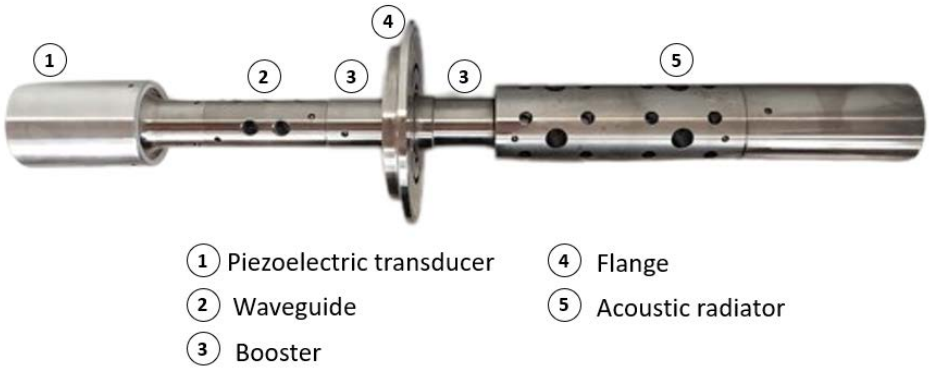

Figure 3.2: Part of the equipment responsible for the generation and propagation of the sound waves and respective parts: Piezoeletric transducer, Waveguide, Flange, Booster and Acoustic Radiator.

The equipment's functioning is detailed on Figure 3.3. The two spherical valves control the inflow and outflow of water. Presently, the setup is configured to allow water to enter through the upper valve and exit from above. However, changing this configuration is a straightforward process; one simply needs to switch from one valve to the other.

In cases where sediment deposition occurs, it is preferable to have an inlet from the bottom and an outlet from above. Given that this is an experimental chamber operating in batch mode, this configuration is essential, as there is no external pressure from above to expel water from the chamber.

There are two other inlets for chamber cooling. These lead to a serpentine arrangement within the chamber, which promotes convective and conductive heat transfer from the chamber to surrounding liquid.

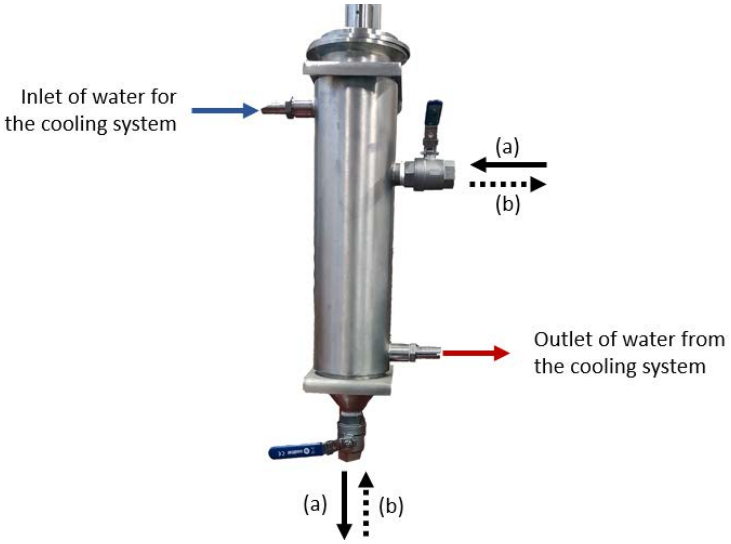

Figure 3.3: System operation with water inlet and outlet for chamber cooling. The treated water outlet can be positioned at the (a) bottom valve if contaminants tend to rise to the surface, or at the (b) top if contaminants tend to settle.

The quest for mechatronic control and sensor integration for reading the acoustic cavitation, required substantial improvements to the original design. These adaptations were imperative to accommodate sensorization effectively. Key among these modifications was the creation of an internal construction enabling the seamless passage of cables and measurement systems from the exterior to the interior.

Acquiring the electrical signal within LabVIEW was a fundamental requirement. Additionally, the diameter of the system was constrained to be below 15 mm to ensure compatibility with the existing setup.

Resistance to ultrasound activity was another crucial criterion, mandating the system to acquire at a minimum frequency of 40 kHz. This stringent requirement was established to enable measurements in environments where ultrasound activity is prevalent.

The system was also expected to feature non-complex acquisition systems, aligning with the overarching objective of achieving an economical solution. This called for the integration of streamlined and cost-effective components.

Additionally, the need for removable and adjustable sensor positioning was crucial for ensuring adaptability and simplified maintenance. This feature enables the reconfiguration and substitution of sensors as necessary, thereby facilitating continuous system optimization.

The detailed requirements for sensor development are outlined in Table 3.1.

Table 3.1: Sensor requirements for the design and development of the acoustic sensor reading.

Sensor Requirements	
Acquire electrical signal in Lab view	Diameter bellow 15 mm
Resistance to ultrasound activity	Acquire at minimum of 40 kHz
Non complex acquire systems	Economic
Removable	Variable sensor position

To meet the specified requirements, two design concepts were developed for integrating sensors into the ultrasonic chamber.

Option A, originating from the upper inlet, necessitates distinct guides and a complex integration system. This solution involves two guide tubes for cables, with the second tube also supporting the sensor. It requires a support with a 90 degree joint to mimic a Morse cone system. However, this approach introduces challenges such as wire passage through multiple holes, potentially increasing signal noise and assembly complexity.

In more practical terms, option A involves the use of two separate guide tubes for cables, Figure 3.4.

The second tube serves a dual purpose by also providing support for the sensor. To achieve this, a support with a 90 degree joint is employed, akin to a Morse cone system. While this solution is viable, it does introduce some challenges. For instance, the process of threading wires through multiple holes may lead to increased signal interference and greater complexity during assembly.

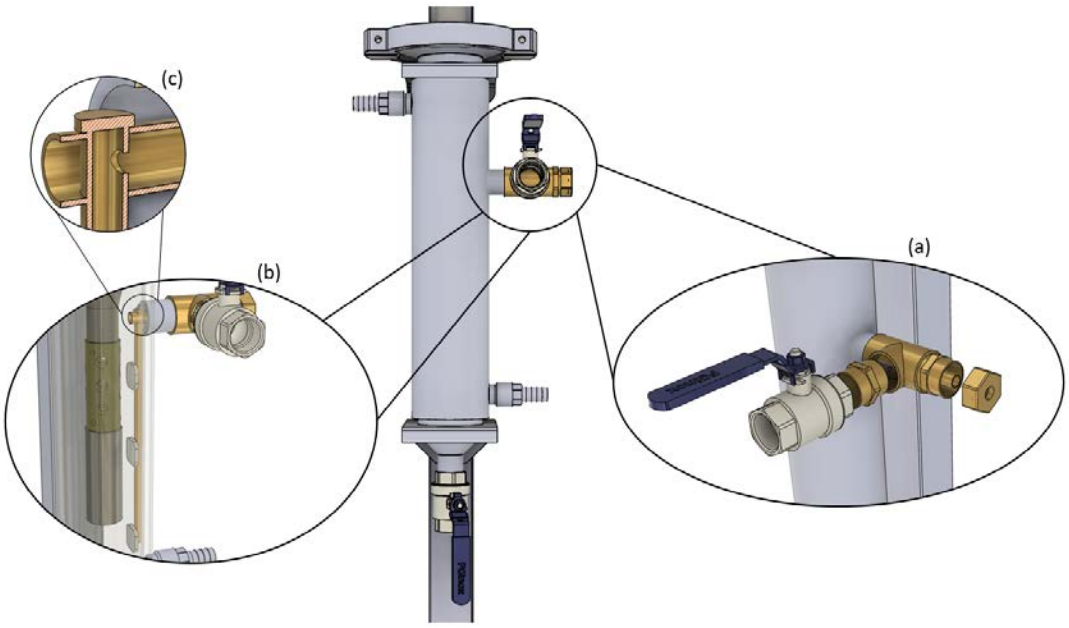

Figure 3.4: Design Concept A employs two tubes for wire passage: (a) with a dual entry at the top for chamber access, and (b) a perpendicular tube for wire passage to the piezoelectric sensors. (c) A detailed view emphasizes the connection between the tubes, highlighting the wire passage hole and the superior plate securing the second tube.

Option B involves a singular tube meticulously shaped to conform to the interior chamber design, as illustrated in Figure 3.5 (a). The tube is seamlessly welded to a flat-faced plug, establishing a connection with the chamber through the use of a T-connector, featuring inlets for water and sensor wires, as depicted in Figure 3.5 (b). The wires traverse the interior of the tube and are precisely bent into the desired position, as shown in Figure 3.5 (c). Once the tube is positioned at the water level within the chamber, there is no need for additional sealing at this juncture. Consequently, this design offers enhanced flexibility for adjusting the sensor height.

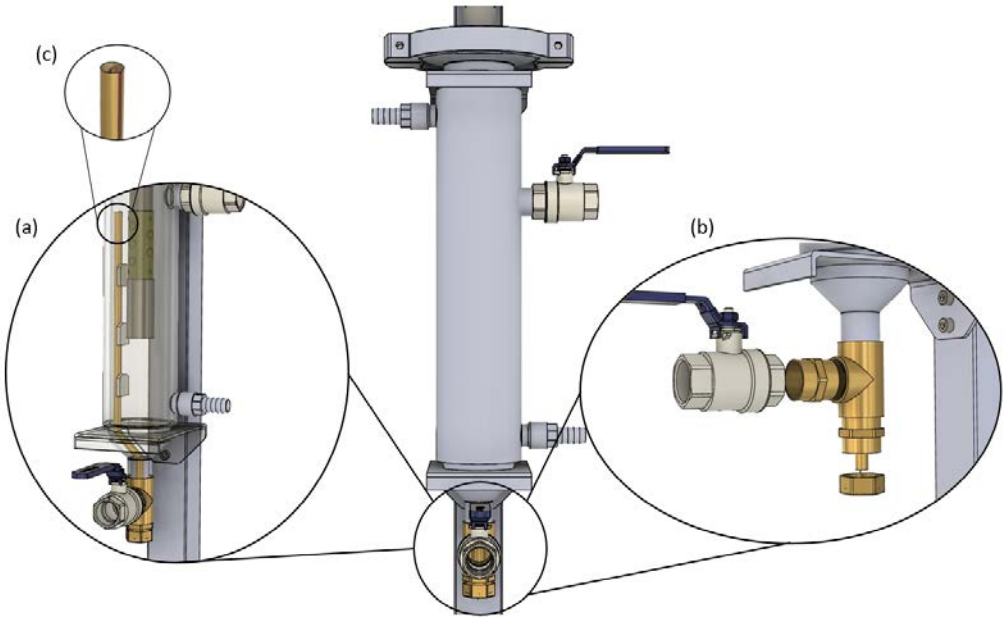

Figure 3.5: Design Concept B employs a single curved tube for wire passage: (a) entering from the bottom of the cylinder in a straightforward operation, (b) utilizing a double inlet accessory connected with a threaded connection, and (c) establishing the wire connection to the piezoelectric sensors via the superior passage on top of the tube.

Upon careful evaluation of both options, a comprehensive analysis reveals that option B stands out as the superior choice. Its advantages are manifold, ranging from simplicity of design to cost-effectiveness and heightened adaptability.

Option B simplifies the construction process by requiring fewer components, contributing to a more efficient and straightforward system. Additionally, it eliminates the necessity for sealing tube holes, marking a noteworthy enhancement in terms of both practicality and maintenance.

One of the most significant merits of option B lies in its flexibility in adjusting sensor height. This attribute empowers the system to achieve acoustic acquisition at any position along the tube, providing a versatility that is crucial for optimizing data collection.

In stark contrast, option A presents certain complexities, particularly in the integration process. The requirement for distinct guides and a complex integration system introduces potential points of failure and complicates the overall assembly.

Furthermore, option A's reliance on multiple tubes introduces a higher probability of signal noise, reduced wire resistance, and increased assembly difficulty, thereby presenting notable drawbacks.

Considering these factors collectively, option B emerges as the preferred selection. Its streamlined design, cost-effectiveness, and heightened adaptability make it the most prudent choice for this application.

With the design option already selected, it is now time to proceed with the implementation. The tube bending process was meticulously carried out using a manual bending machine, with additional heat assistance. The dimensions were finely tuned to ensure a precise fit within the chamber. At the bottom, a T-connection was introduced, featuring dual outputs for both water input and wire passage, firmly secured through tin welding.

The internal diameter of the tube is 10 mm, designed to accommodate a minimum of three sensors. The wire diameter allows for a 3 mm gap when three sensors are in use. The tube's length is designed to prevent contact with water, eliminating the need for additional sealing, Figure 3.6 (a).

The completed bent tube is showcased in Figure 3.6 (b). Rigorous testing was conducted to identify any potential leaks, and the results confirmed the integrity of the tube.

The tube conformation process involved a manual bending machine in the Engine Laboratory of the Mechanical Engineering Department at the University of Minho. The initial attempts led to some marks on the part, but no leaks were discovered during testing with water and compressed air.

The tube, T-joint, plug, and thread adapter form an integrated assembly. The plug was drilled to accommodate the tube, and the thread adapter allows for secure attachment. The tube is attached to the plug through embedding and subsequent welding.

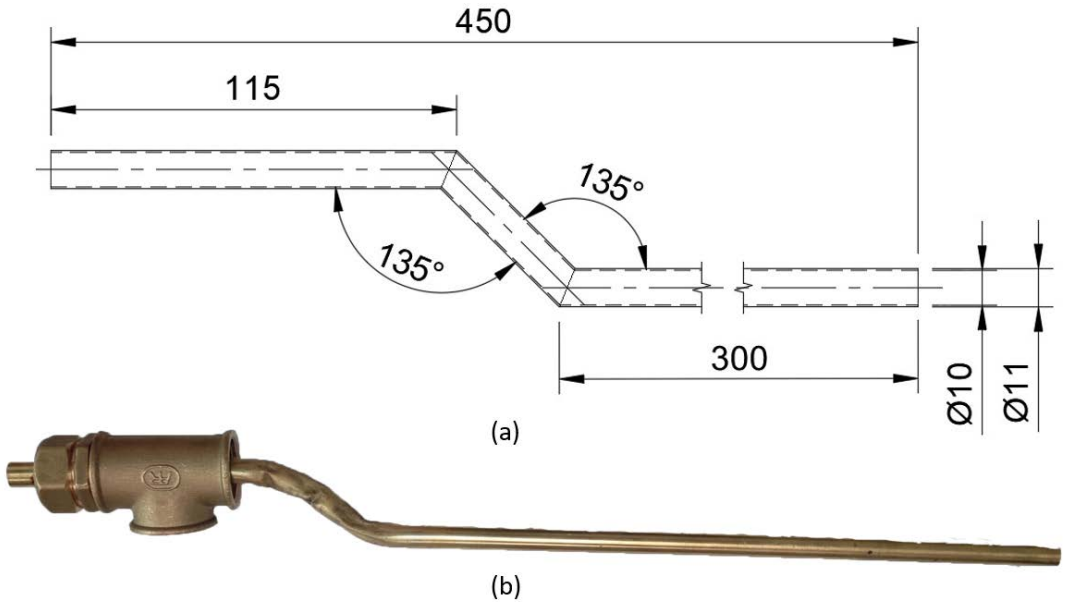

Figure 3.6: Structural component to guide and attach all the wires from the sensor (a) Specifications for tube dimensions and a technical drawing for manufacturing (b) Wended tube support for the wire passage to the piezoelectric sensors after manufacturing.

3.2 Piezoelectric Sensor Setup and Data Analysis

In this application, three piezo HS-PC40 from Hangzhou Altrasonic Technology Co. Ltd. elements were employed. Each piezo disk featured a diameter of 50 mm and a thickness of 2 mm. According to the data sheet provided by the manufacturer, see Annex I, the piezo disk exhibit a resonance impedance of 10 Ω at 1kHz, a direct capacitance of 11 nF, and an electromechanical coupling coefficient of a minimum of 40%. The latter, measured with a LCR meter, was not specified by the manufacturer. This parameter denotes the efficiency of energy conversion within piezoelectric materials, encompassing the conversion of mechanical into electrical energy as well as vice versa [156].

To ensure compatibility with the chamber and to minimize signal interference during data capture, the piezo disks were precisely cut into a square shape. This adaptation allowed the piezo to be treated as having a square shape for analytical purposes. As a result, the electrical charges from the two possible stress directions can be estimated using the following equations:

$$V_{31} = \frac{g_{33} \cdot F_1}{4 \cdot L} \tag{3.1}$$

Here, g_{33} represents the electric field generated by applied stress in direction 1, F_1 denotes the applied force in direction 1, and L signifies the square length.

$$V_{33} = \frac{g_{33} \cdot F_3 \cdot t}{L^2} \tag{3.2}$$

In this equation, g_{33} represents the electric field generated by applied stress in direction 3, F_3 is the applied force in direction 3, L is the square length, and t is the ceramic thickness.

The piezo sensors, belonging to the category of active materials, are distinguished by their ability to establish a strong correlation between mechanical and electrical quantities. These materials exhibit a notable mutual coupling, enabling them to efficiently convert mechanical stimuli into electrical signals and vice versa. Passive materials, on the other hand, constitute the remaining components of the devices [156]. In Figure 3.7, the axes considered for the previous equation are illustrated.

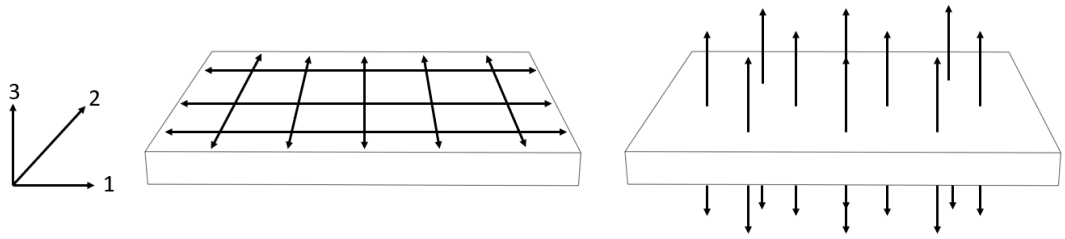

Figure 3.7: Piezoelectric sensor configuration after polarization. Image adapted from Puga et *al.* [156].

The ceramic piezoelectric elements, initially 50 mm of diameter, were cut into a 25 mm square. This process wa challenging due to the material's sensitivity to temperature changes and its inherent brittleness. The presence of microstructural defects within the material further heightened the need for caution during the cutting process. To mitigate the risk of fracturing, a cautious approach was adopted. The cutting was carried out with slow, deliberate movements to minimize stress concentration along the cutting path. Additionally, a cooling fluid was employed to reduce both the thermal gradient within the material and the overall temperature. This cooling process aimed to preserve the material's polar field, which is crucial for its piezoelectric properties.

The piezoelectric sensors, are composed of ceramic elements coated with a layer of silver. On the front part, Sensor 1 is coated with the same resin, Figure 3.8 (a), while the others are left in their original form. To protect the wires and ensure secure electrical connections, an epoxy layer was applied to the rear side of the sensors Figure 3.8 (b). This sensitive protective layer is crucial for enhancing electrical conductivity and providing thermal protection. It prevents direct contact between water and wires while also safeguarding the silver coating from ultrasound exposure.

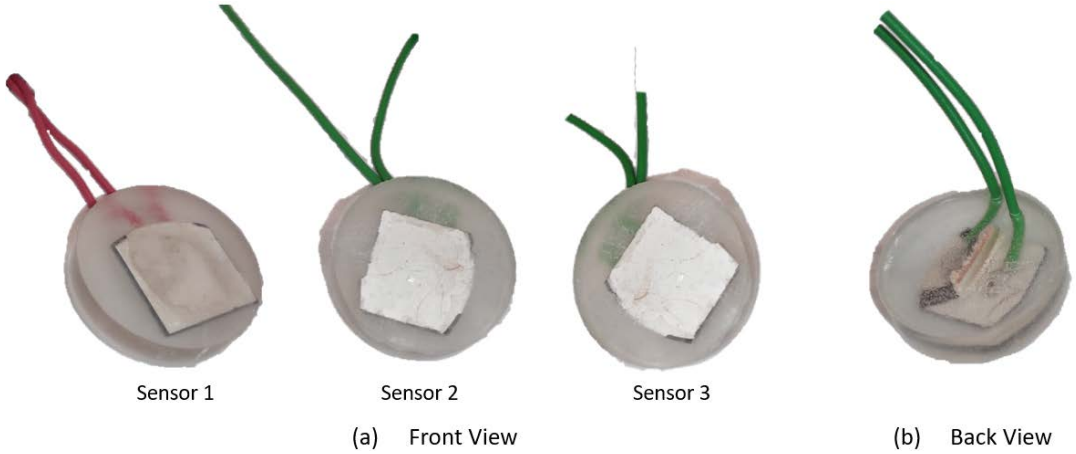

Figure 3.8: Piezoelectric sensors for the acoustic reading with a (a) front view of sensors 1, 2 and 3 and (b) the back view of the three once they have all the same construction.

Having safeguarded the piezoelectric elements, the subsequent step involves processing the acquired data. To achieve this, a program was developed in LabVIEW, encompassing three key sections: the main menu, the Help menu, and the data acquisition menu.

The main menu offers users three distinct options: initiating the Data Acquisition process, accessing the Help menu for guidance, or simply closing the program. This intuitive interface ensures easy navigation and selection of desired actions.

Figure 3.9: Main Menu for the LabVIEW program with the Start, Help and Exit bottoms.

The LabVIEW program for the Main Menu is depicted in Figure 3.10. The structural arrangement for the "Help" and "Start" buttons is outlined. The entire sequence is encapsulated within a "Flat Sequence" box, comprised of two distinct segments. The initial segment features a while loop cycle with an event structure, while the second segment contains the command to terminate the program.

Focusing on the event structure, as depicted in Figure 3.10 (a), the code for activating the "Start" and "Help" menus is discernible. Pressing the "Mais" button navigates to the "Help" menu, whereas pressing "Grave" directs the program to the recording menu. If the "Exit" button (named as "Ok") is pressed, the event structure transitions to a new state, terminating the while loop and facilitating the shift from the first state in the sequence to the second, ultimately shutting down the program (Figure 3.10 b).

Selecting the Help menu provides access to a comprehensive guide, offering explanations of the entire program and useful tips for organizing data effectively. The instructions provided in this menu are tailored to simplify and optimize subsequent data processing in Python.

To facilitate seamless data treatment in Python, it is advisable to follow the naming and saving conventions outlined in the Help menu. This systematic approach ensures that the data integrates smoothly with the Python program.

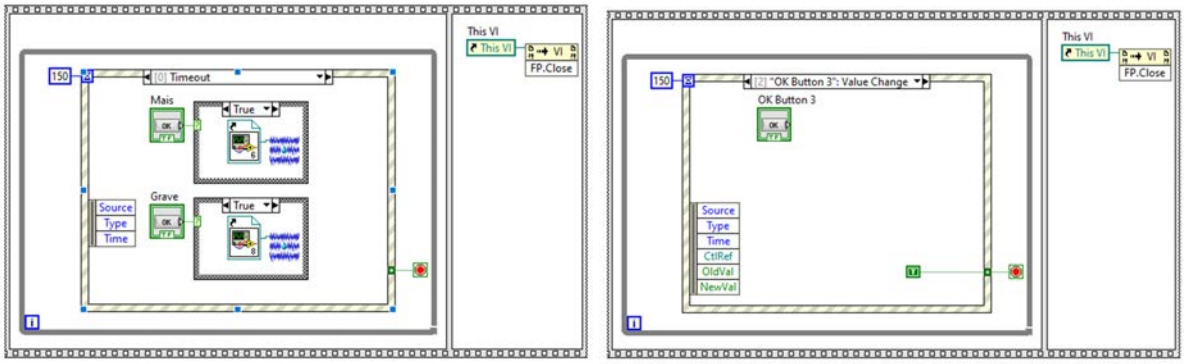

(a) (b)

Figure 3.10: LabVIEW code for the Main Menu with (a) sequence for the access to the Menu Start or Help and (b) for close the program.

Additionally, a convenient feature is located in the lower right corner. When activated, this button allows the user to download the Python program required for data treatment and generating FFT (Fast Fourier Transform) graphics. This further streamlines the data analysis process and enhances the overall user experience.

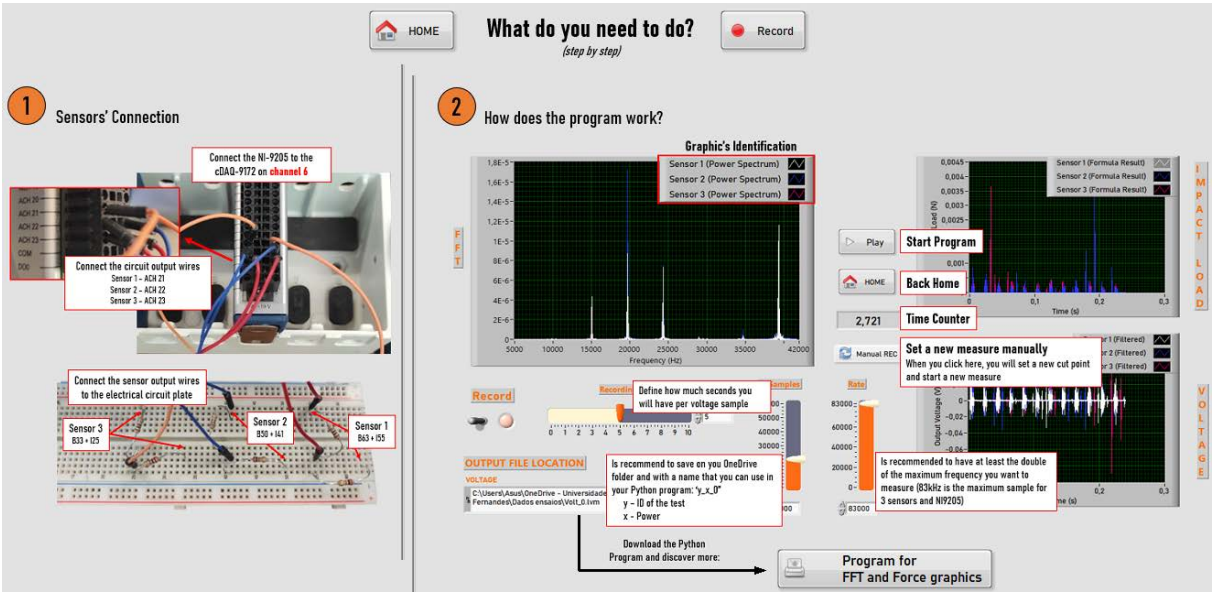

Figure 3.11: Help Menu with all the explanations for utilization of the program and all the options possible.

In Figure 3.12, the code for the Help Menu is presented. Much like the "Main Menu," this code incorporates options to navigate to other menus. Specifically, pressing the button labeled "Cancel" directs the user back to the "Main" menu, while selecting the button labeled "Record" leads to the "Start" menu. To facilitate access to the external domain for downloading the Python code responsible for FFT and Force graphics generation, a button is provided to guide the user through the file download process.

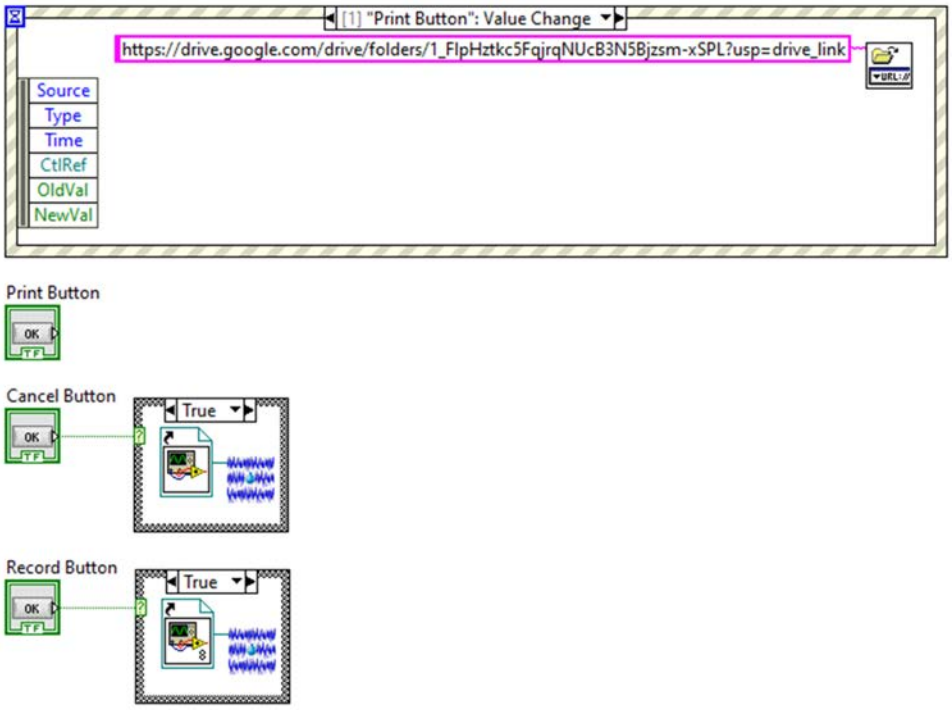

Figure 3.12: LabVIEW Code for the Help Menu With Sequences for the Buttons.

Regarding to the menu for data acquisition, it is necessary to consider that data acquisition process consists of two main components: real-time data visualization and user inputs. The graphics display instantaneous voltage, corresponding Fast Fourier Transform (FFT), and calculate and display instantaneous force on the sensors. This allows users to monitor and analyse measurements effectively.

The user interface for inputs allows modification of certain parameters and the decision on when to save the data. To initiate data acquisition, users need to press the "Play" button, after configuring the acquisition parameters. For optimal results with three sensors and to achieve the maximum frequency range, it is recommended to set the parameters to 83 kHz and 20 k samples per second.

The record function is activated only when the user presses the "Record" button, enabling them to specify the duration of the recording sample. This feature ensures precise and controlled data collection, providing flexibility to capture data for specific periods as needed.

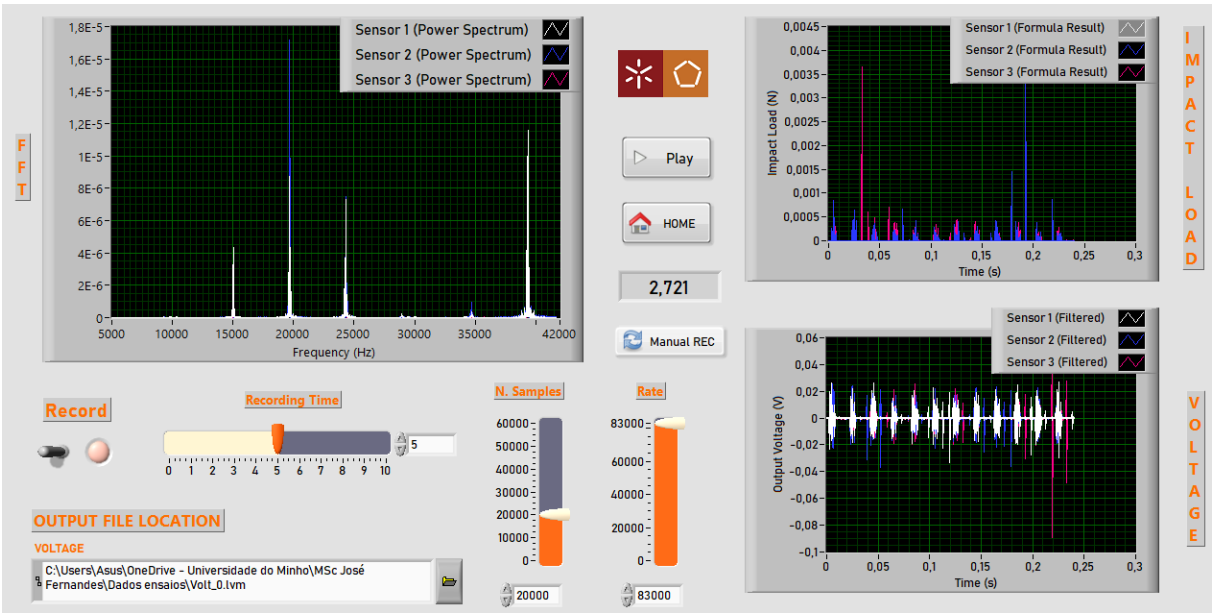

Figure 3.13: Data Acquisition Menu with the FFT graphic, Impact Load and Voltage acquisition. It is possible to set the recording time, the output file location, number of samples and rate and start and stop the record.

In Figure 3.14, the Acquiring and Recording Menu operates by initiating data acquisition only when the "Play" button is pressed. Upon meeting this condition, a countdown timer is activated. The duration of the recording, denoted as "slide 2," is defined by the user within the "User Interface." Users can specify the number of samples and the rate for data acquisition through the "Number" and "Rate" settings, respectively. LabVIEW's assistant is utilized for data acquisition, and the acquired signal undergoes noise reduction processing.

To limit data acquisition above 9,000 Hz, a "low-pass filter" is employed. This filter ensures that only frequencies below the specified threshold are considered in the acquisition process.

The acquired data is presented through corresponding graphics. Prior to these graphics, a spectral measurement is conducted to generate the FFT graphic. Additionally, an equation is applied to transform the signal acquisition into Force readings.

For recording and exporting data, users can define the initial moment as mentioned earlier. Upon pressing the "Gravar" button, the data is recorded and exported to a ".txt" file, following the predefined time cycles. This functionality allows users to capture and export the acquired data for further analysis and use.

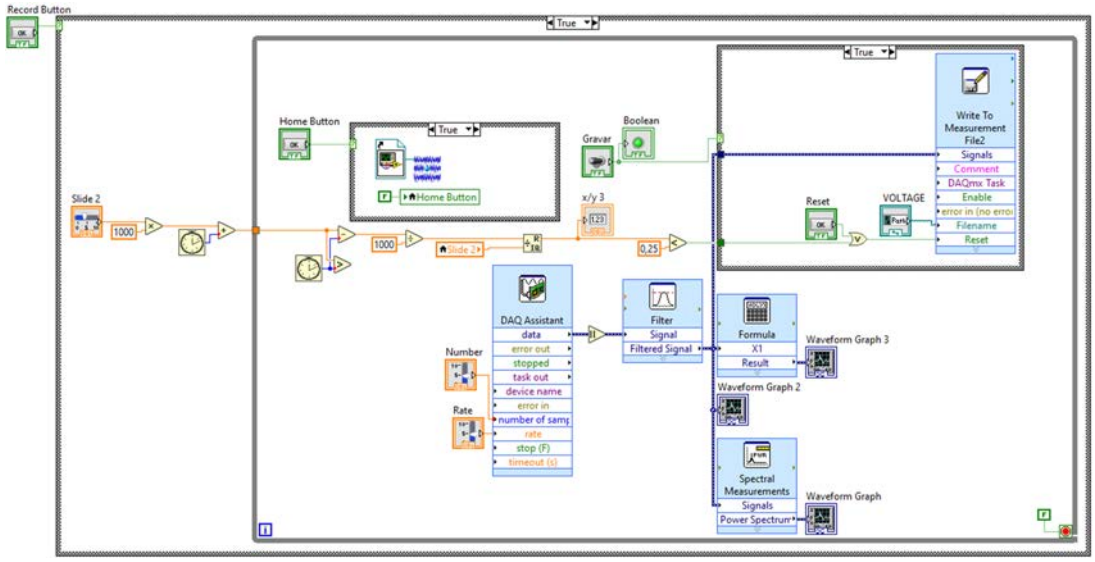

Figure 3.14: LabVIEW Code for Data Acquisition in the Recording and Acquisition Menu.

In the data analysis process, Python is employed to generate FFT graphs. The primary goal of this program is to effectively eliminate noise and create text files containing frequencies of interest (10,000 Hz, 20,000 Hz, 30,000 Hz, and 40,000 Hz) along with their respective amplitudes in the FFT.

An important consideration during analysis is accounting for slight deviations in the output frequency of the ultrasound. Therefore, a tolerance range of 1 kHz around the 20 kHz value is applied to ensure accurate results. As mentioned previously, saving the file with a standardized name is crucial to facilitate and optimize the Python program execution.

User input is minimal, as they only need to specify the first and last numbers of the acquisition sample sequence and provide a name for the output file. The program will then read each file, generate an individual FFT graph, and export the data as a single text file containing the maximum value for each frequency of interest.

3.3 Experimental Conditions

To **characterize the acoustic cavitation**, the test protocol involve subjecting the sensors to varying ultrasound conditions in two distinct chamber positions. To accommodate the unique behaviour of ultrasound, particularly as power output increases, factors such as the influence of the horn and water temperature come into play. The test methodology was deliberately designed to alternate between the two extremes of power levels. This alternation between maximum and minimum power levels was carried out methodically, with each power level maintained for a fixed duration of 18 seconds. During

this interval, voltage samples were meticulously collected at regular 3-second intervals, resulting in the acquisition of six voltage data points for each power level.

The decision to include a substantial number of sampling points in the experimental design was a deliberate one, made with the goal of enhancing the quality and reproductive of the data. It was recognized that our initial data collection efforts, which utilized fewer samples, had certain limitations. By significantly increasing the number of samples taken, we ensured that the voltage data points closely mirrored the actual conditions within the chamber. Consequently, this bolstered the reliability and robustness of the obtained results.

It is also noteworthy that the power levels employed in the testing were controlled, with tolerances of 10W. These power levels were set at specific values: 70 W, 140 W, 280 W, 350 W, 420 W, 500 W, 600 W, 700 W. Furthermore, Sensors 1, 2, and 3 were positioned uniformly at the same height within the chamber but strategically distributed to ensure comprehensive coverage. Position 1 was situated at 50 mm from the water level, while Position 2 was located at 250 mm from the top, Figure 3.15.

The data collection process was executed using the refereed program tailored for this specific purpose. Subsequently, the collected data underwent treatment utilizing a Python program, to ensure consistency and accuracy in the analysis. This methodology was essential for yielding meaningful insights into sensor responses and their capacity to detect acoustic cavitation.

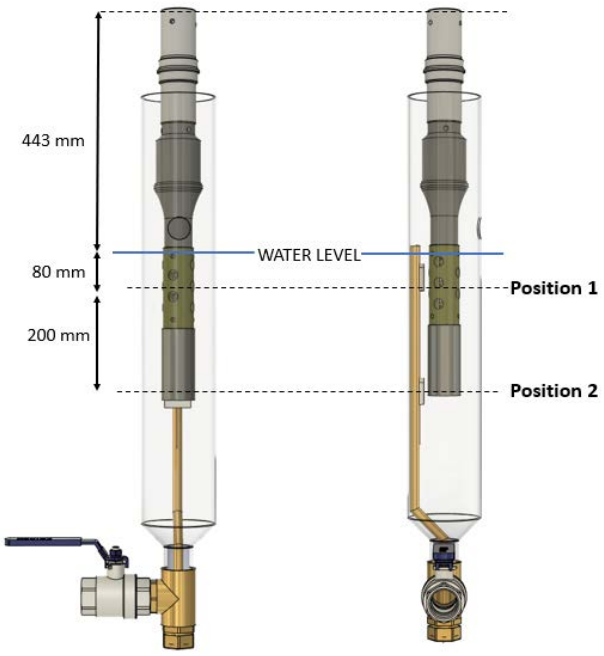

Figure 3.15: Test Positions 1 and 2. Position 1 is located at a distance of 50 mm from the water level, while Position 2 is positioned 250 mm above it. The acoustic sensors are fixed to the interior structure.

The piezoelectric sensors were individually calibrated due to variations resulting from the cutting operations and epoxy application. It is intended to establish a calibration curve between the impact load and the voltage. The calibration setup was identical for all three sensors, and the experimental conditions were consistent and based on the study of Hujer et *al.* [157]. The setup, as shown in Figure 3.16, comprised a ruler, an acrylic guide, a slow-motion camera, a DAQ acquisition system connected to a computer, and four different spheres. The DAQ acquisition employed was the NI 9205 from Texas Instruments connected to the NI cDaq-9172 instrument.

Different spheres were used with varying dimensions and materials to achieve distinct impact loads and characteristics. The spheres included an Alumina sphere with 2.02 g and mm diameter, two spheres of Aluminium with 0.04 g and 0.40 g, and one sphere of stainless steel with 0.80 g. These spheres were dropped from six different heights, 50 mm, 100 mm, 170 mm, 270 mm, 370 mm, and 470 mm through a guide tube, with a stabilized pincer. This allowed to establish a relation between the range of impact loads and ensured that the maximum impact load in the calibration remained less than the maximum impact load from the cavitation. For the reading of the rebound it was used a camera with low speed recording.

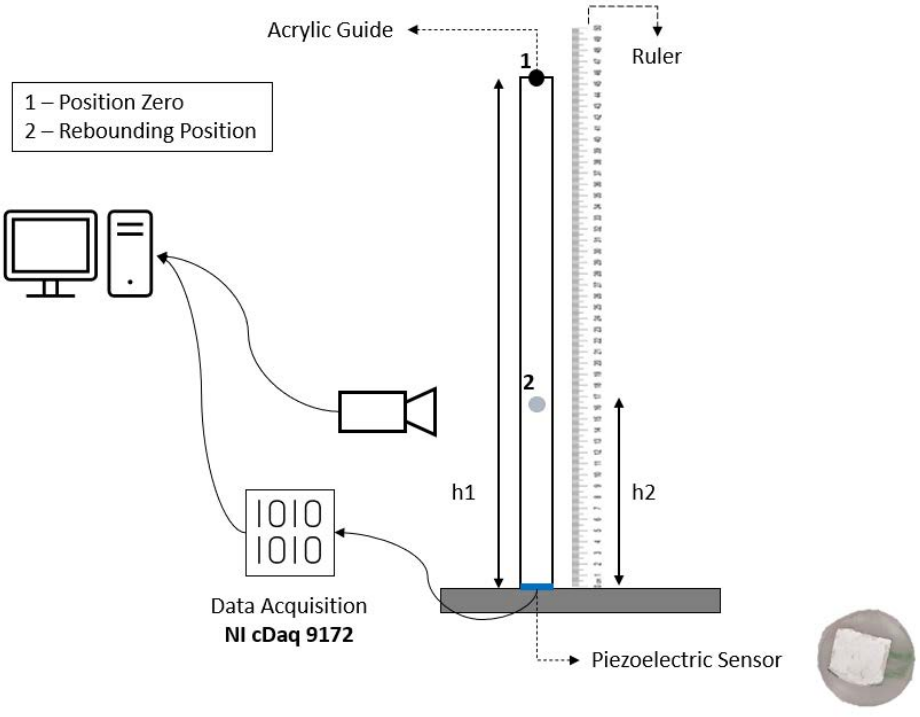

Figure 3.16: Experimental Setup for Impact Test. The positions 'zero' and 'rebounding' are characterized by their respective heights and velocities. Data acquisition from the presented piezoelectric element is facilitated by the NI cDAQ 9172 system connected to the computer. The rebounding height is captured using a slow-motion camera.

The principle behind the test is that the impact of the spheres with the piezoelectric element will generate a tension that can be measured and recorded. The interesting variables for force calculation are shown in Equations 3.3 and 3.4.

$$F_(avg) = \frac{1}{\tau} \cdot \int_{t_1}^{t_2} F(t)dt \tag{3.3}$$

$$F_(avg) = \frac{m}{\tau} \cdot (v_1 + v_2) \tag{3.4}$$

where m is the mass of th ball, v_1 is the initial velocity (at point 1), v_2 the velocity on the point 2, and τ is the impact time of the sphere. This last parameter it is analysed on the recorded voltage acquisition and corresponds to the piezoelectric voltage peak duration [157, 158].

Velocities from the point 1 to 2 can also be calculated with the following equation,

$$v_{1,2} = \sqrt{2 \cdot g \cdot h_1, 2} \tag{3.5}$$

where $h_1, 2$ it is the height of the ball from the sensor and g is the gravitational acceleration [157, 158].

The maximum force can be considered as the double of the average force,

$$F_{max} = 2 \cdot F_{avg} \tag{3.6}$$

Regarding to data acquisition, the 16 bit analogue module had 32 channels with a minimum and maximum voltage acquisition of 96 μV and 10 V, respectively. The maximum conversion time was 4 $\mu \cdot s$, resulting in a maximum sample acquisition rate of 250k samples per second. Considering three sensors, the sample acquisition rate was divided among all channels. To capture the frequency range from 10 kHz to 40 kHz, a minimum sampling rate of 80 kHz (twice the highest frequency) was set, resulting in a rate of 83 kHz and a data collection interval of 12 $\mu \cdot s$.This parameters will be used in along the remaining tests. In Table 3.2, are evident the parameter that were used along the laboratory tests.

Noise related to wire connections and surrounding sound waves influenced voltage acquisition. To determine the minimal value for non-noise readings, various sensors were tested without any applied force, and the average noise was found to range between 0 mV and 10 mV.

Table 3.2: Data Acquisition Parameters for the NI cDAQ 9172.

Desired Frequency Range	9 kHz - 40 kHz
Sample Rate	83 kHz
Acquisition Interval	12 ms
Voltage Range	0.1 V - 10 V

However, the piezoelectric electrical response need the use of a tension divider. The output voltage from the piezoelectric sensor exceeded 10 V, surpassing the limit of the NI cDAQ 9172. To mitigate this, a voltage divider was implemented, Figure 3.17. This involved using a 200 Ohm resistance in conjunction with a 10 Ohm resistance, resulting in a voltage drop of,

$$V_{output} = V_{input} \cdot \frac{R_2}{R_1 - R_2} \tag{3.7}$$

$$V_{output} = V_{input} \cdot \frac{10}{200 - 10} \tag{3.8}$$

where V_{output} it is the voltage output after the tension divisor, V_{input} the initial voltage and R_2 and R_1 the resistances.

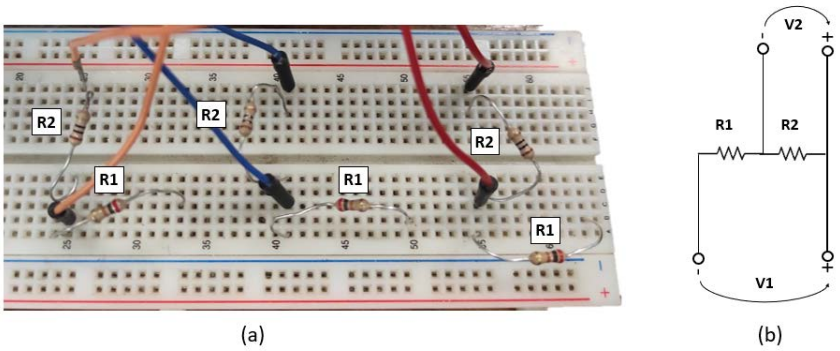

Figure 3.17: Tension Divider for Tension Reduction: (a) Breadboard utilized for electrical connections. (b) Electrical circuit for the tension divider.

4. Experimental Evaluation

This chapter provides experimental evaluation results divided into two main sections. The first focuses on the physical effects of cavitation, particularly the characterization using the developed piezoelectric sensors. The second delves into the influence of ultrasound on water and adsorption systems. The chapter concludes by offering a series of insights derived from the experimental evaluation.

4.1 Physical Analysis of Ultrasound Action on Water

4.1.1 Piezoelectric Calibration and Protective Layer Impact

During the calibration tests, it became evident that the three sensors, see Figure 3.8 exhibited different behaviors. Interestingly, when a protective layer was applied, it was observed that the sensitivity of the piezoelectric sensor decreased. The reduction in sensitivity was so significant that the piezoelectric sensor failed to produce any voltage emission when a ball fell onto it. Subsequent testing with the maximum impact load revealed that the voltage remained unchanged, and there were no discernible peaks on the voltage acquisition graph, Figure 4.1.

This observation strongly suggests that the 0.2 mm Epoxy film used as a protective layer significantly restricts the sensor's sensitivity. Therefore, the protective layer negatively affects the sensor's ability to detect and respond to external forces. As seen in Figure 4.1, the voltage detection is less than the value considered as noise. In that way, it was impossible to establish a calibration curve.

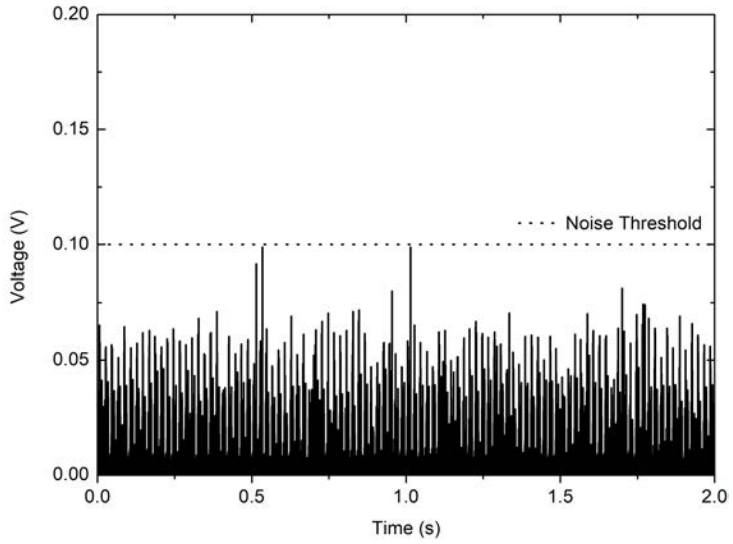

Figure 4.1: Voltage Measurement for Sensor 1 and its Respective Noise Threshold during the calibration process.

The calibration curve of the Sensor 2 shows a linear behavior of the sensor that can be described as a linear relationship between the maximum impact load and the maximum voltage [157].

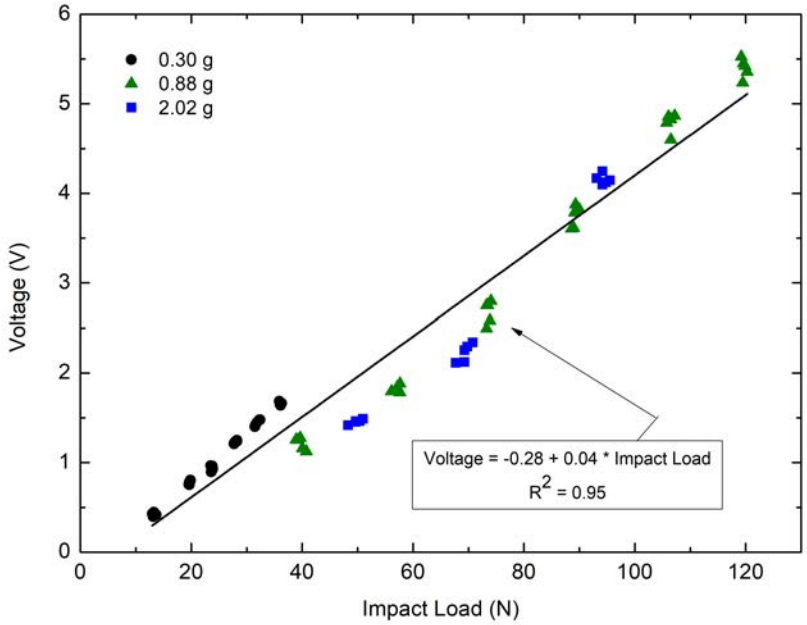

Figure 4.2: Calibration Curve for Sensor 2 with Voltage Variation in Response to Impact Load.

As the weight is change, the maximum voltage of the sensor varies a little. For 0.30 grams there is a more linear growing tendency that for the other heights. This can be interconnected to the impact time. Due to DAQ Acquisition limitation, the minimum time between samples were 12 μs, which corresponds to 83 kHz. Wang et *al.* [159] shows that in similar conditions the impact time of the ball varies in less than 12 μs. This suggests that the current sensors have limitations in data acquisition resolution. The time impact does not vary so much across the time. For impacts of the heights of 0.30 grams and 0.88 grams, the impact time was the same, 36 μs. In the 2.02 grams ball case, the maximum impact time was 60 μs and remains the same for all the cases. These results indicates that the tendency suggested by the bibliography remains once that increasing the ball's weight, the impact load increases as well. More extended results could be seen on Appendix B and Appendix C.

This case is seen as for sensor 2, as for sensor 3 (see the sensors on Figure 3.8). Sensor 2 and 3 have some points that are dislocated from the linear tendency which can be directly connected to the fact that impact time resolution and to experimental variations, mainly on the sensor's impact site. In the same way as sensor 2, the sensor 3 follows a linear tendency, creating a relation between the impact load and the maximum voltage.

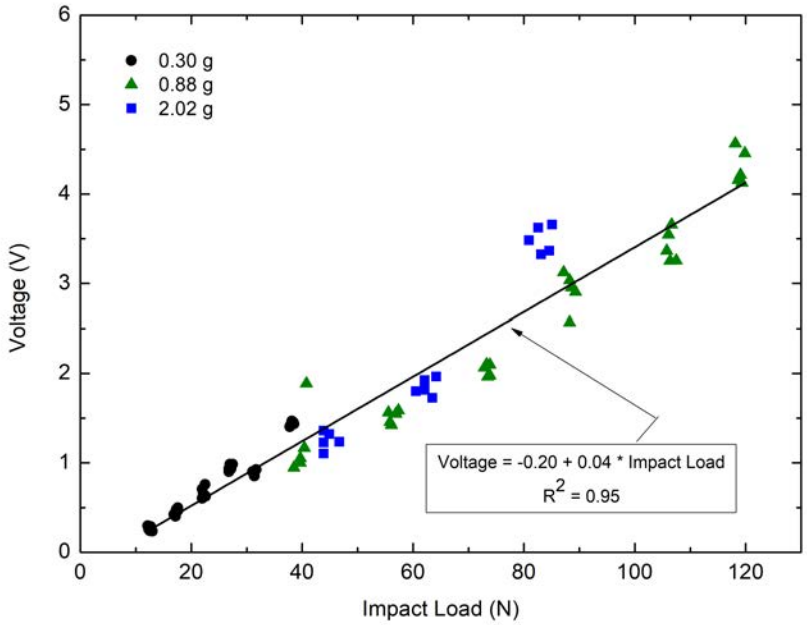

Figure 4.3: Calibration Curve for Sensor 3 with Voltage Variation in Response to Impact Load.

Comparing both sensors, it is evident that they exhibit distinct slopes and theoretical sensitivities. The sensitivity constant, derived from the rate of change of Voltage in relation to applied Force on the squared line, indicates that sensor 2 has a sensitivity of 0.04 V/N, whereas sensor 3 boasts an equal sensitivity of 0.04 V/N. Unfortunately, the manufacture did not provide informations to compare.

Regarding the response to the impact, as depicted in Figure 4.4, it is evident that sensor 2 produces a higher voltage under the same impact load. While this discrepancy becomes notable only for a 0.88 grams sphere after 275 N, it raises the possibility of differing piezoelectric properties between the sensors. The manufacturing process, specifically the cutting procedure, may influence their piezoelectric characteristics. Another conceivable explanation could be associated with potential experimental errors. Despite utilizing 5 data points to establish the calibration curve, variations in the point of impact between the sphere and the piezoelectric material might occur. Additionally, during rebound, the sphere could come into contact with a lateral surface, leading to energy dissipation. Nonetheless, it is apparent that both sensors exhibit a consistent growth pattern for both variables. Any disparities observed are likely attributable to experimental inaccuracies and energy losses.

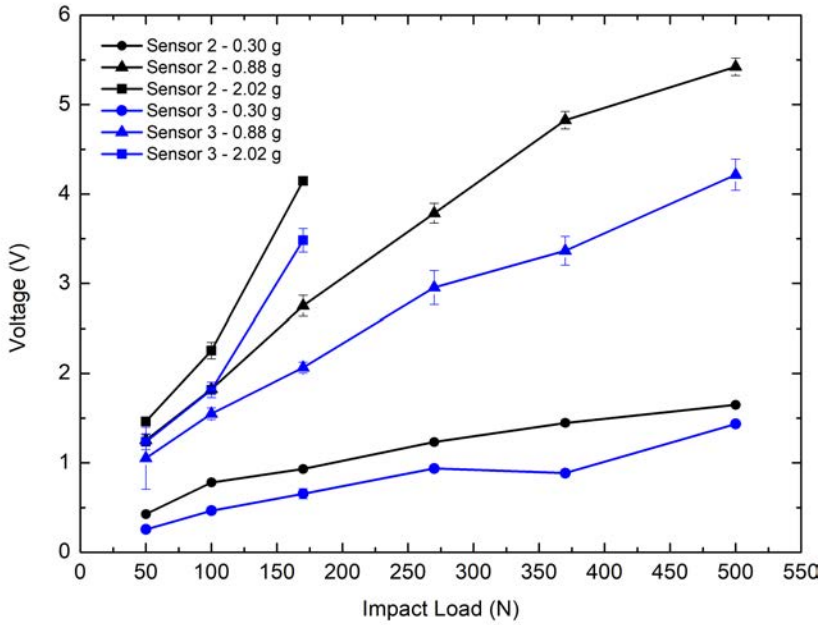

Figure 4.4: Voltage as a Function of Impact Load: Sensor 2 exhibits a higher voltage reading for each impact load. However, both sensors display similar temporal behavior, differing primarily in sensitivity.

The resistance and reliability of the sensors were evaluated through various tests in the chamber. The initial test was conducted without data acquisition to assess the effects of ultrasound on the silver layer of the ceramic and the ceramic itself. Ultrasound power was varied from 100 W to 800 W, in 100 W increments, and each power level was applied for 10 s, totaling 90 s. The sensors were located on the same position on the chamber, Figure 4.5 (b), but scattered around the chamber.

In Figure 4.5 (a), the degradation of the ceramic silver layer is visible at the end of the test for sensors 2 and 3. Notably, the degradation was not uniform between the two sensors, as sensor 3 exhibited less deterioration compared to sensor 2. Sensor 2 also showed signs of breakage, with a noticeable fracture running through the entire ceramic layer. However, it should be mentioned that despite this fracture, the piezoelectric was still able to produce Voltage reading. The epoxy protection constrained the movements of the ceramic, thereby preserving its piezoelectric functionality.

On the other hand, sensor 1, with the epoxy layer, remained unaffected as the epoxy provided protection to the silver layer. Nevertheless, Figure 4.5 illustrates that the sensor was not entirely covered by the epoxy layer due to the polishing process, causing some millimeter defects in the layer. These uncovered areas were vulnerable to wear and tear caused by the action of ultrasound.

The tests revealed that the sensors without any protective layer are more subjects to degradation by effect of ultrasound. However, without any more specific tests it is impossible to announce if the sensor is compromised or not. More tests were done in order to ensure if the sensor is operation or not.

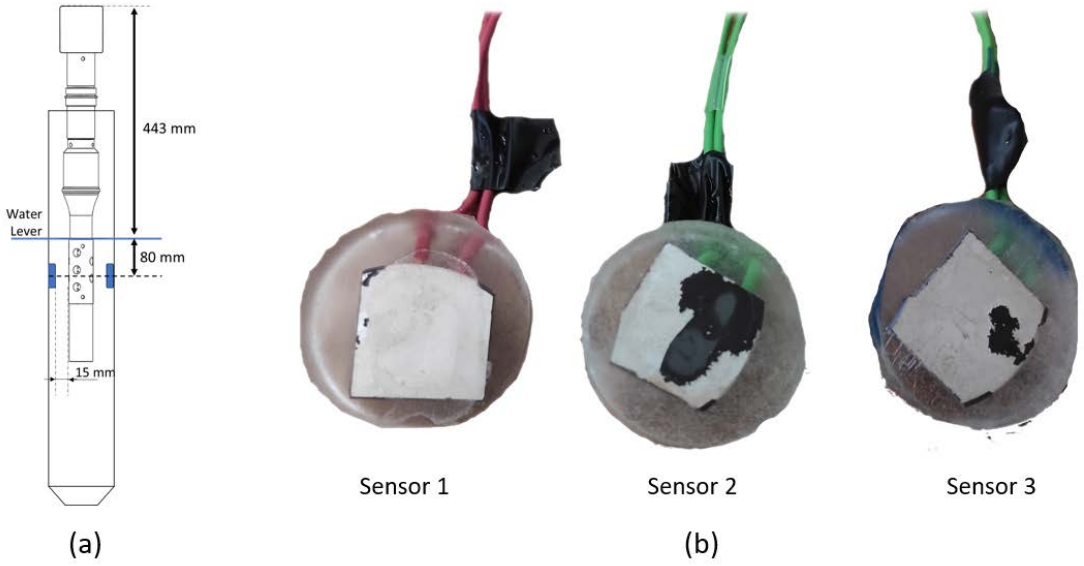

Figure 4.5: Piezoelectric sensors after 90 seconds of cavitation at varying ultrasound frequencies - from 100 W to 900 W, with 10-second intervals. (a) The three sensors were at the same level on the chamber, with 80 mm difference from the water level. (b) Sensor 1 exhibited damages only on areas with deficient epoxy cover. Sensors 2 and 3 displayed damages on the surface layer.

4.1.2 Cavitation Monitorization with Piezoelectric Sensors

The investigation of the sub-harmonic (f/2) has proven to be a reliable parameter in understanding the development of acoustic cavitation within a liquid solution [155]. Figure 4.10 displays the variation of the sub-harmonic for the three sensors at different frequencies, for the Position 1, see Figure 3.15 for positions. This study aims to discern the magnitude of the sub-harmonic as the frequency increases, shedding light on the cavitation development.

In correlation with the studies of Eskin et *al.* [160] and Abramov et *al.* [161] three distinct zones have been proposed. The first zone is referred to as the incipient cavitation, followed by the cavitation threshold in the second zone, and the well-developed cavitation regime in the third. The transition between these zones is believed to occur due to a significant increase in the acoustic signal of the sub-harmonic, signifying the cavitation threshold has been reached, as suggested by Eskin et *al.* [160] and Puga et *al.* [155].

To construct the current graph, was calculated the magnitude of the acoustic signal at the sub-harmonic point. Each data point on the graph represents an average derived from five measurements, with the mean deviation indicated in each corresponding plot.

When examining the piezoelectric sensor responses within the cavitation field at "Position 1", distinctive patterns emerge for each sensor, Figure 4.6. Sensor 3, located in this position, generally

exhibits a magnitude similar to Sensor 1, with the exception of a noticeable drop at 340±10 W. Given that this deviation is isolated, it is categorized as an anomaly and deemed a data error.

In contrast, Sensor 2 consistently displays irregular data points, indicating a potential issue with its functionality. This inconsistency raises concerns about its reliability in providing accurate measurements.

Notably, a sharp increase in the acoustic signal is observed within the power range of 500±10 W to 600±10 W for Sensor 3. Sensor 1 demonstrates a gradual and smooth increase, while Sensor 3 experiences a significantly sharper and higher rise across the entire spectrum. The discrepancy in the sharpness of the increase between Sensor 1 and Sensor 3 may stem from differences in sensitivity or from variations in cavitation distribution within the chamber. Even when positioned at the same height, the propagation of acoustic waves is not uniform in all directions at a given point along the y-axis.

Taking all of this into consideration, and based on the information provided, this range is established as the new threshold point for this specific position.

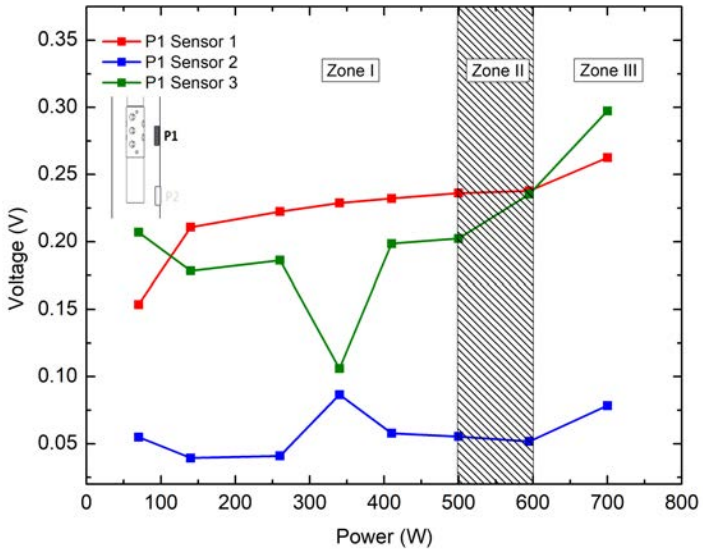

Figure 4.6: Magnitude variation of the sub-harmonic (f/2) for Sensors 1, 2, and 3 at Position 1. The analysis is divided into three zones, Zone 1 (0 W to 500±10 W), Zone 2 (Beginning of cavitation, 500±10 W to 600±10 W), Zone 3 (Developed cavitation, after 600±10 W).

Looking to the responses of Sensors 1 and 3 across various powers, a similar growth pattern is evident, with the exception at 60±10 W and 340±10 W. The spike at 340±10 W is deemed an anomaly and should be excluded from this analysis. This sudden deviation may be attributed to the fact that, in this study, the last cavitation reading was taken at this frequency. This implies that the water temperature may have increased, consequently altering the cavitation response.

The gradual increase seen in almost all range in the acoustic signal, is momentarily interrupted by a

sharp rise within the frequency range of 500±10 W to 600±10 W, mainly on Sensor 3. This could indicate the cavitation threshold. However, this sharp increase is only seen for Sensor 3, being that Sensor 1 only have a sharp increase at 700±10 W.

The noted disparity between the two sensors could be linked to the protective layer present on Sensor 1. This layer might render Sensor 1 less sensitive compared to Sensor 3. The protection provided by the layer may serve as a dampening factor, resulting in reduced sensitivity to the acoustic signals. Other condition is the position of the sensors. Despite their close proximity, the acoustic cavitation could not be uniform across all points, leading to varying measurements, as it will be seen further.

Overall, despite minor disparities at specific frequencies, both sensors in "Position 1" exhibit consistent and nearly identical behavior in response to the acoustic signals. The presence of the protective layer in Sensor 1 could be a contributing factor to the subtle variations observed between the two sensors.

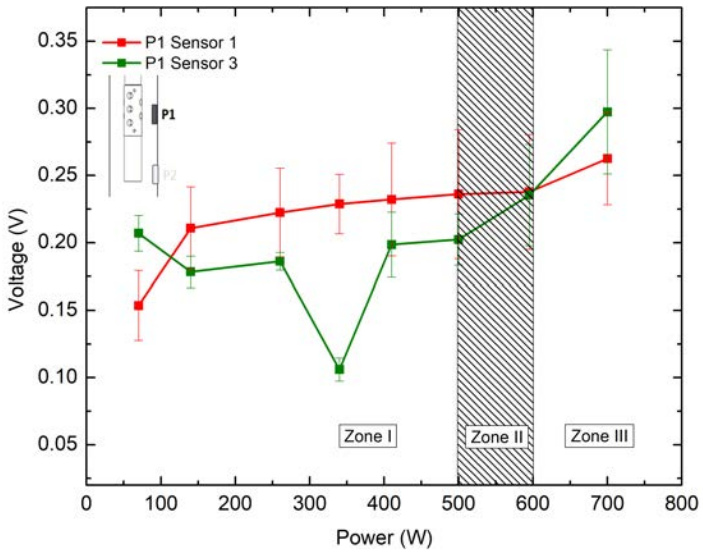

Figure 4.7: Analysis of sub-harmonic magnitude variation for Sensors 1 and 3 at Position 1. Standard deviation aside, line plots show consistent behavior, especially for lower values. Cavitation threshold lies between 500 W and 600 W, marked by a sharp increase. Value at 350 W is negligible, stemming from an instantaneous peak.

In this case, when the acoustic cavitation threshold is not readily discernible, it becomes imperative to verify it through FFT graphics. Additionally, the analysis of sub-harmonic amplitudes across various frequencies must also be corroborated by the FFT graphics derived from the acoustic readings. The acoustic threshold is attained when the magnitude at the ultra-harmonic (3f/2) remains consistent as the frequency escalates. The same behavior is expected for the remaining harmonics. This method serves to substantiate the suggested threshold range through the observation of ultra-harmonics [155, 161].

Figure 4.8 depicts the progression of magnitude for various harmonics, sub-harmonics, and ultra-harmonics at power levels of 260±10 W, 500±10 W, and 700±10 W for Sensor 1 at Position 1. The sub-harmonic (10,000 Hz) amplitude increases proportionally with the rise in power. This behavior is similarly observed for the harmonics, showcasing a comparable peak amplitude at 260±10 W (Figure 4.8 (a)) and 600±10 W (Figure 4.8 (b)), with a more pronounced increase at 700±10 W (Figure 4.8 (c)).

In terms of ultra-harmonics, it is notable that increasing the power leads to an escalation in the ultra-harmonic, although this trend is not as evident for the ultra-harmonic. However, the consistent rise in magnitude around 30,000 Hz, combined with a similar pattern at 10,000 Hz, suggests the presence of cavitation effects between 600±10 W and 700±10 W.

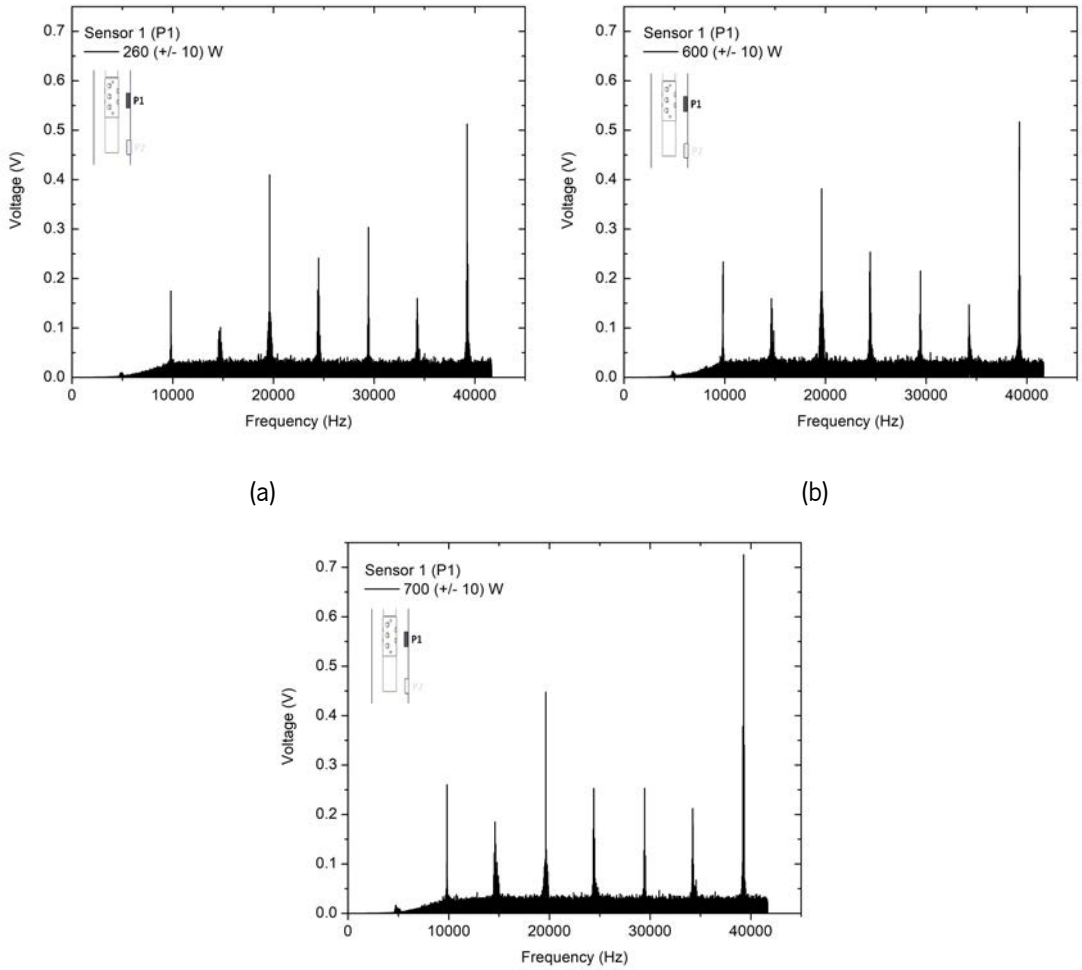

Figure 4.8: Fast Fourier transform graphics for the sensor 1 at position 1 for (a) 260±10 W (b) 500±10 W and (c) 700±10 W.

Respecting to the Sensor 3, Figure 4.9, the analysis is similar. The presence of acoustic cavitation is

demonstrated by the rise in both sub-harmonics and ultra-harmonics, followed by the stabilization of the ultra-harmonics after 600±10 W [161].

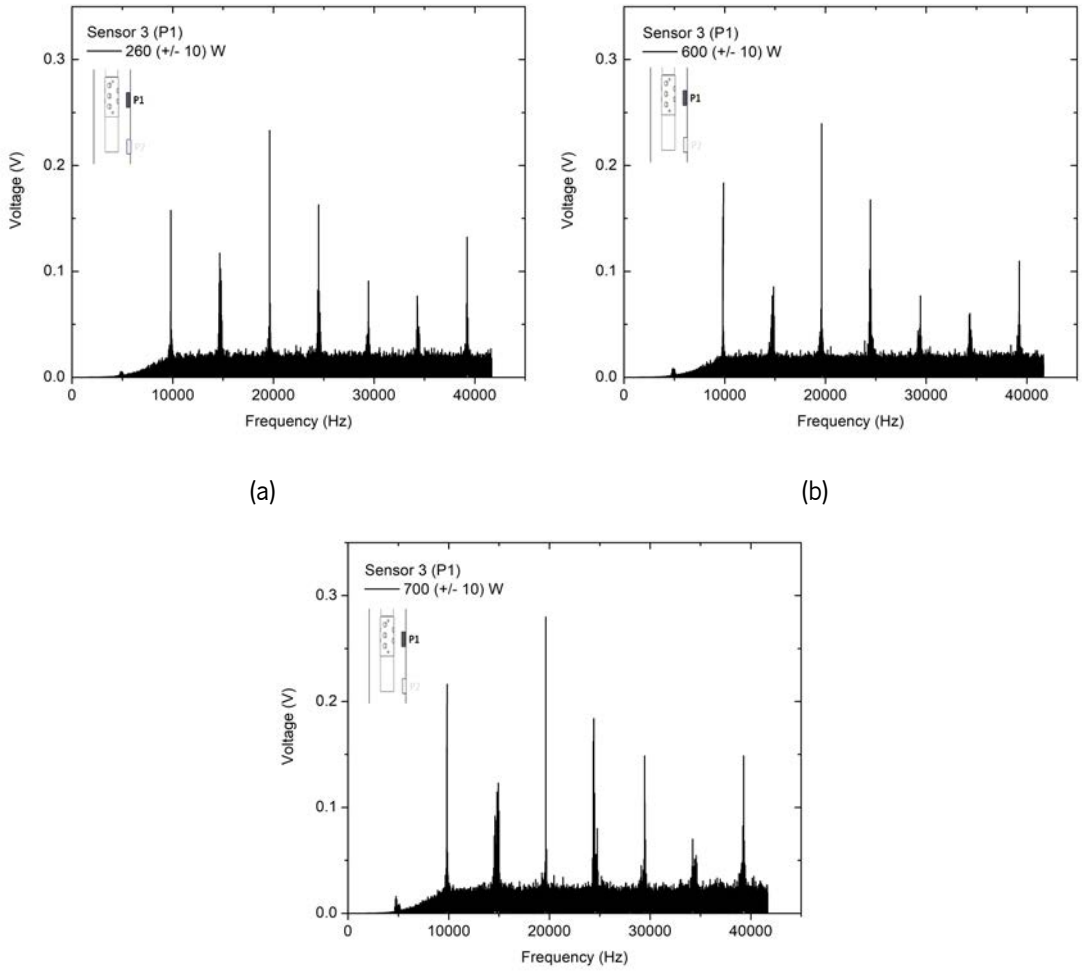

Figure 4.9: Fast Fourier transform graphics for the sensor 3 at the position 1 for (a) 260±10 W (b) 500±10 W and (c) 700±10 W.

Regarding to Position 2, the transition between the zones is observed between the 410±10 W and 500±10 W power. Within this range, a sudden increase in the magnitude of the acoustic signal is evident, indicating the cavitation threshold has been surpassed. However, this observation is only clearly visible for Sensor 1 and Sensor 3. Sensor 2 exhibits erratic behavior without any discernible linear relation. The presence of a fracture in Sensor 2 might suggest that this issue is affecting the accuracy of the readings obtained from this particular sensor. Further investigation is warranted to address this inconsistency in Sensor 2's behavior.

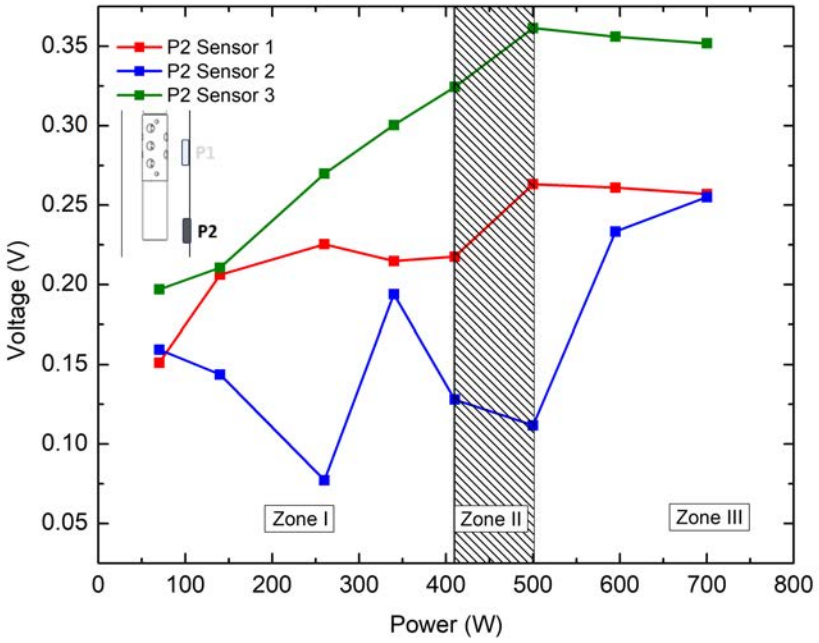

Figure 4.10: Magnitude variation of the sub-harmonic for Sensors 1, 2, and 3 at Position 2. The analysis is segmented into three zones: Zone 1 (0 W to 410 W), Zone 2 (Beginning of cavitation, 410±10 W to 500±10 W), Zone 3 (Developed cavitation, after 500±10 W).

Upon comparing Sensor 1 and Sensor 3, a notable difference is observed in the strength of the acoustic signal, with Sensor 3 showing a much stronger signal. Throughout all data points, the acoustic signal is consistently stronger for sensor three, and at its peak, it reaches approximately 40% higher than that of sensor one. However, after reaching the cavitation threshold, there is not a significant increase in the acoustic signal. In fact, a slight decrease of around 5% is noticeable. This behavior suggests that while cavitation has entered a well-developed regime, the ultrasound action might not be entirely stable. During the experiments, it was observed that high ultrasound powers tend to be less stable, leading to some variations in the acoustic signal input. This instability in the ultrasound action might explain the observed decrease in the acoustic signal after reaching the cavitation threshold. Overall, the comparison between Sensor 1 and Sensor 3, reveals that the absence of the protective layer in sensor three results in a stronger acoustic signal.

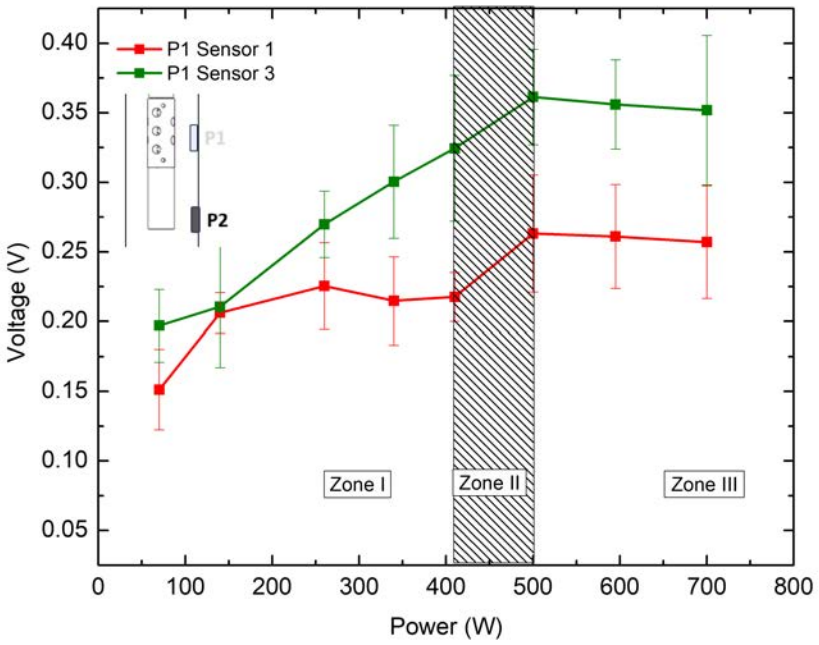

Figure 4.11: Analysis of sub-harmonic magnitude variation for Sensors 1 and 3 at Position 2. The cavitation threshold is between 400±10 W and 500±10 W, marked by a sharp increase. Beyond this threshold, the magnitude stabilizes with a slight decrease.

Analysis of sub-harmonic magnitude variation for Sensors 1 and 3 at Position 1. Standard deviation aside, line plots show consistent behavior, especially for lower values. Cavitation threshold lies between 500±10 W and 600±10 W, marked by a sharp increase. Value at 350 W is negligible, stemming from an instantaneous peak.

Similar to the methodology employed for Position 1, the confirmation of the cavitation threshold hinges on the scrutiny of FFT graphics, specifically focusing on the fluctuations in sub-harmonics and ultra-harmonics in response to power escalation [161]. In Figure 4.12, the variations in magnitude are depicted for power levels of (a) 260±10 W (b) 500±10 W and (c) 700±10 W for sensor 1. As anticipated, at 260±10 W, 3/2f and 2f exhibit a lack of stabilization. However, within the range of 500±10 W to 700±10 W, it is evident that 3/2f and 2f achieve stability and show an augmentation in magnitude concurrent with the increase in power. This observation strongly indicates that the cavitation threshold has been attained, thereby substantiating the previous hypotheses.

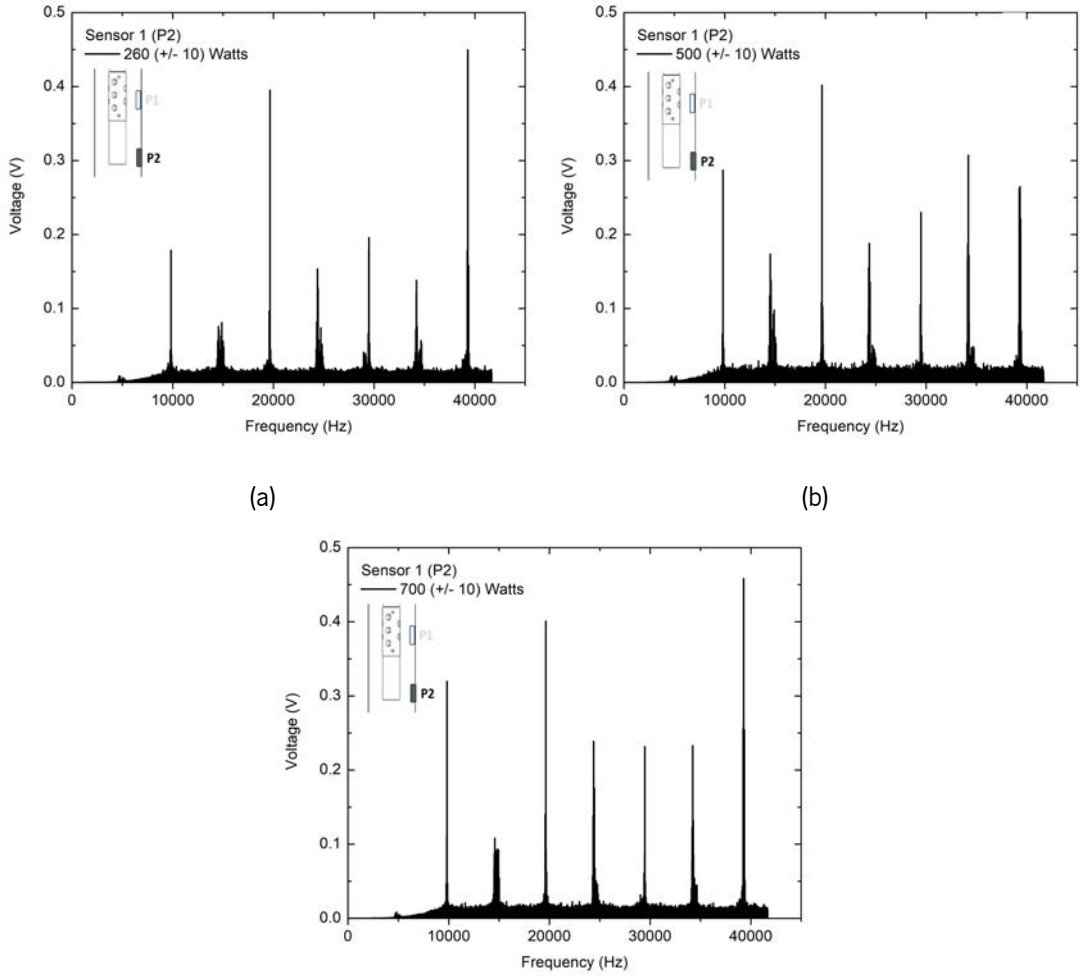

Figure 4.12: Fast Fourier transform graphics for the Sensor 1 at the Position 2 for (a) 260±10 W (b) 500±10 W and (c) 700±10 W.

Regarding to Sensor 3, the same behavior is seen. However, in this case, the increase of the harmonic frequency (20,000 Hz), it is seen more at the power of 500±10 W. However, this is not a problem because second bibliography [161], the ultra-harmonics 3f/2 and 2f, shows a better indicator of acoustic cavitation. In this case, it is possible to see that there is an constant increase of the ultra-harmonics and the stabilization of them, suggesting and confirmed the induction of acoustic cavitation.

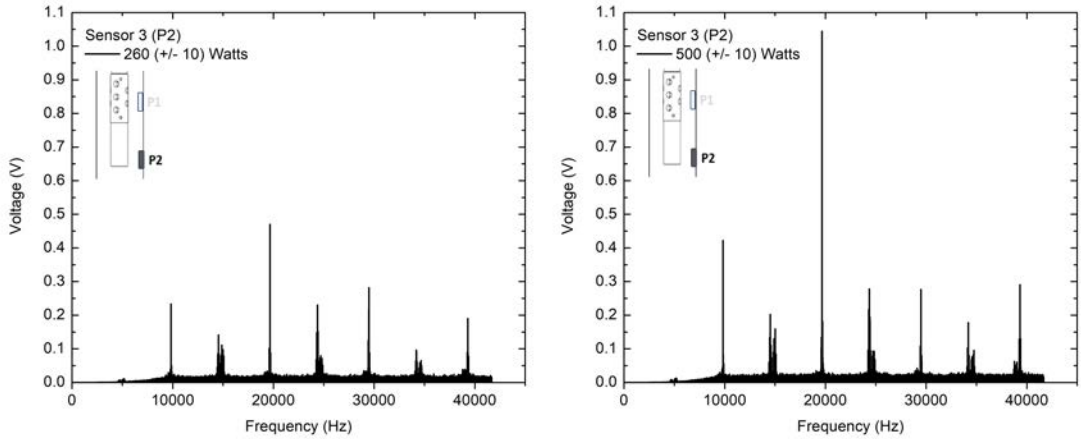

(a)

(b)

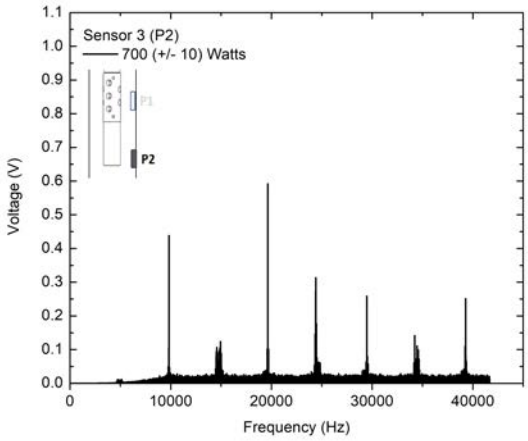

(c)

Figure 4.13: Fast Fourier transform graphics for the sensor 3 at the position 2 for (a) 260±10 W (b) 500±10 W and (c) 700±10 W.

As seen in Figure 4.7 and Figure 4.11, even employing five data points to characterize the acoustic readings, it is evident that there is a notable standard deviation for nearly all points. Nevertheless, this discrepancy does not significantly impact the final results, as the curve consistently follows a similar growth pattern, even when considering the minimum values for each point. The elevated standard deviation suggests the presence of noise, as well as other acoustic waves with varying frequencies and a non-uniform distribution of cavitation within the chamber.

To test this hypothesis, the behavior of cavitation induced by ultrasound in water was studied.

As shown in Figure 4.14, it's evident that cavitation exhibits fluctuations along both the "xx" and "yy" axes over time. Across four distinct time points, each with a one-second interval, noticeable variations in bubble water flux are observed. This highlights that water flow is inherently time-dependent, resulting

in varying pressure fluxes on the water and, consequently, distinct acoustic readings on the piezoelectric sensor. Consequently, making direct comparisons between the two positions is is not possible, as they inherently involve different geometrical parameters of acoustic radiation and waveguide, potentially leading to differing cavitation behaviors.

Additionally, these fluctuations along both axes explain why sensors positioned in the same location might have different cavitation thresholds or measurements.

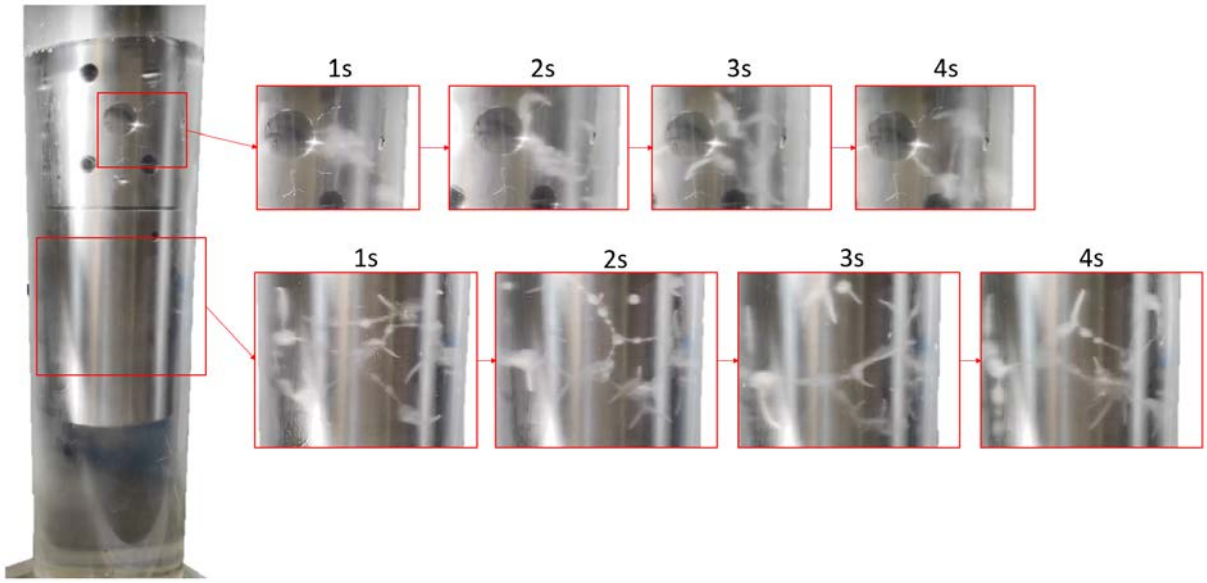

Figure 4.14: Bubble formation due to cavitation over 4 seconds. Cavitation flow changes in axial and radial positions may interfere with acoustic readings due to waves propagating in different directions within the same position.

In Figure 4.15, the formation of bubbles within the holes is clearly observable. It is worth noting that the waveguide and the acoustic radiator demonstrate distinct behaviors when interacting with water. On the waveguide, cavitation primarily occurs around the hole locations, generating elliptical flows outward from these points, acoustic streaming. This geometric characteristic effectively increases the contact area between water and ultrasound, intensifying the cavitation phenomena. However, it is important to highlight that cavitation formation is not solely confined to the hole regions but also extends to the wall side.

As shown in Figure 4.15 (b), the waveguide perforations exhibit two distinct configurations. When the waveguide is excited, the holes undergo a transformation, adopting an elliptical shape that oscillates around their central axis. Initially, the central axis alignment is axial, while the others are radial.

This behavior is mirrored in the ultrasonic acoustic radiator. The acoustic radiator features two primary sources of acoustic propagation, as illustrated in Figure 4.15 (a). Considering the axis of the ultrasound revolution as a reference, it is possible to discern cavitation formation both along this axis and perpendicular

to it. The wave propagation from the cylindrical wall (referred to as the xx axis) is an extension of what occurs on the waveguide.

Regarding the bottom part of the horn, wave propagation occurs through the propagation of acoustic waves along the same axis as the ultrasound. This propagation appears as an inverted mushroom shape at the bottom and a conical shape at the top. Bubble formation is most pronounced at the point of contact with the ultrasound and gradually diminishes visually with increasing distance from it, giving it a conical shape. Simultaneously, the acoustic propagation gradually expands after some distance, until it reaches the bottom of the chamber, resembling a mushroom.

This is a typical behavior for the propagation of cavitation bubbles when using sonotrodes with cavitation formation on the same axis as the ultrasound [162]. The conical bubble structures are referred in literature as common in cavitation produced by these devices [162]. In fact, based on the same investigation, and focusing on the bottom part of the acoustic radiator, the bubble propagation suggests that the quartz particles move towards the periphery, indicating that the vibration is stronger at the center than at the periphery. This is depicted in Figure 4.15, which provides a schematic representation of the observed phenomena. The amplitude of the propagation is higher at the center than at the periphery.

However, when establishing a comparison with the cavitation generated from the waveguide and the acoustic radiator, it is evident that the cavitation bubbles have different configurations, and the propagation is also distinct. Cavitation bubbles produced by the acoustic radiation suggest that the amplitude is higher at the center and the propagation is in a conical shape. In contrast, at the contact surface between water and the acoustic radiator, taking into account the cavitation bubble structures, the acoustic streaming is propagated from the center to the outside [162].

However, the phenomenon observed here differs from that presented by the waveguide. Due to the presence of holes, the propagation in the waveguide seems to amalgamate two distinct types of cavitation bubble structures along with acoustic streaming. In this case, the cavitation bubble structure may not be entirely discernible, but the presence of acoustic streaming is conspicuous.

Upon comparing the studies of Moussatov et *al.* [163] and Bai et *al.* [162] with the pattern illustrated in Figure 4.15, it is possible to observe that along the waveguide, there are zones where acoustic streaming occurs in isolation. Furthermore, it tends to shift from the center towards the periphery in some areas, while in others, it moves from the periphery towards the center, forming a distinctive ”X” shape.

This behavior strongly suggests that the amplitude of vibrations is influenced by the presence of holes, resulting in a geometric configuration where certain areas exhibit higher amplitudes while being surrounded by regions of lower amplitudes, and vice versa.

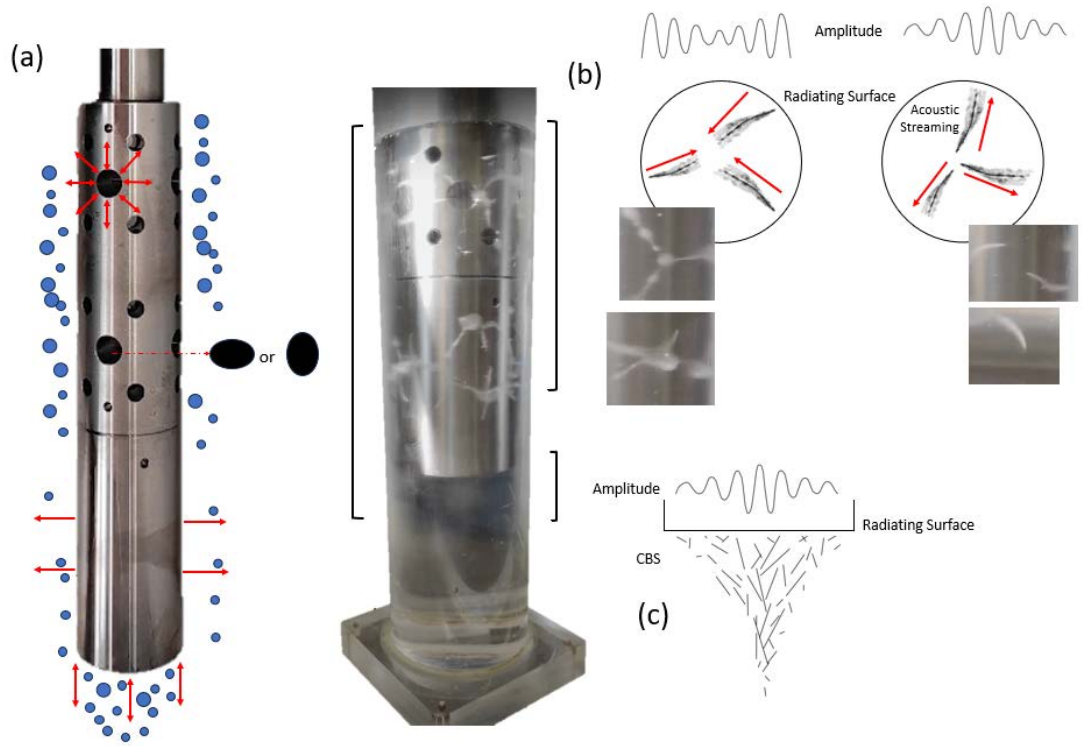

Figure 4.15: Cavitation generation by the ultrasound acoustic radiator (a) Ultrasound induces cavitation with axial and radial movements, creating centrifugal flow. Axial movements at base generate cavitation-aligned acoustic waves. (b) Acoustic streaming distribution along wave guide, low and high center amplitude. (c) Conical bubble structure on ultrasound acoustic radiator tip.

In Figure 4.9, Figure 4.8, Figure 4.12, and Figure 4.13, discernible peaks emerge around 15,000 Hz, 25,000 Hz, and 35,000 Hz. Notably, these peaks exhibit lower magnitudes in comparison to those of the sub-harmonics, harmonics, and ultra-harmonics. By examining the relationship between the frequency at which the maximum voltage is attained for these peaks and its association with the resonance phenomenon, it becomes evident that there exists a consistent difference of 1 harmonic between each noise peak. This value aligns with the harmonic, as illustrated in Figure 4.16.

Given the traceable mathematical relation and the consistent presence of a peak between each harmonic, distinct from one complete harmonic, it is proposed that these peaks result from the resonance and refraction occurring within the chamber itself. The refraction of acoustic waves within the ultrasound chamber gives rise to additional frequency peaks.

Regarding to the impact load reading by the sensor, it was considered the 10 most high values of all reading for each point and calculated the mean. As it can be seen on Figure 4.17 (a), the standard average error it is not high enough to interfere on the final results. Once that the transformation from voltage to impact load is made by a equation, the standard deviation from the voltage can not be considered in the

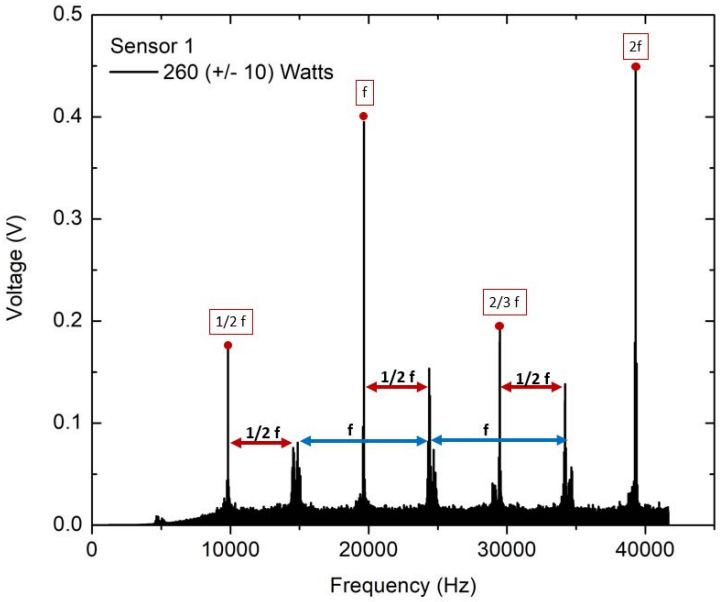

Figure 4.16: Analysis of the distribution of the noise on the voltage acquisition and it relation with the sub-harmonic, harmonic and ultra-harmonic.

impact load. It was used just the mean values but always considering that the values does not impact significantly the voltage acquisition.

Given that Sensor 2 is inoperable, Figure 4.5, and Sensor 1 lacks the necessary sensitivity to trace the force calibration curve, Figure 4.1, only results from Sensor 3 were taken into consideration for force readings. In Position 1, the maximum impact load value is 12.25 V, achieved at a power of 700±10 W. As observed previously, a dip in voltage values at 410± W corresponds to a lower impact load.

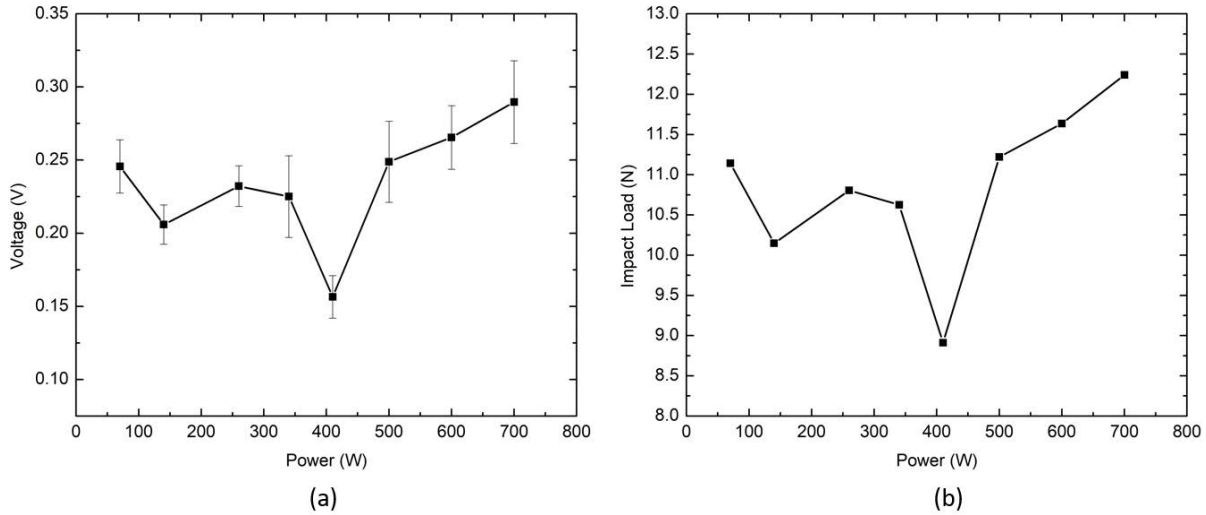

Figure 4.17: (a) Voltage Values Recorded by Piezoelectric Sensor 1. (b) Corresponding Impact Load Calculated Using the Previous Calibration Line and the mean voltage value.

In Position 2, the behaviour similarly aligns with the sub-harmonic pattern over time. The maximum recorded impact load is 15.25 N, achieved at a frequency of 500±10 W. Following this peak, the intensity gradually diminishes until 700±10 W. As mentioned earlier, the occurrence of a peak was not anticipated, as a linear and continuous growth was expected. However, it is noteworthy that the tests were conducted sequentially, with the final test at the highest power level, resulting in elevated temperatures of both the ultrasound equipment and water. This elevation in temperature induced some deviations from the normal functioning of the ultrasound system.

Comparing with the research made by Wang et *al.* [159] the acoustic cavitation, at 0.3 mm of distance between the source of cavitation and sensor, is 0.2 kN. In this case, the distance between them is 15 mm, making it impossible to made a linear relation between them.

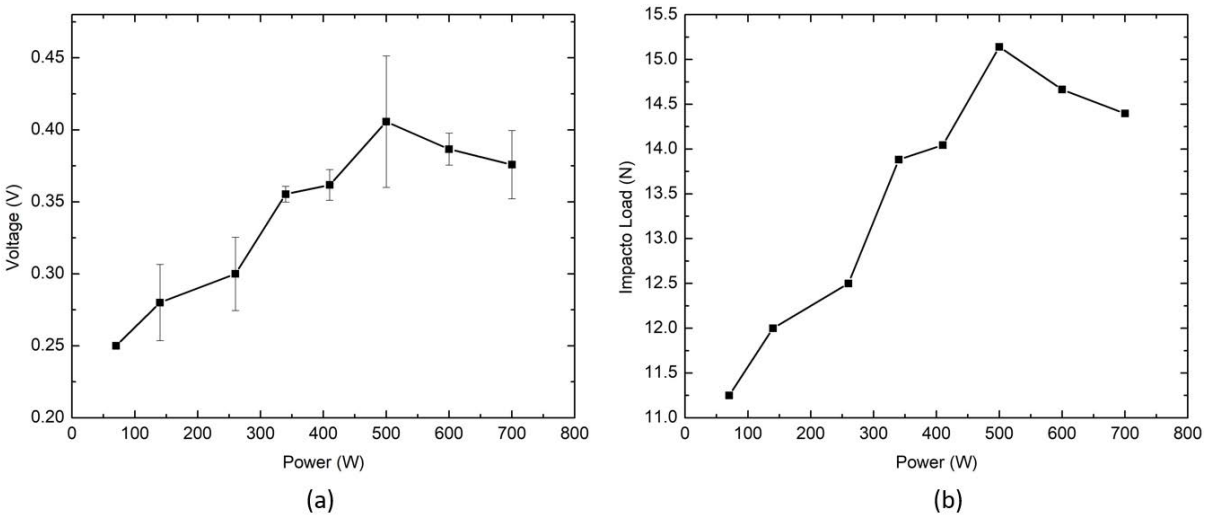

Figure 4.18: (a) Voltage Values Recorded by Piezoelectric Sensor 2. (b) Corresponding Impact Load Calculated Using the Previous Calibration Line and the mean voltage value.

4.1.3 Resonance Frequency Analysis of Piezoelectric Sensors

As previously noted, Sensor 2 displays notable damage attributed to the cavitation effect (see Figure 4.5). The FFT graph findings strongly indicate sensor impairment, making it unreliable for acoustic cavitation measurements. To address potential test errors that could have affected sensor responses, the sensor's natural resonance was evaluated using a TRZ analyser. When examining the impedance of Sensor 2, the TRZ analyser did not identify any significant variations. This reinforces the assessment that the piezoelectric sensor is impaired and cannot be deemed suitable for precise measurements.

For the remaining sensors, it was compared the resonance frequencies in three phases of the piezoelectric material, the original and final configurations, Figure 4.19. In this case, what is pretended is

to understand what is the main consequence of applying an Epoxy layer and cut in a square the initial ceramic disk. The first configuration is the initial one, without any geometrical change (Piezoelectric A). The second configuration is the final configuration with the ceramic disks with new dimensions and with an Epoxy film (Piezoelectric B).

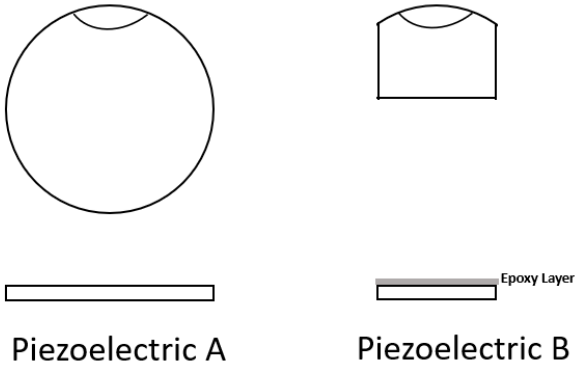

Figure 4.19: Piezoelectric sensors with two geometries. Piezoelectric A represents the unmodified piezoelectric, while Piezoelectric B denotes the final geometry and its corresponding Epoxy layer.

Concerning the original configuration, Figure 4.19 (a), Figure 4.20 illustrates that the resonance frequency is 44,550 Hz, while the anti-resonance is at 45,480 Hz. These values fall within the tolerance range of resonance indicated by the manufacturer, see Appendix A, that was 44±2 kHz.

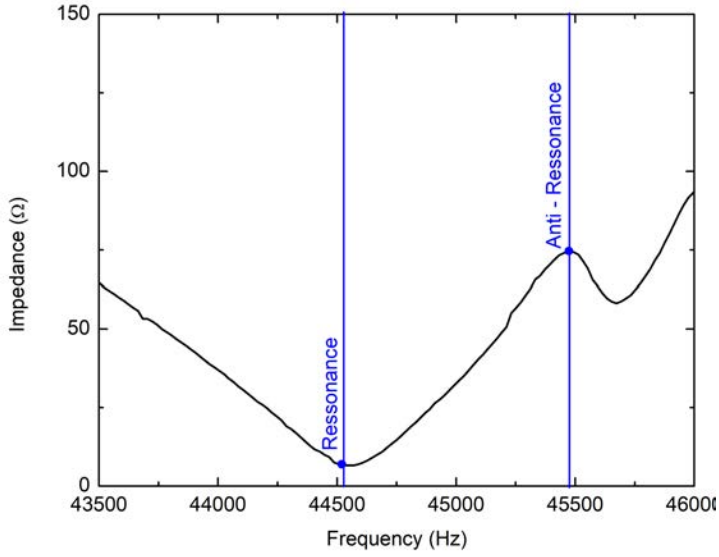

Figure 4.20: Impedance graphic for piezoelectric A with the Resonance t 44,550 Hz and anti-resonance at 45,480 Hz.

Turning the attention to the piezoelectric sensor with the epoxy layer, Piezoelectric B, Figure 4.19 (b), it is observed that the first resonance fall in the expected value, 44,550 Hz, while the second fall out,

46,500 Hz, Figure 4.21. The corresponding anti-resonance frequencies are 45,530 Hz and 47,520 Hz, respectively.

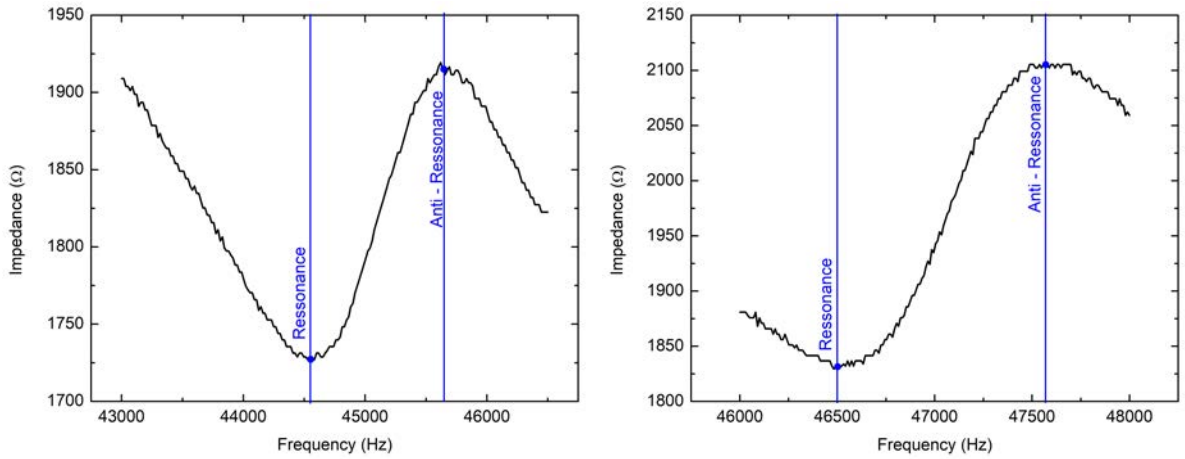

Figure 4.21: Impedance graph for Piezoelectric B, which includes the epoxy layer, two distinct resonances and anti-resonance are evident: (a) at 44,550 Hz and 46,500 Hz and at (b) 46,500 Hz and 47,520 Hz.

When comparing both graphs, it becomes evident that both configurations exhibit one resonance frequency within the expected range. Piezoelectric A and B share a similar primary resonance, differing by a maximum of only 110 Hz, which is negligible, Table 4.1. However, the modification of the geometry leads to a new resonance frequency at 46,500 Hz.

The analysis of these two sensors confirms that they adhere to the manufacturer's specifications. However, the resonance outside the specified range can be attributed to modifications in the geometry and the addition of an epoxy layer to Piezoelectric B during its construction.

Furthermore, it is noteworthy that the epoxy layer, at this stage, does not appear to significantly affect the behavior of the piezoelectric material. The resonance frequency remains consistent across different sensors, indicating a similarity in their performance.

Table 4.1: Resonance and Anti-Resonance comparison between Piezoelectric A and B.

	Resonance	**Anti-Resonance**	**Resonance**	**Anti-Resonance**
Piezoelectric A	44,550 Hz	45,450 Hz	-	-
Piezoelectric B	44,550 Hz	45,560 Hz	46,500 Hz	47,550 Hz

The cavitation and wave propagation vary with the frequency of the ultrasound [106]. This variation is influenced by the volume of water inside the chamber, which consequently affects the contact area between

the ultrasound and the water. To analyse the relation between the contact area and the ultrasound's effect on water, a study was conducted. The ultrasound was brought into contact with water at different depths. In this scenario, the point labelled as zero represents the initial contact between the water's surface and the tip of the ultrasound face, signifying the minimum possible contact between them. The other points analysed were at depths of 80 mm (Position 1), 180 mm, 280 mm (Position 2) and 300 mm, 4.22 (a).

As depicted in Figure 4.22 (b), an increase in the contact area between the ultrasound and water influences the resonance frequency. Progressing from the first to the last position, the ultrasound frequency decreases from 19,650 Hz (at 0 mm depth) to aproximatdly 19,220 Hz (at 180 mm and 280 mm depths) and 19,150 Hz (at 300 mm depth). Increasing the area of contact, the resonance decrease. It is also evident that with an increase in depth, the impedance graph exhibits more noise. This phenomenon can be attributed to the presence of resonance-induced noise in the water and its subsequent attenuation.

The existence of noise can be also linked to the emergence of new resonances. At a distance of 300 mm, a minor resonance is observable, potentially attributed to the substantial mass of water in direct contact with the upper part of the ultrasound device. This gives rise to a secondary reaction, resulting in the appearance of a new cavitation source above the ultrasound apparatus. Throughout the tests, this phenomenon became conspicuous, causing instability in the system and introducing problematic behavior in the ultrasound operation.

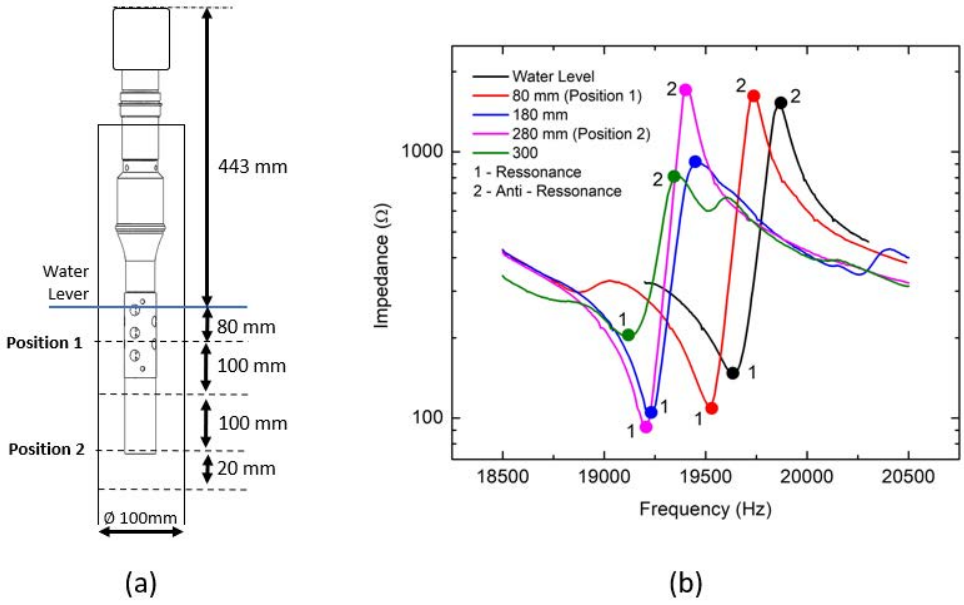

Figure 4.22: Ultrasound Resonance Test. (a) Conducted at different levels of submersion in water. (b) Resonance at minimal water contact measured at 19,700 Hz. Decreasing submersion depth led to a decrease in resonance frequency.

4.1.4 Ultrasound Effects on Water and Water-Oil Mixture

Simultaneously, with the automation of the previous ultrasound system, a study was conducted using a smaller ultrasound device to comprehend the water flow and variations in key water quality parameters.

This initial test focused on the behaviour of a water and oil mixture when applied the ultrasound system. To conduct this experiment, a solution was prepared by blending 1 L of water with 10 mL of SAE 10W40 oil produced by Castrol. Ultrasound was applied to this solution for a total duration of 2 minutes, operating in cycles of 15 seconds on and 15 seconds off. The ultrasound power was set at 65W with a tolerance of 5W, resulting in a power intensity of 20.7 $W \cdot cm^{-2}$, calculated using Equation 2.12. A camera was strategically positioned to capture the entire solution flow.

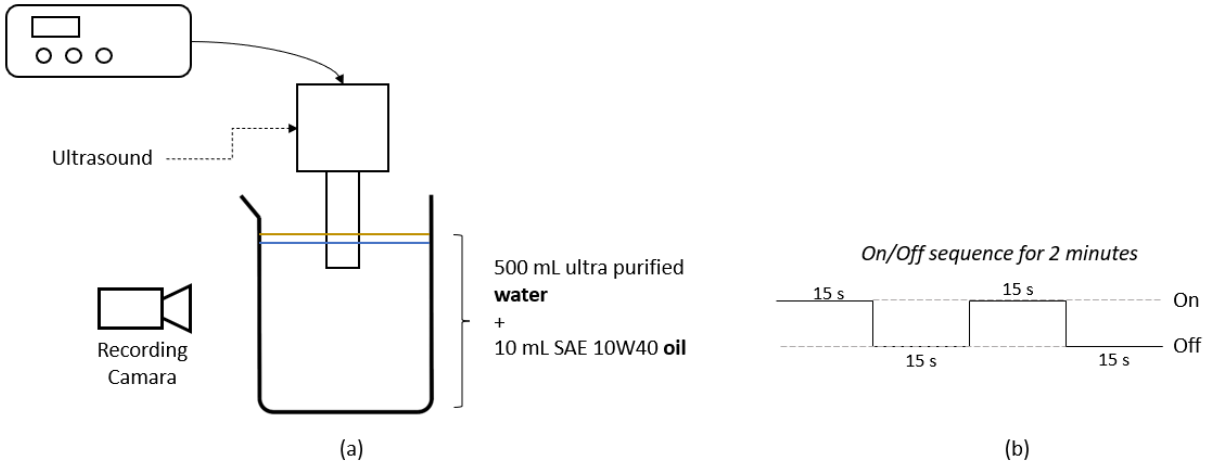

Figure 4.23: Flocculation and coagulation test on water-oil mixture: (a) Experiment: 500 mL beaker with 500 mL water and 10 mL SAE 10W40 oil. (b) Intermittent ultrasound treatment: 15 seconds on, 15 seconds off, for 2 minutes.

In Figure 4.24, the chronological sequence of events during the test is presented. At the initial time point, as depicted in Figure 4.24 (a), representing the condition before activating the ultrasound, a thin film of oil is visible on the surface of the water. The oil and water do not naturally mix due to their differing polarities and densities, causing them to separate into distinct layers when combined [164].

As the experiment progresses to the 2 seconds mark, as depicted in Figure 4.24 (b), a distinctive white mixture starts to take shape, forming an inverted mushroom-like structure originating from the ultrasound tip. This phenomenon vividly illustrates the impact of ultrasound waves on the water. It provides insight into the path of acoustic propagation along the revolution axis of the ultrasound, and it's notable that the diameter of acoustic influence tends to expand with distance from the ultrasound source. Additionally, there is noticeable vortex formation and reflux along the beaker's wall during this initial phase. However,

it's worth noting that this visible effect is primarily observed within the first two seconds.

Subsequently, the mixture becomes uniformly white, making it challenging to discern specific fluid dynamics, as seen in Figure 4.24 (c). Nevertheless, based on initial observations, it is anticipated that the water flow pattern remains consistent with what was presented in 4.24 (b). The intense mixing suggests that the flow phenomena persist and simultaneously enhance the visual mixing of water and oil.

Upon concluding the three minutes of ultrasound application, the water-oil solution remains highly turbid, with no signs of flocculation or coagulation initiation, as indicated in Figure 4.24 (d). In fact, the ultrasound tends to emulsify the solution and hinders the flocculation/coagulation process. After one week, the solution still appears white and shows no discernible changes.

The quick mixing of the two fluids, in conjunction with insights from the cited literature on the effects of ultrasound on the increased efficiency of coagulation and flotation processes [66, 68, 165], suggests that ultrasound could enhance the mixing between the solution and the coagulant. However, given the absence of specific studies on the application of ultrasound systems to coagulation/flotation processes for oil removal, the results obtained from the analysis of water flow behaviour serve as a basis for further investigation. This study should be extended, introducing coagulants to explore their potential impact on the overall process.

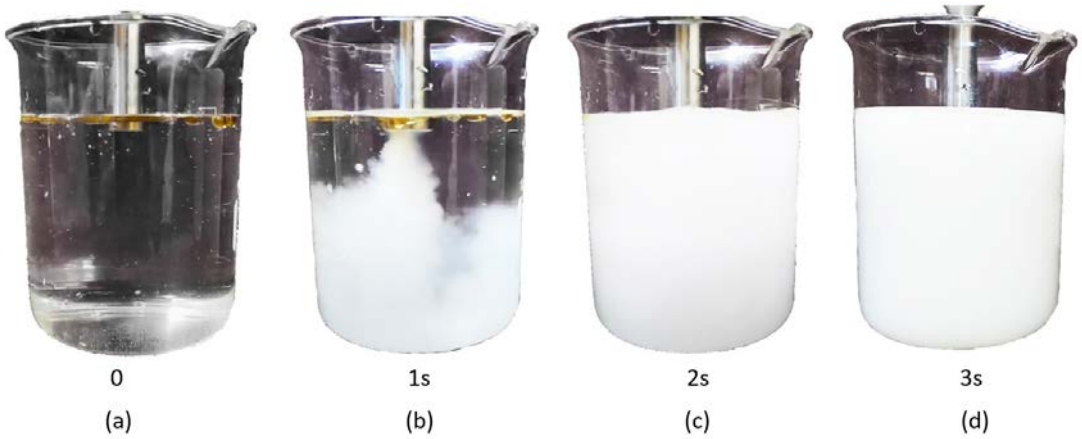

Figure 4.24: Mixture visual behaviour over 3 minutes. (a) Initial state pre-ultrasound. (b) Movement of water mixture in the first second after ultrasound, forming an inverted mushroom-shaped white mixture. (c)(d) By the second second, the mixture is entirely white.

To gain a deeper understanding of fluid movement at the bottom of the ultrasound acoustic radiator and its implications for the movement of solids within the solution, an investigation was conducted by studying the water flow with the integration of wax beads. As depicted in Figure 4.25 (a), the wave propagation on this Ultrasound begins with the sound travelling through the water from the base of the

acoustic radiator.This principle mirrors the approach employed at the base of the acoustic radiator in the primary ultrasound system, serving as a reference point to comprehend the dynamics occurring within it. It is noticeable that the flow propagation aligns with the axis of the horn's output tip. The pressure waves emanate from the bottom of the ultrasound transducer in a vertical direction, colliding with the beaker. Consequently, the water molecules in this region are displaced outward, resulting in a continuous motion phenomenon throughout the duration of the ultrasound application, as shown in Figure 4.25 (b). This fluid movement appears akin to an inverted mushroom shape. The cavitation shape, as seen before, correspond to a bubble structure, typical of ultrasonic horns of this type [163]

The molecules are pushed towards the beaker's sidewall, concurrently generating a centrifugal flow near the beaker's wall. Observable features include regions of reflux and the creation of vortices, as depicted in Figure 4.25 (c). This phenomenon is particularly pronounced at the onset and persists throughout the ultrasound action.

Once cavitation is established, and the system reaches a stable phase, two distinct phenomena become apparent. At the bottom, pressure waves continue to generate the centrifugal flow, while those able to escape the ultrasound field ascend and, at the top, re-enter the cavitation field, resulting in their descent, see Figure 4.25 (d). This process unfolds continuously, providing insights into wave propagation patterns through this type of horn and the distribution of flows along the beaker.

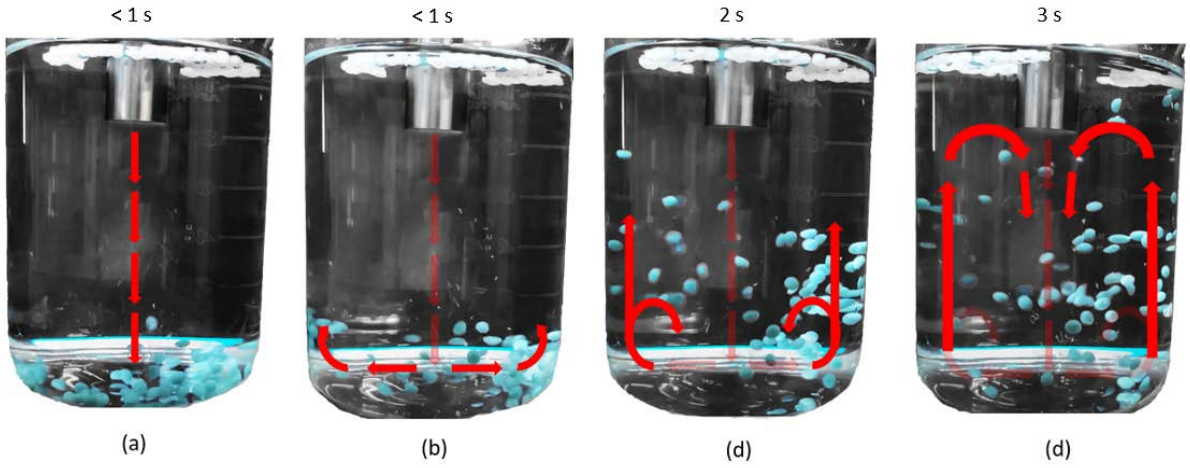

Figure 4.25: Sequence of Water Flow Movements upon Contact with Ultrasound. (a) Initially, the wave propagates along the same axis as the ultrasound. (b) Upon reaching the bottom, the flow tends to dissipate towards the base, causing radial movement. (c) The flow now has two paths: it can ascend through the sides, escaping ultrasound, or remain at the bottom as refluxes. (d) Escaped molecules are recirculated to the bottom due to continued ultrasound action.

4.2 Ultrasound Effects on Water Characteristics and Adsorption

Before beginning the analysis of parameter variations over time, it is crucial to establish the method for data analysis. The assessment of parameter variation will involve considering the relationship between the initial and final values, as expressed by the equation,

$$C(\%) = \frac{C_i - C_0}{C_0} \times 100 \tag{4.1}$$

where C is the variation from the initial point in percentage, C_i is the value at time i and C_0 is the initial value. It is important to mention that the units on the initial values must be the same as C_i.

4.2.1 Impact of Ultrasound on ORP and pH

Focusing on the effects of cavitation on water characteristics, the investigation shifted towards examining variations in pH and ORP for both tap water and ultra-filtrated water. To assess the influence of ultrasound on water, a study was conducted to investigate the effects of ultrasound at a electrical power of 65 $\pm$ 5 W, 20.7 W ($\pm$ 1.6 W·m^{-2}) on a 500 mL beaker containing ultra-filtrated water or tap water. Every 18 seconds, pH and ORP were measured using the HI8424 equipment and recorded. In parallel, a similar experiment was conducted without applying ultrasound, simply allowing the water to come into contact with air. The experiment lasted for 144 seconds and aimed to understand the increase in reaction speed facilitated by ultrasound.

Beginning with the analysis of ultra-filtrated water, particularly focusing on ORP, Figure 4.26 (a) provides a clear visual of the impact of acoustic cavitation on the ORP. The initial 18 seconds witnessed a rapid surge, marking a 2.52-fold increase. Following this initial surge, the application of ultrasound exhibited minimal impact on the ORP, aligning closely with instances where ultrasound was not employed. The values of $\Delta 1$ and $\Delta 2$ further underscored comparable rates of increase.

Comparing the pH, as depicted in Figure 4.26 (b), it is notable that in the first 18 seconds, the pH decreased 2.29 times faster compared to when ultrasound was not applied. The difference in growth rates persisted until around 40 s, after which the behaviors became similar. At 50 s, the difference in pH between the two conditions was 6 units, which reduced to 4 units at 60 s and remained constant for the rest of the experimental test.

The graphical representations of the pH and ORP data further support that ultrasound enhances

chemical reactions in the water. The data suggest that ultrasound action promotes more oxidative reactions, enhancing the oxidation process and accelerating chemical reactions. In this case, ultrasound appears to act as a catalyst, exerting a significant effect initially, thereby intensifying its impact on the water.

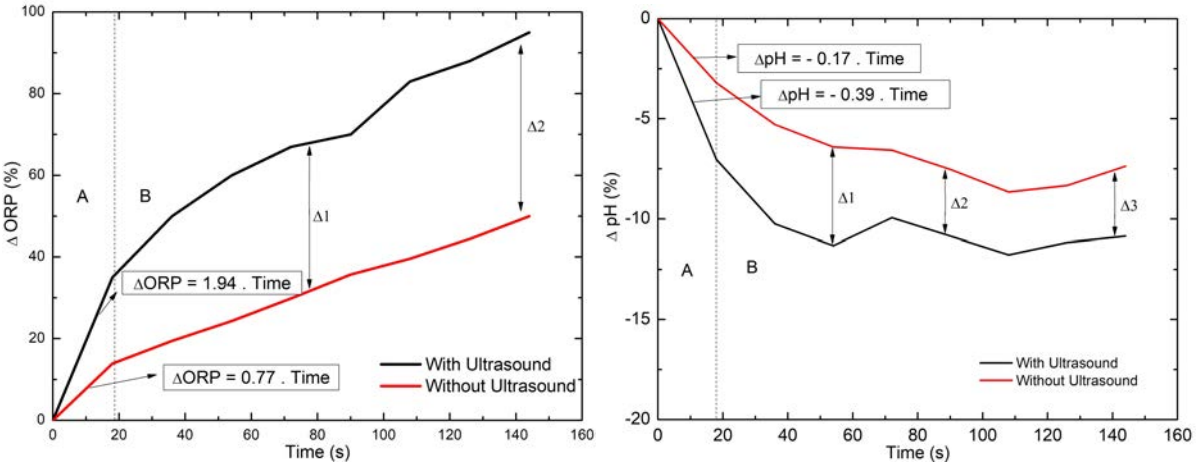

(a) (b)

Figure 4.26: Effects of acoustic cavitation on the ORP and pH of ultra-filtered water. (a) The ORP increases 2.52 times fast with ultrasound action and then stabilize. (b) The decreases 2.29 times faster and then stabilize as well.

When observing the evolution of the same parameters for tap water, several interesting observations were made. Without ultrasound action, the ORP did not exhibit any significant variation. However, when ultrasound was applied, two distinct zones were observed. The first, referred to as Zone "A" in Figure 4.27 (a), was characterized by a slight decrease in ORP. Following this initial period, ultrasound had a pronounced effect, leading to a significant decrease in ORP values. Comparing the points at 40 s, 90 s, and 140 s, the differences in ORP without ultrasound were 14 units, 24 units, and 28 units, respectively. The action of ultrasound on tap water appears to enhance its capacity to donate electrons, resulting in oxidation processes. This phenomena is constantly growing, within the study 142 s range.

Concerning the pH behaviour, as illustrated in Figure 4.27 (b), ultrasound induces a rapid increase of 20%. Subsequently, there is no significant difference between the use and non-use of ultrasound until the 72-second mark. At this point, ultrasound action prompts a swift pH increase over the next 18 seconds, reaching a stable value. This maintained difference persists over time when ultrasound is not employed. As the process of oxidation progressed, the increasing pH suggests that the solution released hydroxide ions (OH-), which contributed to the reduction of another substance. However, this phenomena tends to be more intense at certain point of the experiments.

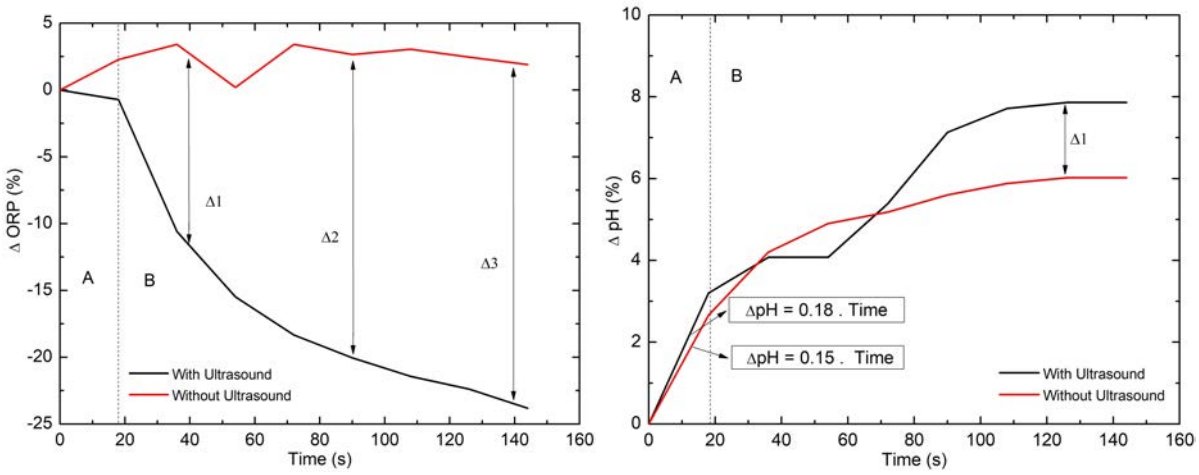

(a) (b)

Figure 4.27: Effects of acoustic cavitation on the ORP and pH of ultra-filtered water. (a) The ultrasound action promotes an exponential decrease over the ORP values and (b) the same action promotes only a difference on pH after 70 seconds.

Comparing the two cases, ultrasound had different consequences on the ORP and pH behavior. For ultra-filtrated water, the ability to acquire electrons was higher and was further enhanced by ultrasound. Additionally, oxygenation increased with ultrasound, as indicated by the rise in ORP, which is associated with the influx of oxygen into the solution. Combining the increase in ORP with the decrease in pH confirms that the solution's oxidative potential is augmented.

The differences in pH and ORP behaviors for the two types of water can be attributed to the availability of electrons in the solutions. Solutions with more electrons (tap water) will experience a decrease in electron species (as they are donated to other substances), while solutions with fewer electrons will exhibit an increase in electron concentration. This, coupled with the fact that the processes shown in Figures 4.26 and 4.27 demonstrate opposite behaviors under ultrasound, suggests that acoustic cavitation accelerates the rate of natural reactions. This is further supported by the comparison of pH and ORP values with and without ultrasound use. The graphs exhibit similar behavior, but ultrasound reduces the time taken to reach the final values.

4.2.2 Ultrasound Impact on Adsorption Processes

Focusing now on the potential enhancement of adsorption through the concurrent application of ultrasound and mechanical action. This research focus on the removal of both organic and inorganic pollutants, specifically Ciprofloxacin and Copper. To ensure the robustness of the experiment, ultrasound

and mechanical actions were applied in a staggered manner. The ultimate goal is to conduct a comparison between the use of ultrasound and mechanical agitation, aiming to gain valuable insights into the enhancement of adsorption through ultrasound.

Ultrasound action, Figure 4.28 (a) and mechanical action, Figure 4.28 (b), operating at a rotational speed of 30 revolutions per minute (rpm), were carried out with a time lag between them to validate the viability of the test. The ultrasound power was meticulously maintained at a consistent level of 65W, with a permissible deviation of 5 W. This was achieved through a regulated cycle of 15 seconds "ON" and 15 seconds "OFF", allowing precise control over the ultrasound application. The entire experimental duration was meticulously standardized to 30 minutes. Different containers were used for each equipment due to their unique characteristics: ultrasound was applied in a beaker, while mechanical action was executed using a closed bottle.

(a) (b)

Figure 4.28: Equipment used for the adsorption tests. (a) Ultrasound with the beaker with the solution to treat. The beaker is in a water cooling system with a tank with water. (b) Rotational machine for the mechanical action.

The initial step involved preparing a solution consisting of 500 mL of ultra-filtrated water, 8 mg/L of Cu, and 2 grams of the organic compound, Nutrimais by Lipor. Subsequently, another solution was prepared, comprising 500 mL of ultra-filtrated water, 8 mg/L of Cu, and 2 grams of Kaolinite.

To investigate the removal of organic pollutants, solutions were prepared, each containing 500 mL of ultra-filtrated water, 15 mg/L of Ciprofloxacin, and specific adsorbents. One solution included 2 grams of the Nutrimais (Organic Compound), while another incorporated 2 grams of Kaolinite. Additionally, a

solution with 500 mL of ultra-filtrated water and 15 mg/L of Ciprofloxacin was prepared as a control group.

Temperature measurements were recorded to understand their potential effects on the final results.

To enhance the affinity for adsorption, the OC compound and Kaolinite were introduced into the solutions 30 minutes before the experiment commenced. At the onset of the experiment (minute 0), reference samples were included for each prepared solution, serving as a baseline for comparison. Subsequently, samples were extracted at specific time intervals, collected at minute 1, minute 5, minute 15, and minute 30. Notably, for ultrasound collection, no specific downtime was required, whereas, for mechanical action collection from the bottle, a 1 minute pause was necessary between each collection.

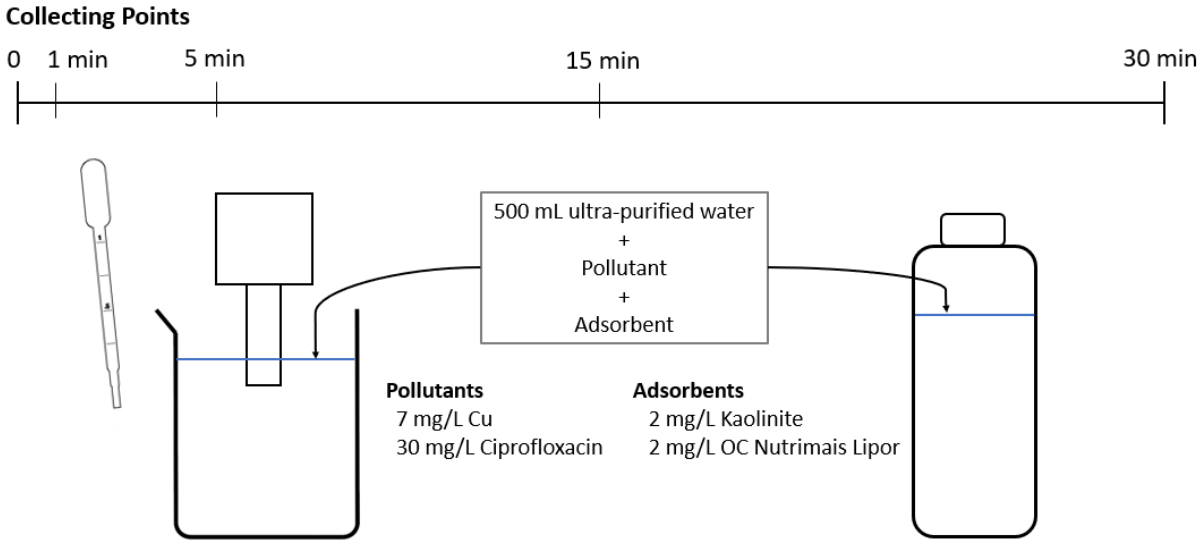

Figure 4.29: Experimental procedure for the adsorption tests. Each experiment has 500 mL of ultra-filtrated water, pollutant solution and adsorbent. In some cases, the adsorbent is not used. The time points for the samples removal it were 0, 1, 5, 15 and 30 minutes.

To measure organic and inorganic concentrations, two distinct instruments were employed. For the measurement of organic concentrations, it was made by the Chemical Engineering laboratory of University of Minho by HPLC technique. Regarding the analysis of inorganic concentration, it was employed the Hanna HI83399, a multi parameter photometer. Once that it was used concentrations above 5 mg/L, it was necessary to dilute the initial solution. The initial solution was diluted in a 50% concentration solution, with introduction with 50% in volume of ultra-filtrated water. Specific measurement procedures were followed to obtain accurate readings.

Figure 4.30: Hanna 83300 for the measurement of inorganic pollutants concentration on the samples.

To enhance the efficiency of the adsorption rate, it is crucial to differentiate the analysis for Kaolinite and Organic Compound. As depicted in Figure 4.31 (a), Ciprofloxacin adsorption after one minute is higher with mechanical action compared to ultrasound action. With mechanical action, adsorption reaches a maximum of 66%, whereas with ultrasound, it reaches only 59%. However, it is evident that after 5 minutes, ultrasound-assisted adsorption surpasses mechanical action. Another phenomenon observed is that ultrasound raises the adsorption threshold. The maximum adsorption rate achieved with Kaolinite + US is 71%, while MA + Kaolinite only reaches 68%. In terms of using ultrasound alone, its effects are negligible, with a maximum removal of only 20%.

When employing Organic Compounds as adsorbents, the Ciprofloxacin removal rate reaches 69% at the end of one minute with ultrasound assistance. Mechanical Action with Kaolinite only achieves 40%. As shown in Figure 4.31 (b), the maximum removal rate for this adsorbent under these conditions is attained with US + OC at the end of one minute, while MA + OC only reaches this level at the end of 15 minutes.

Ultrasound-assisted action significantly enhances the maximum adsorption when combined with both Kaolinite and Organic Compounds. While MA + Kaolinite results in slightly higher Ciprofloxacin removal after 1 minute, the difference is only 9%. However, when used alone, ultrasound demonstrates limited efficacy in Ciprofloxacin removal. This weak performance of ultrasound aligns with existing literature, which indicates that while sonochemistry can initiate oxidative processes, it may not lead to substantial mineralization abilities [166]. Mineralization or removal needs to be facilitated by other AOPs processes or adsorption [166].

Regarding temperature variations during the ultrasound process, there is an immediate increase upon ultrasound application. After one minute, the temperature rises by 2°C, and after 10 minutes, it increases by approximately 8 °C. While temperature may play a role in Ciprofloxacin removal, it is likely not substantial, as the increase after one minute is only 2 °C, and yet the removal rate reaches its

maximum. Moreover, the removal rate does not experience a significant increase with ultrasound application alone, even though the temperature rises by over 10 °C by the end of the experiment.

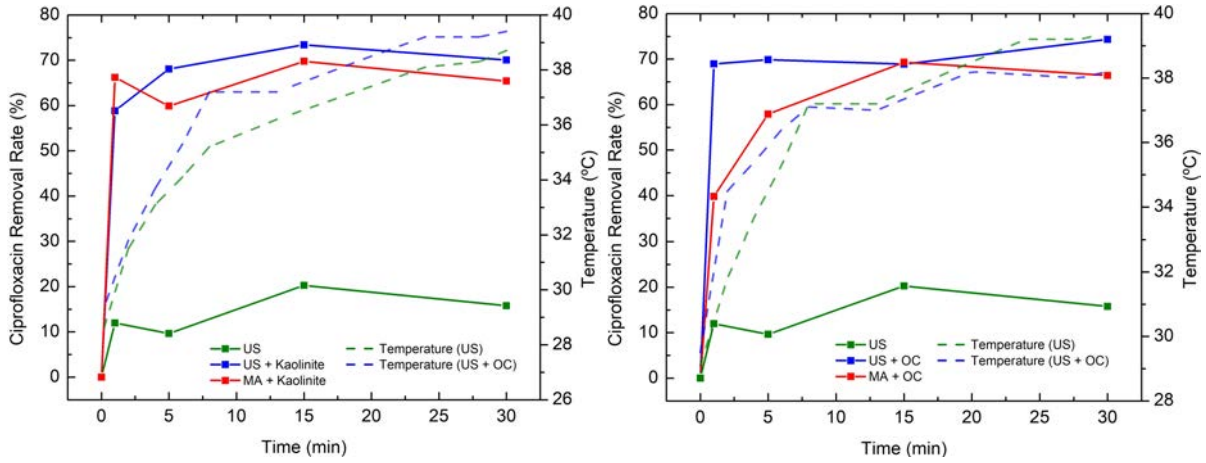

(a) (b)

Figure 4.31: Ciprofloxacine removal rate and it temperature during the exposition time, combining the ultrasound with (a) Kaolinite and with (b) Organic Compound.

In terms of utilizing ultrasound to enhance adsorption of heavy metals, we evaluated its combined use with Kaolinite and Organic Compounds. As depicted in Figure 4.32 (a), Kaolinite does not demonstrate effective behavior when combined with either Ultrasound or Mechanical Action. Specifically, Mechanical Action assistance only yielded a 12% removal rate after one minute, while US + Kaolinite achieved only 4%. Ultrasound did not lead to an improvement in the removal rate, and similar to mechanical action (MA + Kaolinite), the rate remained above 20%, indicating a low removal potential. The sudden exponential increase to 77% removal rate by US + Kaolinite after 15 minutes, following a period of constant stability around 5%, suggests a potential error in the process.

However, when combined with Organic Compounds, Ultrasound significantly enhances the removal rate, as shown in Figure 4.32 (b). After one minute, the removal reaches 82%, and it reaches a maximum of 86% after 5 minutes, maintaining this level thereafter. This implies that within just 5 minutes, the adsorbent reaches its maximum adsorbent rate, and after 1 minute, it has adsorbed 95% of its maximum capacity. Conversely, MA + OC only achieves a 19% Copper removal rate after one minute, and even after 30 minutes, the removal rate continues to increase, reaching up to two-thirds of the maximum adsorbent rate of US + OC.

In accordance with the findings detailed in the investigation conducted by Gupta et al. [88], the synergistic application of ultrasound treatment and adsorption demonstrates a pronounced enhancement in the adsorption kinetics. Notably, the accelerated rate of adsorption is evidenced by

achieving an 80% removal efficiency within the initial minute of treatment, ultimately culminating in the attainment of maximum removal efficiency after a 5-minute duration.

As observed in the case of Ciprofloxacin, the temperature follows a similar pattern as before. It does not appear to have a significant impact on Copper removal, as the temperature increase is not followed by an increase in pollutant concentration in the US + Kaolinite system. Moreover, in US + OC, the rapid increase in removal rate is not accompanied by a similar temperature increase.

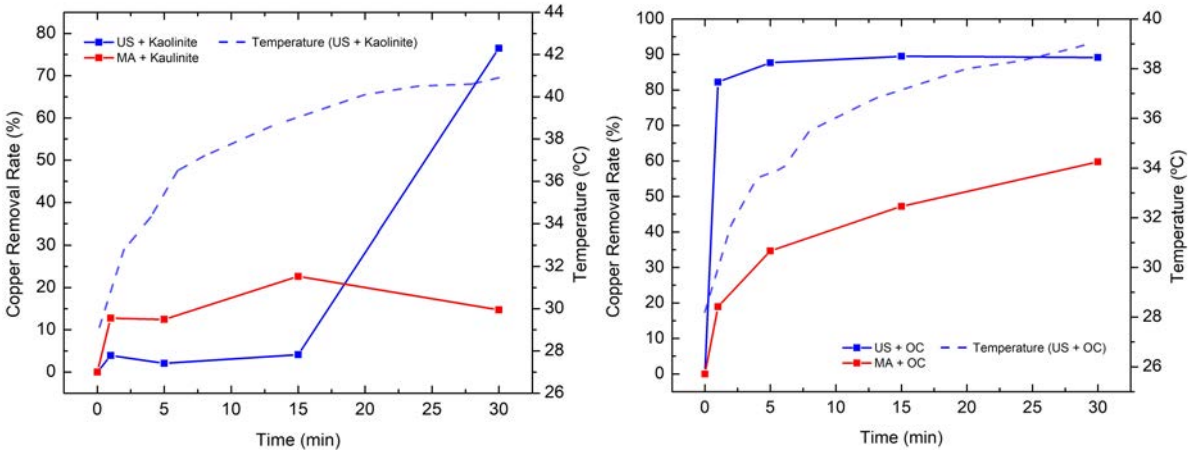

(a) (b)

Figure 4.32: Copper removal rate during the 30 minutes exposition time, combining the ultrasound with (a) Kaolinite and with (b) Organic Compound.

4.3 Insights from the Experimental Analysis

The experimental data obtained from the aforementioned tests provides valuable insights into the functionality of ultrasound in water and its associated impacts. Table 4.2 presents the key findings from the chamber sensorization. The study involved the evaluation of three sensors: Sensor 1, 2 and Sensor 3 in two different chamber positions. Calibration's equations were established, revealing distinct responses to applied forces. Sensor 2 and 3 exhibited signs of wear after exposure to cavitation, in contrast to Sensor 1 which remained unaffected.

Cavitation threshold assessments indicated that Sensor 1 and Sensor 3 share similar ranges, and the cavitation was detected. Notably, the cavitation threshold comparing Position 1 and 2, show different results. This offers a valuable insight into the cavitation pattern within the chamber, indicating that it is not a linear phenomenon over time and position.

The noise equations revealed consistent patterns for Sensor 1 and Sensor 3, providing information on

the levels of noise detected by these sensors, and the possible sources of it. The maximum peak cavitation force on the sensors reached 15.25 N at position 2 and 12.25 N at an alternate position.

Table 4.2: Insights provided by the data analysis from the chamber sensorization.

Parameters	**Sensor 1**	**Sensor 2**	**Sensor 3**
Equation of Calibration P1	$V = -0.28 + 0.04 \cdot F$	$V = -.20 + .04 \cdot F$	-
Wear after cavitation	No	Yes	Yes
Cavitation threshold - P1	[410$\pm$10 ; 500$\pm$10] W	-	[410$\pm$10 ; 500$\pm$10] W
Cavitation threshold - P2	[500$\pm$10 ; 600$\pm$10]	-	[600$\pm$10 ; 700$\pm$10]
Noise Equation	$F^n_{Peak} = 15,000 + f \cdot n$	-	$F^n_{Peak} = 15,000 + f \cdot n$
Maximum Impact Load - P1	-	-	12.25 N
Maximum Impact Load - P2	-	-	15.25 N

In Table 4.3, a comprehensive examination of experimental outcomes is presented, outlining the effects of Ultrasound on different water types. Both Ultra-Filtrated and Tap waters underwent Ultrasonic treatment, allowing for the measurement of pH and ORP values. Upon subjecting Ultra-Filtrated water to Ultrasound, ΔORP displayed a significant alteration, indicating a speed ratio of 2.52 at 18 seconds, subsequently reducing to 1. Similarly, ΔpH exhibited a change from 2.29 at 18 seconds to a steady state of 1.

Conversely, in the case of Tap water, data for ΔORP at 18 seconds was unattainable due to its inherently unpredictable behavior. Post the initial 18 seconds, Ultrasound application elicited a distinct variation as described by the function $-0.3 \cdot t - 1.9$, while the non-Ultrasound condition demonstrated negligible change. Meanwhile, ΔpH remained relatively stable, with an initial reading of 1.2 at 18 seconds persisting through subsequent time intervals.

Table 4.3: Insights provided by the data analysis from the application of Ultrasound on water.

Water Type	**Parameters**	**Acquisition time point**		**Notes**
		18 s	**]18;160] s**	
Ultra-Filtrated	ΔORP	2.52	1	-
	ΔpH	2.29	1	
Tap	ΔORP	-	$-0.3 \cdot t - 1.9$	Just US provokes alteration on ORP
	ΔpH	1.2	1	

Speed Comparison

In the context of adsorption enhanced by ultrasound, Table 4.4 offers a comparative analysis of pollutant removal efficiency achieved through ultrasound and mechanical action treatments using various adsorbents.

Initially, ultrasound exhibited a notable impact within the first minute of application, particularly in augmenting the adsorption of organic compounds. However, after this initial period, the results with Kaolinite were less compelling. Mechanical action only slightly suppressed the removal of CIP, resulting in a removal efficiency of only 60%. Nonetheless, it's worth noting that there was an observable increase in maximum removal with the application of ultrasound. As for the removal of Cu, the results indicated insufficient removal rates.

Turning our attention to the Organic Compound adsorbent, ultrasound treatment demonstrated impressive results, achieving a 69% removal of CIP within the first minute, surpassing the performance of Kaolinite. This superiority in removal efficiency extended to the maximum pollutant removal.

Regarding Cu removal, ultrasound combined with the Organic Compound adsorbent achieved remarkable rates, reaching 82% in the first minute and a maximum removal of 86%. In contrast, mechanical action yielded significantly lower rates of 19% and 58%.

It is important to highlight that ultrasound alone did not lead to any considerable alteration in removal efficiency.

Table 4.4: Insights provided by the data analysis from the aplication of Ultrasound with adsorption processes.

Adsorbent	**Pollutant**	**Ultrasound**		**Mechanical Action**	
		1 min	**Max removal**	**1 min**	**Max removal**
Kaolinite	CIP	60 %	72%	66%	69%
	Cu	3%	76%	12%	20%
Organic Compound	CIP	69%	74%	40%	69%
	Cu	82%	86%	19%	58%
-	CIP	12%	20%	-	-

Pollutant Removal

5. Performance Assessment on a Wastewater Treatment Plant

To evaluate the efficacy of the assisted ultrasound system in wastewater treatment, a comprehensive experimental study was conducted. This chapter outlines the experimental setup, methodology employed during the experiment, and the subsequent results obtained from the treatment process. Finally, the chapter concludes by presenting the key findings derived from the analysis of chemical and physical parameters.

5.1 Experimental Conditions and Setup

The experimental test took place at Serzedo's ETAR, wastewater treatment plant, and was collected treated wastewater from the secondary decanter. The equipment installed contemplated the ultrasound (ultrasonic device and respective chamber) and an air compressor in order to cool the transducer. To ensure that the humidity produced by the air compressor does not damage the transducer, it was used an air filter, Festo MS-LFR-B. Ultrasound management was made using the proper software that allows control every parameter from the ultrasonic wave.

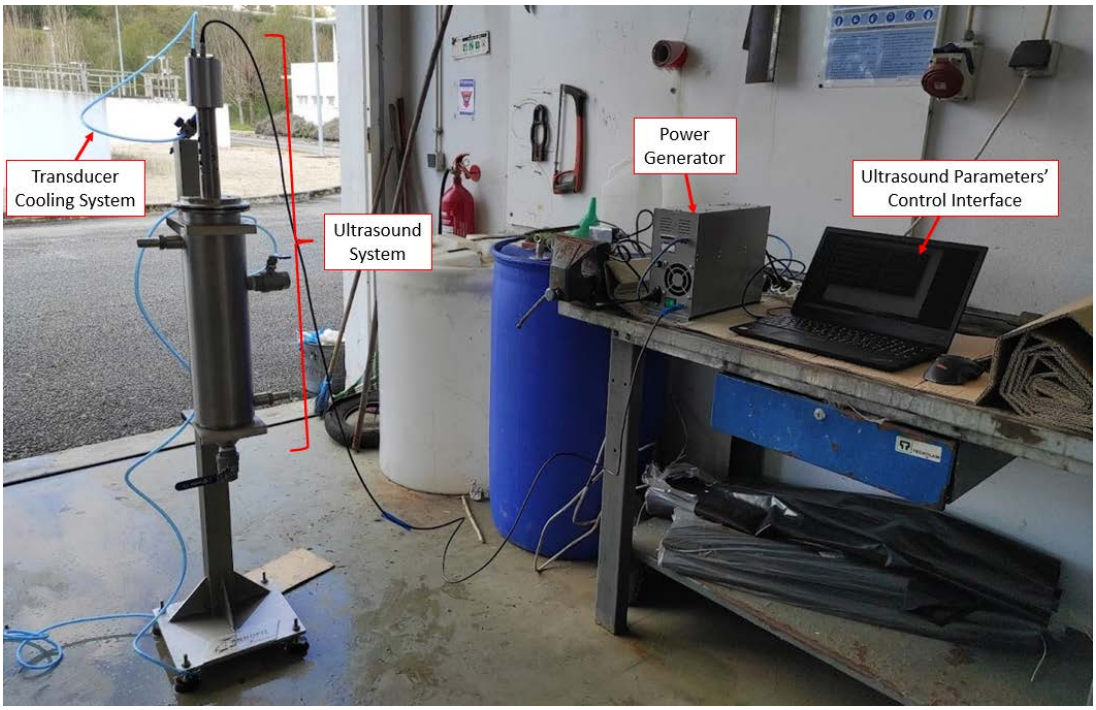

Figure 5.1: Experimental Setup for Ultrasound Cleaning in ETAR of Serzedo. The ultrasound unit is linked to both the power supply and a computer for system control. The transducer is cooled using compressed air supplied by an air compressor.

For evaluating the effects of the acoustic cavitation on the wastewater, it was defined 3 different

acoustic power and 5 different collection points. The different acoustic power values were 200 W, 400 W and 800 W. These are the variable conditions which allow evaluating the effect of the ultrasound in water at different power values. The collection points were 2, 5, 10 and 20 minutes, being that at zero time, it was measured the initial conditions. In order to evaluate the effects, were selected 12 different parameters: chemical oxygen demand, total Nitrogen, Phosphate, Ammonium, Nitrate Nitrogen, total suspended solids, pH, ORP, dissolved Oxygen, electrical conductivity, total dissolved solids and temperature.

The measurement was made in two different phases. A 500 mL beaker is used at each collection point, and subsequently, the collected sample is subjected to instant measurements using the multi-parameter HANNA HI98494. After the measurement of pH, ORP, dissolved Oxygen, electrical conductivity, TDS and temperature, was separated a 80 mL sample to posterior laboratory analysis of COD, total Nitrogen, PO_4^-, $N^-NH_4^+$ and $N^-NO_3^-$. The other 420 mL were put back in the chamber, and the time between the collection procedure and the restart of the acoustic cavitation was established as 1 minute.

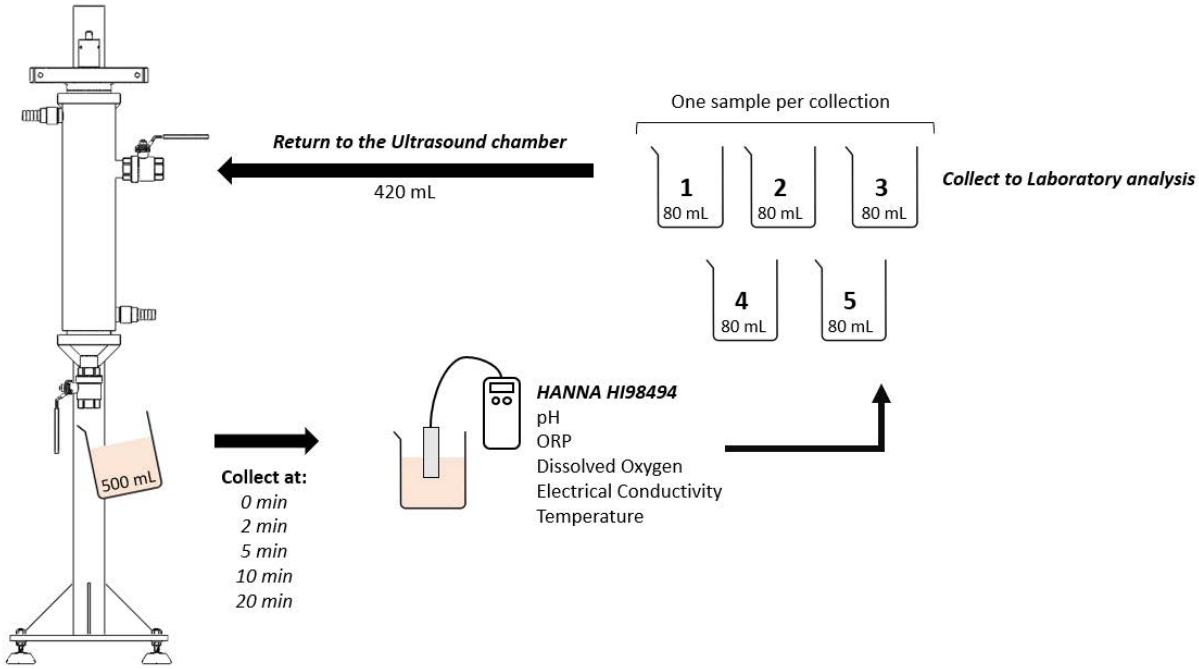

Figure 5.2: Experimental Study Scheme with Real Wastewater: A 500 mL sample is collected at 0, 2, 5, 10, and 20 minutes, followed by analysis using the HANNA HI98494. An 80 mL sample is extracted from the initial 500 mL for subsequent laboratory testing, while the remaining solution is returned to the chamber.

At the outset of the experimental tests, initial values for the wastewater were measured. The initial conditions for wastewater obtained from the secondary decantation process are presented in Table 5.1. It is imperative to thoroughly elucidate each initial sample corresponding to the respective power level. The

collected wastewater from the secondary decantation process comprised a 20 L sample.

Table 5.1: Physical and Chemical Parameters of Wastewater Before the Ultrasound Assisted Treatment with each Different Power.

	Power (W)				**Power (W)**		
Parameters	**200**	**400**	**800**	**Parameters**	**200**	**400**	**800**
CQO (mg/L)	25.9	13.1	46.8	*pH*	7.47	7.47	7.47
N_{total} *(mg/L)*	2.67	2.39	3.05	*ORP (mV)*	14.9	14.9	14.9
PO_4^- *(mg/L)*	2.3	2.21	2.24	*DO (mg/L)*	2.89	2.89	2.89
$N^-NH_4^+$ *(mg/L)*	0.593	0.642	0.632	*Conductivity* ($\mu S/cm$)	2445	2445	2445
$N^-NO_3^-$ *(mg/L)*	0.245	0.256	0	*TDS (mg/L)*	1222	1222	1222
SST (mg/L)	<7	<7	<7	*Temperature (°C)*	20.78	20.78	20.78

5.2 Analysis of Ultrasound Treatment Effects on Wastewater Parameters

Table 5.2 displays the variations in variables throughout the study, considering different acoustic intensities. Beginning with the variables that showed no variation, it is evident that Electrical Conductivity, Total Dissolved Solids, and Total Suspended Solids remained constant over time. The limited fluctuations in the latter two variables can be attributed to their low presence in the wastewater post-secondary decantation. Consequently, the subsequent analysis will concentrate on the remaining parameters.

Table 5.2: Physical and chemical parameters for the wastewater treated with ultrasound along the experimental test. Parameters at 0, 2, 5, 10 and 20 minutes.

						Power (W)									
Parameters			**200**					**400**					**800**		
Time (min)	**0**	**2**	**5**	**10**	**20**	**0**	**2**	**5**	**10**	**20**	**0**	**2**	**5**	**10**	**20**
COD (mg/L)	25.9	26.1	44.9	55.9	63.9	13.1	37	42.5	46.3	60.6	46.8	39.1	44.6	47.5	61.4
N_{total} *(mg/L)*	2.67	2.84	3.23	4.1	3.08	2.39	3.12	3.64	2.95	3.59	3.05	3.98	3.15	3.39	4.87
PO_4^- *(mg/L)*	2.3	2.25	2.29	2.24	2.31	2.21	3.21	2.77	2.81	4.13	2.24	2.25	2.3	2.31	2.4
$N^-NH_4^+$ *(mg/L)*	0.593	0.653	0.353	0.701	0.725	0.642	0.682	0.68	0.687	0.717	0.632	0.639	0.631	0.628	0.662
$N^-NO_3^-$ *(mg/L)*	0.245	0.144	0.208	0.193	0.281	0.256	0.196	0.223	0.233	0.254	0	0.246	0.181	0.206	0.196
pH	7.47	7.04	7.42	7.52	7.44	7.47	7.57	7.53	7.49	7.32	7.47	7.65	7.58	7.47	7.42
ORP (mg/L)	14.9	86	56.4	41.5	27.4	14.9	25.9	33.5	27.4	16.9	14.9	20.9	22.6	19.5	11.1
DO	2.89	4.99	4.29	4.23	3.76	2.89	4.53	4.24	4.04	3.65	2.89	4.8	4.55	4.25	3.88
Conductivity ($\mu S/cm$)	2445	2403	2452	2482	2543	2445	2451	2471	2497	2544	2445	2440	2450	2494	2537
TDS (mg/L)	1222	1205	1226	1242	1272	1222	1228	1235	1249	1272	1222	1220	1225	1247	1270
Temperature (°C)	20.78	22.2	26.04	31.65	41.09	20.78	24.64	28.41	34	43.42	20.78	24.4	28.45	33.77	43.48

Regarding pH and ORP, which serve as indicators of chemical reactions, Figure 5.3 illustrates distinct behaviours in the initial two minutes. During this period, ORP experiences a rapid increase, while pH exhibits the opposite trend. Subsequently, between 2 and 5 minutes, a reversal of reactions is observed: pH increases rapidly, while ORP decreases, albeit at a slower rate. This trend of ORP decline persists until the conclusion of the experiments, mirroring the pH's behaviour but in the opposite direction. Ultimately, after 20 minutes, the values return to their initial states.

In contrast, Figure 5.3 demonstrates that Temperature shows a nearly linear increase over the 20-minute duration. Conversely, Dissolved Oxygen undergoes relatively minor changes. Similar to pH and ORP, it appears that the cavitation effect is most pronounced within the initial 2 minutes, after which the values gradually revert back to their initial states.

The rise in pH indicates that ultrasound generates more hydroxide ions, resulting in fewer hydrogen ions and an abundance of hydroxide ions. This shift leads to an environment with higher levels of oxidizing species, augmenting the solution's oxidant potential. However, the ORP variation suggests a decreased likelihood of electron transfer reactions occurring and a reduced probability of oxidation reactions taking place.

After the initial 2 minutes, the capacity to generate additional hydroxide ions diminishes, leading to a pH decrease followed by an ORP increase. The elevated ORP signifies that the solution gains a heightened ability to accept electrons. With the reduction of hydroxide ions, the reactive species become more available to undergo oxidation, accepting electrons. This behaviour implies that ultrasound exerts a substantial effect initially but lacks the sustained power to mineralize additional pollutant species [167].

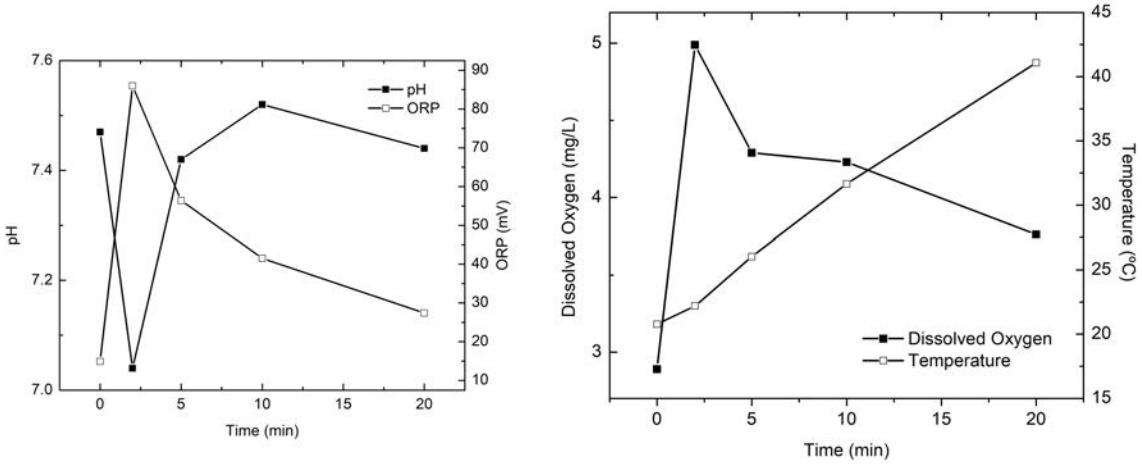

(a) (b)

Figure 5.3: Variation of parameters that are indicators of chemical reactions on wastewater treatment with application of a acoustic power of 200 W. (a) pH and ORP (b) Temperature and Dissolved Oxygen.

In reference to COD removal, as depicted in Figure 5.4, there is no discernible reduction; rather, an increase in COD concentration is observed. In the initial two minutes, the value remains stable. However, from minute 2 to 10, there is a notable and steep incline. In the final 10 minutes, this rate of increase decreases, resulting in a flatter trajectory compared to the preceding period. Over the course of the first to last minute, the COD concentration rises from 26 mg/L to 64 mg/L.

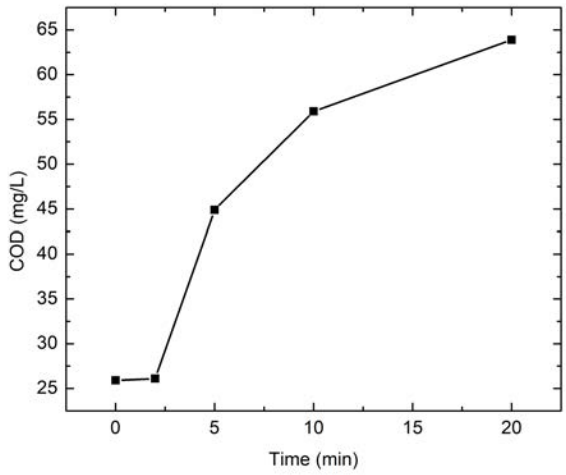

Figure 5.4: COD removal with application of a acoustic power of 200 W.

Focusing on other chemical parameters, Ammonium Nitrogen ($N^{-}NH_4^{+}$) exhibits an initial increase within the first 2 minutes and between the tenth and last minute, as shown in Figure 5.5 (a). However, after 5 minutes, the concentration experiences an abrupt fluctuation, suggesting a potential error in this data point. Generally, the Ammonium Nitrogen concentration shows a slight overall increase, while Nitrate Nitrogen ($N^{-}NO_3^{-}$) displays subtle fluctuations over time, ultimately returning to its initial value.

The rise in Ammonium Nitrogen may be correlated with a decrease in Ammonia levels. This increase could be attributed to the chemical conversion of Ammonia to Ammonium, a less toxic compound. Additionally, the elevated Ammonium Nitrate levels might be linked to an intensified decomposition of organic matter.

As for Nitrate Nitrogen, the minimal variation may be attributed to low levels of dissolved oxygen. In such circumstances, the reduced concentration diminishes nitrification efficiency, resulting in a less effective biological nutrient removal (BNR) process and consequently higher ammonium concentrations in the effluent. Notably, Dissolved Oxygen, Figure 5.3, shows no significant alteration throughout the experiment, aligning with the stable trends observed in both Ammonium Nitrate and Nitrate Nitrogen concentrations.

Comparing Total Nitrogen and Phosphate, Phosphate demonstrates a linear increase from 2.7 mg/L to 4.1 mg/L over 10 minutes, followed by a subsequent decrease of 3 mg/L. In contrast, akin to Nitrate Nitrogen, Phosphate maintains a consistent value throughout the entire experiment, exhibiting no substantial variations, Figure 5.5.

The increase in Total Nitrogen could be attributed to various factors. This rise might be linked to the incomplete oxidation of nitrogen compounds, or the transformation of nitrogen species into other forms.

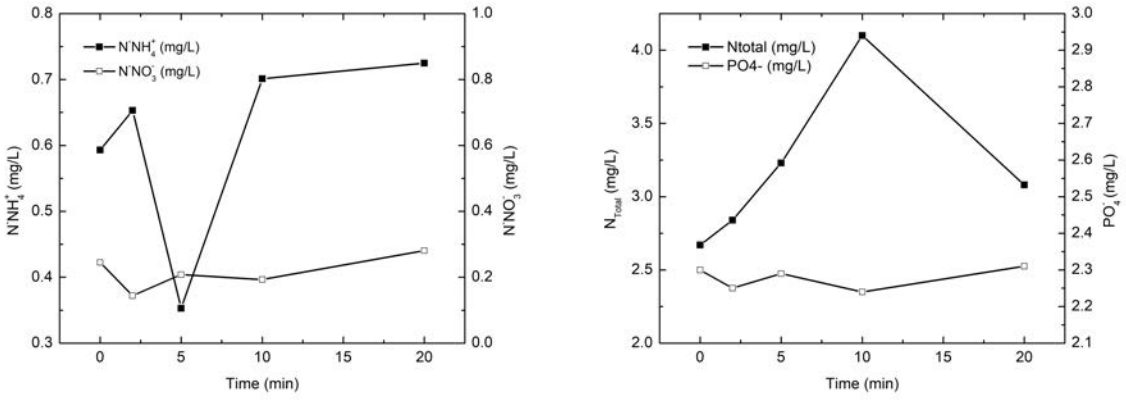

(a) (b)

Figure 5.5: Variation of parameters that are indicators of chemical reactions and biological and organic reaction along wastewater treatment with application of a acoustic power of 200 W. (a) $N^-NH_4^-$ and $N^-NO_3^-$ (b) N_{total} and PO_4^-.

With an increase in acoustic power to 400 W, both pH and ORP exhibit different behaviours compared to the 200 W setting. In contrast to the previous observation, where pH and ORP consistently changed in opposite directions, here both parameters follow similar patterns. ORP increases until the fifth minute, while pH peaks at the second minute, after which both values decline. In this case, it appears that ultrasound exerts a more prolonged influence, as pH decreases to levels below the initial ones. However, ORP tends to stabilize back to the initial values after the initial increase (see Figure 5.6).

This combined increase and subsequent decrease suggests that, at 400 W, the solution is conducive to oxidation processes within the initial two minutes. However, once the cavitation ceases to promote the formation of more hydroxide ions, the system's oxidation potential substantially decreases.

Temperature continues its linear increase, mirroring the trend observed at 200 W. Dissolved Oxygen, on the other hand, exhibits the same initial increase in the first two minutes followed by a decline. Comparing the results to those at 200 W (see Figure 5.5 and Figure 5.6), it is evident that Dissolved Oxygen increases between 0 and 2 minutes and then subsequently decreases. Elevating the ultrasound power intensity

further accentuates this trend, leading to a higher concentration of Dissolved Oxygen at its peak.

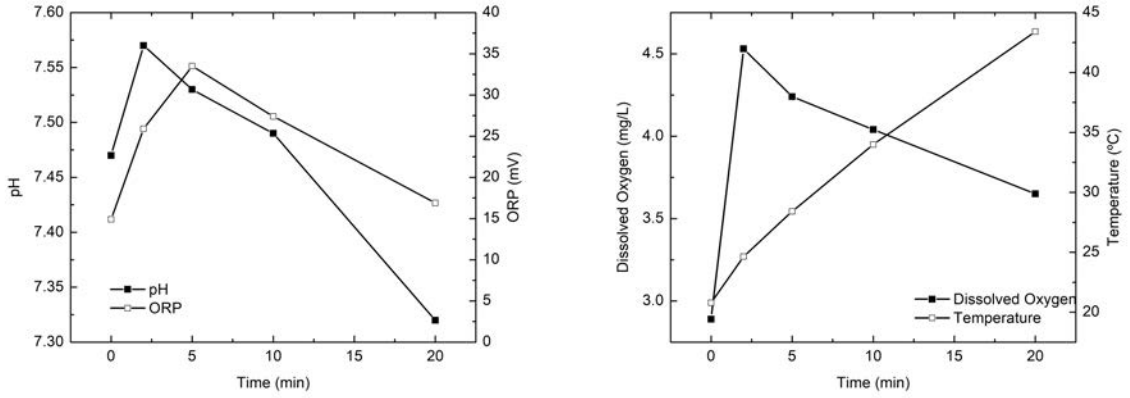

(a) (b)

Figure 5.6: Variation of parameters that are indicators of chemical reactions on wastewater treatment with application of a acoustic power of 400 W. (a) pH and ORP (b) Temperature and Dissolved Oxygen.

In terms of COD removal, there is no initial stabilization as observed at 200 W. Instead, there is a notable surge within the first two minutes, marking the most significant increase during this period. However, this increase continues steadily, displaying a linear progression after the second minute. From the initial moment to the conclusion, the COD concentration rises from 12 mg/L to 60 mg/L. This trajectory mirrors the behaviour observed at 200 W, as depicted in Figure 5.7.

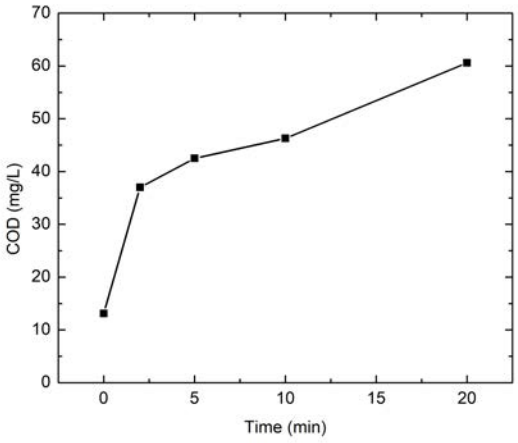

Figure 5.7: COD removal with application of a acoustic power of 400 W.

Similar to the effects observed at 200 W ultrasound power, there is a notable increase in Ammonium concentration within the first two seconds, while for Nitrate Nitrogen, the opposite effect occurs, resulting

in a decrease. This trend continues after the initial two minutes, with Ammonium concentration steadily increasing, albeit at a slower rate, and Nitrate Nitrogen returning to its initial value. Comparing the variations in these parameters between 200 W and 400 W applications (Figure 5.5 (a) and Figure 5.5 (a)), it's evident that the overall behaviour is similar. Ammonium experiences notable growth, particularly in the initial two seconds. As for Nitrate, there's a significant decrease in the first two seconds followed by a subsequent increase until it reaches the initial value.

Turning to Total Nitrogen and Phosphate, both exhibit similar patterns, showing significant increases in the initial two minutes (Figure 5.8 (b)). Comparing this to Figure 5.5 (b), it's apparent that at 400 W acoustic power, the peak in Total Nitrogen occurs earlier, shifting from 10 minutes to 5 minutes, and also induces an increase in Phosphate, which was not observed at 200 W.

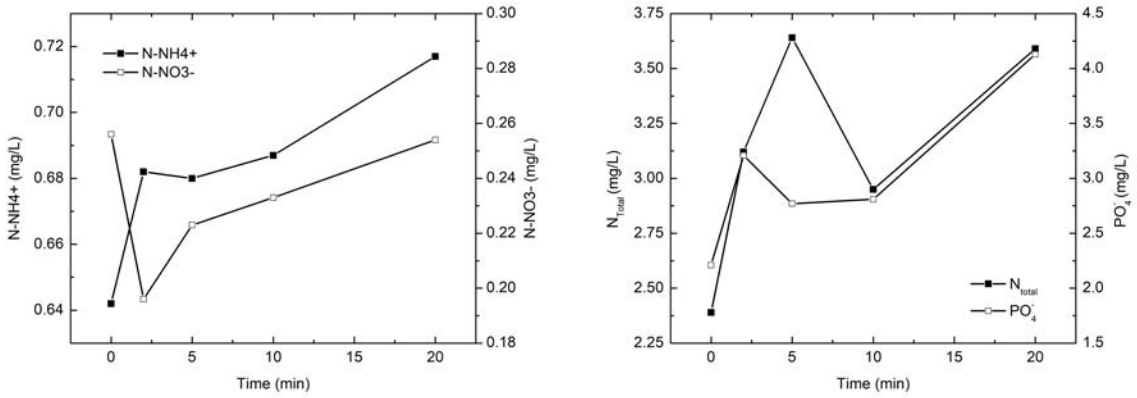

(a) (b)

Figure 5.8: Variation of parameters that are indicators of chemical reactions and biological and organic reaction along wastewater treatment with application of a acoustic power of 400 W. (a) $N^-NH_4^-$ and $N^-NO_3^-$ (b) N_{total} and PO_4^-.

Similar to the trends observed in Figure 5.6 (a), both pH and ORP exhibit very similar behaviours over time for acoustic powers of 400 W and 800 W, as shown in Figure 5.9 (a). At 800 W power, both pH and ORP values experience significant increases in the initial two minutes. However, while ORP reaches its maximum value at 5 minutes and then decreases, pH starts decreasing after the second minute. When compared with the other power levels, it's notable that at 800 W, the ORP value experiences a more pronounced decrease from the initial value.

Temperature maintains the anticipated behaviour as seen previously, and Dissolved Oxygen concentration confirms the established pattern of an initial increase in the first two minutes, followed by a subsequent decrease. In this case, the final value still remains above the initial one (Figure 5.9 (b)).

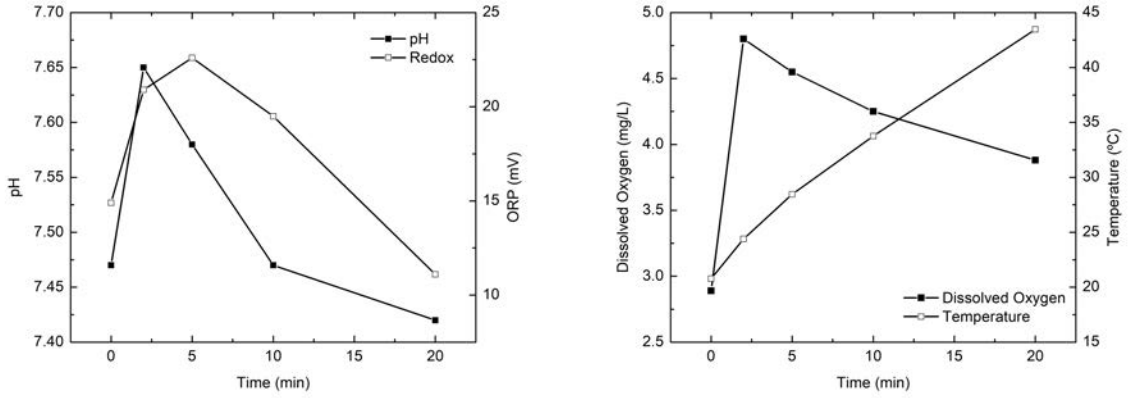

(a) (b)

Figure 5.9: Variation of parameters that are indicators of chemical reactions on wastewater treatment with application of a acoustic power of 800 W. (a) pH and ORP (b) Temperature and Dissolved Oxygen.

In contrast to the previous COD concentration observations, at 800 W of acoustic power, there is a decrease in COD concentration in the initial two minutes. Subsequently, there is a gradual increase until the 10-minute mark. From that point on, the increase becomes more pronounced, extending until the conclusion of the experiment (see Figure 5.10).

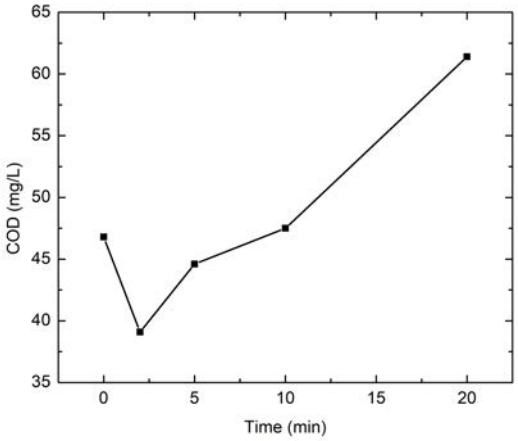

Figure 5.10: COD removal with application of a acoustic power of 800 W.

At 800 W, Ammonia exhibits a behaviour similar to that demonstrated at an intensity of 400 W. It's evident that there is a rapid increase in the first minute, followed by a slight decrease, and then another swift increase (Figure 5.11). However, the pattern for Nitrate Nitrogen is opposite. Nitrate Nitrogen experiences a substantial increase in the first two seconds, after which its concentration remains constant over time.

Similar to the observations at 200 W and 400 W power levels, the peak of Total Nitrogen occurs earlier than in the other cases, manifesting in the second minute. Following this peak, the behaviour decreases before increasing again. On the other hand, in line with the concentration of Phosphorous for 200 W and 400 W, ultrasound action leads to an increase in this chemical concentration (see Figure 5.11).

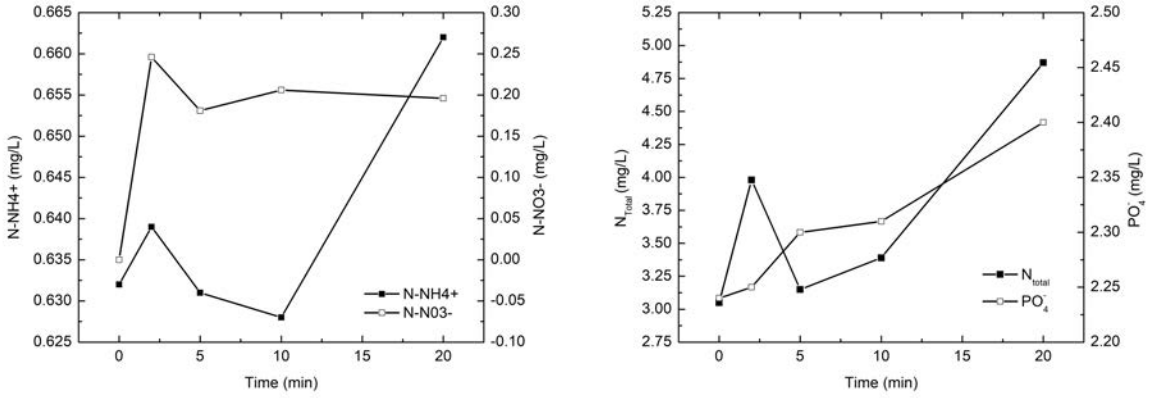

(a) (b)

Figure 5.11: Variation of parameters that are indicators of chemical reactions and biological and organic reaction along wastewater treatment with application of a acoustic power of 800 W. (a) $N^-NH_4^-$ and $N^-NO_3^-$ (b) N_{total} and PO_4^-.

It is evident that most significant modifications occur within the initial two minutes. During this time frame, chemical parameters experience notable increases or decreases. Subsequently, there is a tendency for the values to revert back to their initial states. This suggests that the primary impact of acoustic cavitation occurs in the initial minutes, after which the effects begin to dissipate.

In terms of COD concentration, two distinct behaviours are observed. At 200 W and 800 W, the concentration stabilizes or decreases in the first two minutes, followed by a subsequent increase. However, this trend is not observed at 400 W, where COD increases rapidly in the first two minutes.

These results deviate from what is typically expected based on the literature [94–96]. However, they could be related to phenomena mentioned in the same references. For instance, in the wastewater treatment of pharmaceutical wastewater, a maximum removal efficiency of 8% at 30 minutes was reported with ultrasound at an amplitude of 20% and a solution pH of 5. In another study on the tertiary treatment of treated municipal wastewater, a maximum COD removal of 35% was achieved after 30 minutes. Throughout the process, no negative removal rates were observed. Nevertheless, upon analysing the removal of organic compounds, it was noted that the concentration of two organic components increased. Similar observations were made by other authors, suggesting that this

phenomenon is attributed to the presence of organic pollutants adsorbed on suspended solids. The physical action of ultrasound induces the size reduction of solids, releasing absorbed pollutants. This could be the mechanism responsible for the increase in COD during ultrasound application.

The varying responses across different ultrasound powers may be attributed to the ultrasound's incapacity to effectively degrade and mineralize the pollutants [167]. The variation in COD across different power levels suggest two mechanisms. The first involves degradation induced by ultrasound, while the second involves the separation of organic compounds from the solids present in water. In the initial moments, ultrasound possesses sufficient power to degrade and mineralize organic compounds. At 200 W, the ultrasound lacks the power to entirely counteract the emission of organic compounds from solids, resulting in an equilibrium between the two phenomena. However, at 800 W, when ultrasound has more power, the COD concentration decreases. Subsequently, as it reaches the threshold for organic compound degradation and mineralization, the COD starts to increase again.

At 400 W, no degradation occurs, which suggest that ultrasound has minimal effect at this power level, or the wastewater sample contains more organic pollutants associated with solids. Comparing the variations in Figure 5.12, it is apparent that the wastewater solution at 400 W has the lowest COD concentration, implying that organic compounds may be more prevalent on the walls of solids.

Another piece of evidence supporting this is that even though the experiments start with different initial COD concentrations, the final values converge to similar levels. This indicates that ultrasound increases the separation between organic compounds and the walls of solids, leading to an increase in isolated organic compounds in the water.

Another noteworthy phenomenon that may significantly influence the observed effects is the concurrent increase in temperature during cavitation. As illustrated in Figure 5.3 (a), Figure 5.6 (b), and Figure 5.9 (c), the temperature exhibits a rising trend over time. Bagal et al. [10] have reported that the cavitation phenomenon is particularly favored within a temperature range of 25-30 °C.

It is essential to consider the impact of temperature on the overall process, as several studies, including those by Bagal et *al.* [10], highlight that the efficiency of pollutant degradation tends to decrease with increasing temperatures. Certain investigations emphasize that pollutant degradation is more efficient at temperatures below 30 °C than at higher temperatures [18, 126, 129]. Consequently, the temperature variation could potentially play a crucial role in the removal rate, with higher temperatures potentially contributing to a reduction in overall efficiency.

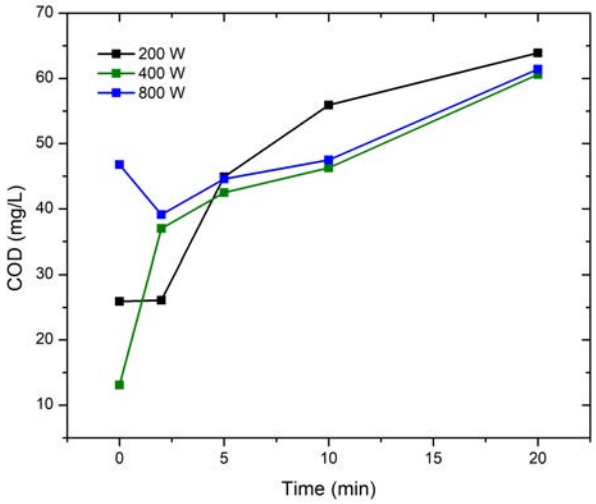

Figure 5.12: COD removal comparison for the three powers of 200 W, 400 W and 800 W.

6. Conclusions

6.1 Piezoelectric Sensor for Cavitation Characterization

The sensors developed in this dissertation successfully met the initially outlined objectives. Alongside their physical development, a real-time monitoring program was created to collect and process cavitation data.

The piezoelectric sensors exhibited low resistance to cavitation when not used with a protective resin layer. In this case, one of the unprotected piezoelectrics was damaged, rendering it inoperative. On the other hand, the piezoelectric with the epoxy layer showed no associated damage. However, the same studies demonstrate that the 0.2mm layer hinders the ultrasound from having similar sensitivity to the others. During sensor calibration, it was confirmed that the presence of this thickness of layer limits sensitivity in readings, preventing its calibration.

Sensorization of the ultrasonic chamber allowed the conclusion that acoustic cavitation near the sensor occurred around 500 W. However, it was also verified that this value could vary depending on the sensor's position. This aligns with what is visually observed, where it is possible to identify that cavitation and acoustic streaming vary along the acoustic radiator and over time.

Monitoring of acoustic cavitation was performed through both subharmonic readings and FFT graph readings of the data acquired by the sensor. Both methods allowed for establishing a relationship between the increase in power and the onset and increase of acoustic cavitation. The existence of this phenomenon ensures that the current dimensions of the ultrasound equipment are in accordance with what is expected.

In addition to characterization through harmonic readings, a relation was also established between the potential difference generated by the piezoelectrics and the force to which the sensor is subjected. In this case, the sensors were able to provide a reading of the force resulting from cavitation.

During the development of this sensor, one of the main questions was whether modifying its geometric and physical properties would significantly influence the resonance frequency. In this case, the resonance frequency after final geometry and the placement of the epoxy protective layer revealed that there are no significant differences in these. However, it is important to note that in the second case, there is a new resonance above the natural frequency. However, as it does not imply major differences in the final reading, it can be considered that in this case, modifying the original sensor does not entail considerable consequences.

Regarding the immersion level of the ultrasound in water, the results show that the maximum immersion limit should be, at most, below 200 mm. Above this value, the resonance frequency varies considerably.

6.2 Assessment of Impacts of Ultrasound on Wastewaterw

Ultrasound proves to accelerate chemical reactions and bolstering radical presence, including H_2O_2 and H^+. In the initial stages, its effects are notably pronounced. For instance, in ultra-filtered water, within 20 seconds, ultrasound leads to a 1.5-fold increase in ORP and a 2.29-fold surge in pH compared to no action. In tap water, ultrasound causes a continuous ORP reduction, while without action, it remains unchanged. These results affirm ultrasound's potential in expediting oxidative processes, particularly in the early stages.

In adsorption processes, ultrasound showcasing notable effectiveness. Within 1 minute, ultrasound matches the Ciprofloxacin adsorption capacity with Kaolinite achieved by mechanical action. However, with Organic Compound, ultrasound demonstrates a removal rate 1.75 times faster. For Copper removal, ultrasound, applied with kaolinite, yields similar results, but with the Organic Compound, it boasts a removal rate 4.3 times higher. This acceleration is confined to the first minute, where ultrasound propels adsorption to its limit. This highlights ultrasound's significant potential, especially in initial stages.

Results pertaining to adsorption also suggest that ultrasound amplifies the adsorption rate of an adsorbent. Post-stabilization, it is evident that ultrasound's maximum adsorption value surpasses that achieved through mechanical action. The combined effect of accelerated adsorptive processes and the potential increase in maximum adsorption capacity underscores ultrasound's substantial promise.

When applied to wastewater, ultrasound exerts notable influence across various phases, with the most significant impact occurring initially. Generally, ultrasound's significance wanes after the initial action, as parameters revert to their baseline values. This observation underscores ultrasound's potential in driving mechanical actions that trigger chemical reactions.

Notably, ultrasound's application leads to the disintegration of organic substances previously adhered to solids. This holds immense potential, as the separation of organic compounds from solids paves the way for easier mineralization. This phenomenon is closely tied to the variation in COD during testing. Moreover, higher applied power leads to greater initial degradation of organic compounds in the solution, after which they begin to increase. Beyond the cavitation threshold (identified at 500 W), ultrasound significantly impacts COD reduction, aligning with expectations.

In assessing other parameters like temperature, it is evident that its influence is minimal, both in laboratory tests and within WWTP contexts. However, temperature elevation does impact ultrasound efficiency, warranting efficient cooling measures for continuous operation.

6.3 Future Works

Through the analysis of the obtained results, key areas for future equipment development have come to light. Starting with sensors, an essential step is to delve into the study of the minimum protective layer required. This layer aims to shield the sensor from cavitation while ensuring it remains sensitive enough for accurate cavitation characterization.

Having validated the functionality of the sensors, it is now imperative to explore the maximum feasible size for the chamber. This investigation aims to investigate the maximum possible diameter where still exist cavitation. In connection with piezoelectric sensors, the utilization of signal acquisition equipment with higher resolution is recommended for future endeavours. The existing equipment falls short in reading interferences below 12 μs, hindering proper sensor calibration and comprehension of bubble effects. This necessity is underscored by the proven requirement for comprehensive chamber monitoring, necessitating multiple sensors and a higher sample acquisition rate.

Following chamber sensorization, the adoption of smaller sensors becomes imperative for seamless accommodation within the chamber. This undertaking involves an exploration of new sensors, compact yet operating on a similar principle. At the same time it is important to develop a temperature monitoring system to regulate the temperature inside the chamber. While current equipment has cooling channels, continuous temperature monitoring ensures water flow for cooling is initiated only when necessary.

Regarding to cavitation impact on water, it is necessary to develop an incremental introduction of diverse solid and chemical substances is essential for evaluating Ultrasound's impact on these elements.

The present work presents two potential paths for equipment evolution. The first path integrates ultrasound for pollutant adsorption acceleration and optimization. This necessitates tests to validate ultrasound's efficacy in the initial minute and determine the minimum exposure time for maximum adsorption. Additionally, exploring new adsorbents and assessing their adsorption capacities, with and without ultrasound application, is vital.

Conversely, the alternative path envisions equipment tailored to water treatment, combining ultrasound with other AOPs. Given ultrasound's limitations in fully eradicating organic pollutants, coupling it with processes like Ozone, Fenton, and H_2O_2 for enhanced mineralization is proposed. Understanding the requisite minimum concentrations, actual benefits of ultrasound use, and the distribution of degraded pollutants post-mineralization are paramount for this equipment's development. This insight will guide subsequent steps and procedures for degraded pollutant elimination.

References

[1] UN, *The human right to water and sanitation*. New York: UN, 2010. [Online]. Available: http://digitallibrary.un.org/record/687002

[2] M. A. Hanjra and M. E. Qureshi, "Global water crisis and future food security in an era of climate change," *Food Policy*, vol. 35, no. 5, pp. 365–377, 2010.

[3] U. W. W. A. Programme, Ed., *The United Nations World Water Development Report 2023: partnerships and cooperation for water*. UN, 2023.

[4] E. E. Agency, *Industrial waste water treatment : pressures on Europe's environment*. Publications Office, 2019.

[5] J. Rockström, M. Falkenmark, L. Karlberg, H. Hoff, S. Rost, and D. Gerten, "Future water availability for global food production: The potential of green water for increasing resilience to global change," *Water Resources Research*, vol. 45, no. 7, 7 2009.

[6] P. R. Gogate and A. B. Pandit, "A review of imperative technologies for wastewater treatment i: oxidation technologies at ambient conditions," *Advances in environmental research*, vol. 8, no. 3-4, pp. 501–551, 2004.

[7] A. L. Camargo-Perea, A. Rubio-Clemente, and G. A. Peñuela, "Use of ultrasound as an advanced oxidation process for the degradation of emerging pollutants in water," *Water*, vol. 12, no. 4, p. 1068, 4 2020.

[8] A. Gogoi, P. Mazumder, V. K. Tyagi, G. T. Chaminda, A. K. An, and M. Kumar, "Occurrence and fate of emerging contaminants in water environment: a review," *Groundwater for Sustainable Development*, vol. 6, pp. 169–180, 2018.

[9] D. Rozman, Z. Hrkal, M. Váňa, J. Vymazal, and Z. Boukalová, "Occurrence of pharmaceuticals in wastewater and their interaction with shallow aquifers: a case study of horní beřkovice, czech republic," *Water*, vol. 9, no. 3, p. 218, 2017.

[10] M. V. Bagal and P. R. Gogate, "Wastewater treatment using hybrid treatment schemes based on cavitation and fenton chemistry: A review," *Ultrasonics Sonochemistry*, vol. 21, no. 1, pp. 1–14, 2014.

[11] J. H. Gibson, D. H. N. Yong, R. R. Farnood, and P. Seto, "A literature review of ultrasound technology and its application in wastewater disinfection," *Water Quality Research Journal*, vol. 43, no. 1, pp. 23–35, 2 2008.

[12] R. Patidar and V. C. Srivastava, "Ultrasound-assisted enhanced electroxidation for mineralization of persistent organic pollutants: A review of electrodes, reactor configurations and kinetics," *Critical Reviews in Environmental Science and Technology*, vol. 51, no. 15, pp. 1667–1701, 2021.

[13] A. Hassani, M. Malhotra, A. V. Karim, S. Krishnan, and P. V. Nidheesh, "Recent progress on ultrasound-assisted electrochemical processes: A review on mechanism, reactor strategies, and applications for wastewater treatment," *Environmental Research*, vol. 205, 4 2022.

[14] X. Zhang, X. Kang, J. Wu, Q. Yang, Y. Zhang, J. He, C. Zheng, Y. Yang, and Z. Ye, "Sulfur-doped mesoporous ferric oxide used for effectively activating h2o2 to degrade moxifloxacin," *Journal of Environmental Chemical Engineering*, vol. 11, no. 2, 4 2023.

[15] V. Naddeo, V. Belgiorno, and R. M. Napoli, "Behaviour of natural organic mater during ultrasonic irradiation," *Desalination*, vol. 210, no. 1-3, pp. 175–182, 6 2007.

[16] M. Smol, P. Marcinek, D. Szołdrowska, M. Preisner, J. Kruopienė, M. Klavins, R. Ozola-Davidane, L. Appels, M. Horttanainen, I. Deviatkin, J. Havukainen, L. Pietrzkiewicz, A. Loch-Dzido, K. Roosalu, E. Lobos-Moysa, E. Kudlek, F. Ashour, H. Elsersy, N. Salam, and M. Dudziak, *Water and Sewage in the Circular Economy Model*. Publishing House Mineral and Energy Economy Research Institute, 09 2022.

[17] T. J. Mason, E. Joyce, S. S. Phull, and J. P. Lorimer, "Potential uses of ultrasound in the biological decontamination of water," *Ultrasonics Sonochemistry*, vol. 10, no. 6, pp. 319–323, 2003.

[18] P. R. Gogate and G. S. Bhosale, "Comparison of effectiveness of acoustic and hydrodynamic cavitation in combined treatment schemes for degradation of dye wastewaters," *Chemical Engineering and Processing: Process Intensification*, vol. 71, pp. 59–69, 2013, process Intensification by Alternative Energy Forms and Transfer Mechanisms.

[19] R. de Portugal, "Decreto-lei n.o 152/97, de 19 de junho," 1997.

[20] ——, "Decreto-lei n.o 236/98, de 1 de agosto," 1998.

[21] H. Monte, M. Santos, A. Barreiros, and A. Albuquerque, *Tratamento de Águas Residuais*, E. R. dos Serviços de Águas e Resíduos, I. S. de Engenharia de Lisboa, and U. da Beira Interior, Eds. ISEL, 12 2016.

[22] C. Simões, I. Rosmaninho, and A. G. Henriques, *Guia para a Avaliação de Impacte Ambiental de Estações de Tratamento de Águas Residuais*, 1st ed., A. P. do Ambiente, Ed. Agência Portuguesa do Ambiente, 2008.

[23] G. Tchobanoglous, F. Burton, H. Stensel, and I. Metcalf & Eddy, *Wastewater Engineering: Treatment and Reuse*, ser. McGraw-Hill higher education. McGraw-Hill Education, 2003.

[24] A. Sonune and R. Ghate, "Developments in wastewater treatment methods," *Desalination*, vol. 167, pp. 55–63, 8 2004.

[25] C. E. Boyd, "Suspended solids, color, turbidity, and light," *Water Quality*, pp. 119–133, 2020.

[26] W. B. Jensen, "The symbol for ph," *Journal of Chemical Education*, vol. 81, no. 1, p. 21, 2004.

[27] USGS, "Water science school: ph and water," https://www.usgs.gov/special-topics/water-science-school/science/ph-and-water, accessed: October 01, 2023.

[28] T. V. Suslow, *Oxidation-Reduction Potential (ORP) for Water Disinfection Monitoring, Control, and Documentation*. University of California, Agriculture and Natural Resources, 9 2004.

[29] M. M. Walczak, D. A. Dryer, D. D. Jacobson, M. G. Foss, and N. T. Flynn, "ph dependent redox couple: An illustration of the nernst equation," *Journal of chemical education*, vol. 74, no. 10, p. 1195, 1997.

[30] A.-S. Feiner and A. McEvoy, "The nernst equation," *Journal of chemical education*, vol. 71, no. 6, p. 493, 1994.

[31] S. Nasser and H. Al-Hussainin, "The oxidation reduction potential distribution along diyala river within baghdad city dye removal from wastewater view project watersheds assessment view project," *Mesopotamia Environmental Journal*, 2016.

[32] R. B. Geerdink, R. Sebastiaan van den Hurk, and O. J. Epema, "Chemical oxygen demand: Historical perspectives and future challenges," *Analytica Chimica Acta*, vol. 961, pp. 1–11, 2017.

[33] I. Bisutti, I. Hilke, and M. Raessler, "Determination of total organic carbon – an overview of current methods," *TrAC Trends in Analytical Chemistry*, vol. 23, no. 10, pp. 716–726, 2004.

[34] M. Vázquez-López, L. E. Amabilis-Sosa, G. E. Moeller-Chávez, A. Roé-Sosa, P. Neumann, and G. Vidal, "Evaluation of the ultrasound effect on treated municipal wastewater," *Environmental Technology*, vol. 40, no. 27, pp. 3568–3577, 12 2019.

[35] T. Deblonde, C. Cossu-Leguille, and P. Hartemann, "Emerging pollutants in wastewater: A review of the literature," *International Journal of Hygiene and Environmental Health*, vol. 214, no. 6, pp. 442–448, 11 2011.

[36] . Martínez-Orgániz, J. E. Becerril-Bravo, and A. Navarro-Frómeta, "Pollutants of emerging concern in tourist beaches of guerrero, mexico: A first approach to sources." *Marine Pollution Bulletin*, 2023.

[37] C. Awuchi and I. Amagwula, "Environmental pollutants and contaminants of emerging concern: An african perspective," *Journal La Lifesci*, vol. 2, no. 3, pp. 39–50, Sep. 2021.

[38] K. Y. Bell, M. J. Wells, K. A. Traexler, M.-L. Pellegrin, A. Morse, and J. Bandy, "Emerging pollutants," *Water Environment Research*, vol. 83, no. 10, pp. 1906–1984, 10 2011.

[39] T. Salthammer, "Emerging indoor pollutants," *International Journal of Hygiene and Environmental Health*, vol. 224, p. 113423, 2020.

[40] A. L. Tasca, D. Clematis, E. Stefanelli, M. Panizza, and M. Puccini, "Ciprofloxacin removal: Bdd anode coupled with solid polymer electrolyte and ultrasound irradiation," *Journal of Water Process Engineering*, vol. 33, p. 101074, 2020.

[41] S. A. Al-Saydeh, M. H. El-Naas, and S. J. Zaidi, "Copper removal from industrial wastewater: A comprehensive review," *Journal of Industrial and Engineering Chemistry*, vol. 56, pp. 35–44, 12 2017.

[42] P. B. Tchounwou, C. G. Yedjou, A. K. Patlolla, and D. J. Sutton, "Heavy Metal Toxicity and the Environment," *Molecular, Clinical and Environmental Toxicology*, pp. 133–164, 2012.

[43] D. J. Fitzgerald, "Safety guidelines for copper in water." *The American Journal of Clinical Nutrition*, 1998.

[44] A. Galvão and J. S. Matos, "Sustentabilidade de pequenos sistemas de tratamento de Águas residuais," *Associacao Portuguesa dos Recursos Hidricos*, 2004.

[45] B. Mandal, A. Purkayastha, A. A. Prabhu, and V. V. Dasu, *Development in wastewater treatment plant design*, M. P. Shah, S. Rodriguez-Couto, and S. S. Şengör, Eds. Elsevier, 2020. [Online]. Available: https://www.sciencedirect.com/science/article/pii/B9780128198605000134

[46] B. Koul, D. Yadav, S. Singh, M. Kumar, and M. Song, "Insights into the domestic wastewater treatment (dwwt) regimes: A review," *Water*, vol. 14, no. 21, 2022.

[47] M. Amin and G. Bazedi, "Chemical enhanced primary: Treatment of wastewater," *European Journal of Engineering and Technology Research*, 05 2019.

[48] S. Ameta and R. Ameta, *Advanced Oxidation Processes for Wastewater Treatment: Emerging Green Chemical Technology*. Elsevier Science, 2018. [Online]. Available: https://books.google.pt/books?id=hyk0DwAAQBAJ

[49] L. K. Wang, M.-H. S. Wang, N. K. Shammas, and H. H. Hahn, *Physicochemical Treatment Consisting of Chemical Coagulation, Precipitation, Sedimentation, and Flotation*. Cham: Springer International Publishing, 2021, pp. 265–397.

[50] D.-H. Kwak, T.-G. Kim, and M.-S. Kim, "Flotation of cyanobacterial particles without chemical coagulant under auto-flocculation," *Membrane Water Treatment*, 2018.

[51] I. Szilagyi, A. Sadeghpour, and M. Borkovec, "Destabilization of colloidal suspensions by multivalent ions and polyelectrolytes: From screening to overcharging," *Langmuir*, vol. 28, no. 17, pp. 6756–6765, 2012.

[52] C. Y. Teh, P. M. Budiman, K. P. Y. Shak, and T. Y. Wu, "Recent advancement of coagulation–flocculation and its application in wastewater treatment," *Industrial & Engineering Chemistry Research*, vol. 55, no. 16, pp. 4363–4389, 2016.

[53] G. Boczkaj and A. Fernandes, "Wastewater treatment by means of advanced oxidation processes at basic ph conditions: A review," *Chemical Engineering Journal*, vol. 320, pp. 608–633, 2017.

[54] Q. U. Jiuhui, "Research progress of novel adsorption processes in water purification: A review," *Journal of Environmental Sciences*, vol. 20, pp. 1–13, 2008.

[55] N. M. Mahmoodi, M. Taghizadeh, A. Taghizadeh, J. Abdi, B. Hayati, and A. A. Shekarchi, "Bio-based magnetic metal-organic framework nanocomposite: Ultrasound-assisted synthesis and pollutant

(heavy metal and dye) removal from aqueous media," *Applied Surface Science*, vol. 480, pp. 288–299, 2019.

[56] W. S. Chai, J. Y. Cheun, P. S. Kumar, M. Mubashir, Z. Majeed, F. Banat, S.-H. Ho, and P. L. Show, "A review on conventional and novel materials towards heavy metal adsorption in wastewater treatment application," *Journal of Cleaner Production*, vol. 296, p. 126589, 2021.

[57] V. Bobade and N. Eshtiagi, "Heavy metals removal from wastewater by adsorption process: A review," in *Asia Pacific Confederation of Chemical Engineering Congress*, 2015.

[58] A. Ameri, S. Tamjidi, F. Dehghankhalili, A. Farhadi, and M. Saati, "Application of algae as low cost and effective bio-adsorbent for removal of heavy metals from wastewater: a review study," *Environmental Technology Reviews*, vol. 9, pp. 85–110, 12 2020.

[59] S. M. Gawande, N. S. Belwalkar, and A. A. Mane, "Adsorption and its isotherm – theory," *International Journal of Engineering Research and*, 2017.

[60] A. Tripathi and M. R. Ranjan, "Heavy metal removal from wastewater using low cost adsorbents," *J Bioremed Biodeg*, vol. 6, no. 6, p. 315, 2015.

[61] D. Shahidi, R. Roy, and A. Azzouz, "Advances in catalytic oxidation of organic pollutants – prospects for thorough mineralization by natural clay catalysts," *Applied Catalysis B: Environmental*, vol. 174-175, pp. 277–292, 2015.

[62] W. H. Glaze and J. W. Kang, "Advanced oxidation processes. test of a kinetic model for the oxidation of organic compounds with ozone and hydrogen peroxide in a semibatch reactor," *Industrial & Engineering Chemistry Research*, vol. 28, no. 11, pp. 1580–1587, 1989.

[63] M. Antonopoulou, E. Evgenidou, D. Lambropoulou, and I. Konstantinou, "A review on advanced oxidation processes for the removal of taste and odor compounds from aqueous media," *Water Research*, vol. 53, pp. 215–234, 2014.

[64] V. Vikulina and P. Vikulin, "Sedimentation of suspended solids in ultrasound field," *MATEC Web Conf.*, vol. 144, 2018.

[65] L. Z. Ma, Z. Y. Wang, J. M. Guo, Q. F. Cui, M. H. Liu, and Y. J. Zhang, "Treating the eutrophic water by ultrasonic – flocculation sedimentation," *Advanced Materials Research*, vol. 662, pp. 445–449, 2013.

[66] F. Özyonar, Ömür Gökkuş, and M. Sabuni, "Removal of disperse and reactive dyes from aqueous solutions using ultrasound-assisted electrocoagulation," *Chemosphere*, vol. 258, p. 127325, 11 2020.

[67] A. Trujillo-Ortega, S. M. Delgadillo, V. Mendoza-Escamilla, M. May-Lozano, and C. Barrera-Diaz, "Modeling the removal of indigo dye from aqueous media in a sonoelectrochemical flow reactor," *International Journal of Electrochemical Science*, vol. 8, no. 3, pp. 3876–3887, 2013.

[68] H. Oza, T. Anantha Singh, and S. Sasikumar Jampa, "Removal of arsenic from aqueous solution using combined ultrasonic and electrocoagulation process," *Materials Today: Proceedings*, vol. 47, pp. 728–732, 2021.

[69] S. A. Fast and V. G. Gude, "Ultrasound-chitosan enhanced flocculation of low algal turbid waters," *Journal of Industrial and Engineering Chemistry*, 2015.

[70] H. Duckhouse, T. Mason, S. Phull, and J. Lorimer, "The effect of sonication on microbial disinfection using hypochlorite," *Ultrasonics Sonochemistry*, vol. 11, no. 3, pp. 173–176, 2004, 4th Conference on the Applications of Power Ultrasound in Physical and Chemical Processing.

[71] X. Zhou, J. Zhao, Z. Li, J. Lan, Y. Li, X. Yang, and D. Wang, "Influence of ultrasound enhancement on chlorine dioxide consumption and disinfection by-products formation for secondary effluents disinfection," *Ultrasonics Sonochemistry*, vol. 28, pp. 376–381, jan 2016.

[72] S. Phull, A. Newman, J. Lorimer, B. Pollet, and T. Mason, "The development and evaluation of ultrasound in the biocidal treatment of water," *Ultrasonics Sonochemistry*, vol. 4, no. 2, pp. 157–164, 1997, fifth Meeting of the European Society of Sonochemistry.

[73] L. Stępniak and E. Stańczyk-Mazanek, "Ultrasonic energy as an agent to aid water treatment in the coagulation process," *Energies*, vol. 15, no. 14, p. 5186, 7 2022.

[74] B.-M. Jun, S. Kim, H. Rho, C. M. Park, and Y. Yoon, "Ultrasound-assisted ti3c2tx mxene adsorption of dyes: Removal performance and mechanism analyses via dynamic light scattering," *Chemosphere*, vol. 254, p. 126827, 2020.

[75] E. A. Dil, M. Ghaedi, and A. Asfaram, "The performance of nanorods material as adsorbent for removal of azo dyes and heavy metal ions: Application of ultrasound wave, optimization and modeling," *Ultrasonics Sonochemistry*, vol. 34, pp. 792–802, 2017.

[76] A. Asfaram, M. Ghaedi, S. Hajati, A. Goudarzi, and A. A. Bazrafshan, "Simultaneous ultrasound-assisted ternary adsorption of dyes onto copper-doped zinc sulfide nanoparticles loaded on activated carbon: Optimization by response surface methodology," *Spectrochimica Acta Part A: Molecular and Biomolecular Spectroscopy*, vol. 145, pp. 203–212, 2015.

[77] J. Abdi, M. Vossoughi, N. M. Mahmoodi, and I. Alemzadeh, "Synthesis of amine-modified zeolitic imidazolate framework-8, ultrasound-assisted dye removal and modeling," *Ultrasonics Sonochemistry*, vol. 39, pp. 550–564, 2017.

[78] S. A. Sadat, A. M. Ghaedi, M. Panahimehr, M. M. Baneshi, A. Vafaei, and M. Ansarizadeh, "Rapid room-temperature synthesis of cadmium zeolitic imidazolate framework nanoparticles based on 1,1-carbonyldiimidazole as ultra-high-efficiency adsorbent for ultrasound-assisted removal of malachite green dye," *Applied Surface Science*, vol. 467-468, pp. 1204–1212, 2019.

[79] M. Oveisi, M. A. Asli, and N. M. Mahmoodi, "Mil-ti metal-organic frameworks (mofs) nanomaterials as superior adsorbents: Synthesis and ultrasound-aided dye adsorption from multicomponent wastewater systems," *Journal of Hazardous Materials*, vol. 347, pp. 123–140, 2018.

[80] S. Dashamiri, M. Ghaedi, A. Asfaram, F. Zare, and S. Wang, "Multi-response optimization of ultrasound assisted competitive adsorption of dyes onto cu (oh)2-nanoparticle loaded activated carbon: Central composite design," *Ultrasonics Sonochemistry*, vol. 34, pp. 343–353, 2017.

[81] A. Olushola, M. Amoo, A. Omolola, O. Oketayo, and S. Nelana, "Ultrasonic degradation of ciprofloxacin in the presence of zinc oxide nanoparticles and zinc oxide/acha waste composite," *Research Journal of Chemistry and Environment*, vol. 27, no. 1, pp. 22–28, 1 2023.

[82] R. A. Al-Juboori and N. Hilal, "Pharmaceuticals removal from wastewater: Ultrasound technology and its potential amalgamation with membrane processes," *Journal of Water Process Engineering*, vol. 53, p. 103810, 2023.

[83] R. S. Sutar and V. K. Rathod, "Ultrasound assisted laccase catalyzed degradation of ciprofloxacin hydrochloride," *Journal of Industrial and Engineering Chemistry*, vol. 31, pp. 276–282, 2015.

[84] G. Z. Kyzas, N. Mengelizadeh, M. K. Saloot, S. Mohebi, and D. Balarak, "Sonochemical degradation of ciprofloxacin by hydrogen peroxide and persulfate activated by ultrasound and ferrous ions," *Colloids and Surfaces A: Physicochemical and Engineering Aspects*, vol. 642, p. 128627, 2022.

[85] S. Chakma, P. K. Dikshit, M. N. Galodiya, A. S. Giri, and V. S. Moholkar, "The role of ultrasound in enzymatic degradation mechanism," *Journal of the Taiwan Institute of Chemical Engineers*, vol. 107, pp. 54–71, 2020.

[86] E. D. Bel, J. Dewulf, B. D. Witte, H. V. Langenhove, and C. Janssen, "Influence of ph on the sonolysis of ciprofloxacin: Biodegradability, ecotoxicity, and antibiotic activity of its degradation products," *Chemosphere*, vol. 77, no. 2, pp. 291–295, September 2009.

[87] A. Igwegbe, S. Ahmadi, S. Rahdar, A. Ramazani, and A. R. Mollazehi, "Efficiency comparison of advanced oxidation processes for ciprofloxacin removal from aqueous solutions: Sonochemical, sono-nano-chemical and sono-nano-chemical/persulfate processes," *Environmental Engineering Research*, vol. 25, no. 2, pp. 178–185, 4 2020.

[88] H. Gupta and P. R. Gogate, "Intensified removal of copper from waste water using activated watermelon based biosorbent in the presence of ultrasound," *Ultrasonics Sonochemistry*, vol. 30, pp. 113–122, 5 2016.

[89] M. Secondes, V. Naddeo, F. Ballesteros Jr, and V. Belgiorno, "Adsorption of emerging contaminants enhanced by ultrasound irradiation," *Sustainable Environment Research*, vol. 24, pp. 349–355, 05 2014.

[90] H. R. Campos and P. E. Wheat, "Ultrasound-enhanced copper removal by hydrous iron oxide adsorption," in *Conference: 9. Annual conference on hazardous waste remediation*. Kansas State Univ., Manhattan, KS (United States), 1996.

[91] Z. Danková, A. Bekényiová, I. Štyriaková, and E. Fedorová, "Study of cu(ii) adsorption by siderite and kaolin," *Procedia Earth and Planetary Science*, vol. 15, pp. 821–826, 2015.

[92] G. Rossi, M. Mainardis, E. Aneggi, L. K. Weavers, and D. Goi, "Combined ultrasound-ozone treatment for reutilization of primary effluent—a preliminary study," *Environmental Science and Pollution Research*, vol. 28, no. 1, pp. 700–710, 1 2021.

[93] A. Arka, C. Dawit, A. Befekadu, S. K. Debela, and P. Asaithambi, "Wastewater treatment using sono-electrocoagulation process: optimization through response surface methodology," *Sustainable Water Resources Management*, vol. 8, no. 3, p. 61, 6 2022.

[94] E. A. Serna-Galvis, A. M. Botero-Coy, D. Martínez-Pachón, A. Moncayo-Lasso, M. Ibáñez, F. Hernández, and R. A. Torres-Palma, "Degradation of seventeen contaminants of emerging

concern in municipal wastewater effluents by sonochemical advanced oxidation processes," *Water Research*, vol. 154, pp. 349–360, 5 2019.

[95] E. A. Serna-Galvis, J. Silva-Agredo, A. M. Botero-Coy, A. Moncayo-Lasso, F. Hernández, and R. A. Torres-Palma, "Effective elimination of fifteen relevant pharmaceuticals in hospital wastewater from colombia by combination of a biological system with a sonochemical process," *Science of The Total Environment*, vol. 670, pp. 623–632, 2019.

[96] S. Chandak, P. K. Ghosh, and P. R. Gogate, "Treatment of real pharmaceutical wastewater using different processes based on ultrasound in combination with oxidants," *Process Safety and Environmental Protection*, vol. 137, pp. 149–157, 2020.

[97] N. A. Fetyan and T. M. S. Attia, "Water purification using ultrasound waves: application and challenges," *Arab Journal of Basic and Applied Sciences*, vol. 27, no. 1, pp. 194–207, 1 2020.

[98] C. Brennen, *Cavitation and Bubble Dynamics*, ser. Oxford engineering science series. Oxford University Press, 1995. [Online]. Available: https://books.google.pt/books?id=vYiUO0RIC4UC

[99] J. Franc and J. Michel, *Fundamentals of Cavitation*, ser. Fluid Mechanics and Its Applications. Springer Netherlands, 2006. [Online]. Available: https://books.google.pt/books?id=QJOQYa_oo24C

[100] M. Vukalovich, *Thermodynamic Properties of Water and Steam: Tables and Diagram*. Freud Publishing House, 1973. [Online]. Available: https://books.google.pt/books?id=JHlTPQAACAAJ

[101] C. Yi, Q. Lu, Y. Wang, Y. Wang, and B. Yang, "Degradation of organic wastewater by hydrodynamic cavitation combined with acoustic cavitation," *Ultrasonics Sonochemistry*, vol. 43, pp. 156–165, 5 2018.

[102] T. Mason, *Advances in Sonochemistry*, ser. Advances in Sonochemistry. Elsevier Science, 1999, no. vol. 5. [Online]. Available: https://books.google.pt/books?id=ORayryzBEdQC

[103] M. Ashokkumar, J. Lee, S. Kentish, and F. Grieser, "Bubbles in an acoustic field: An overview," *Ultrasonics Sonochemistry*, vol. 14, no. 4, pp. 470–475, 2007.

[104] M. Ashokkumar, "The characterization of acoustic cavitation bubbles - an overview," *Ultrasonics Sonochemistry*, vol. 18, no. 4, pp. 864–872, 2011.

[105] T. Mason, *High Powered Ultrasound in Physical and Chemical Processing*. Biblioteca de Ciecias, 01 2003, pp. 105–138.

[106] T. Mason and D. Peters, *Practical Sonochemistry: Power Ultrasound Uses and Applications*. Woodhead, 01 2002.

[107] B. Pollet and M. Ashokkumar, *Introduction to Ultrasound, Sonochemistry and Sonoelectrochemistry*, ser. SpringerBriefs in molecular science: Ultrasound and sonochemistry. Springer, 2019. [Online]. Available: https://books.google.pt/books?id=y0E-zQEACAAJ

[108] M. R. Doosti, R. Kargar, and M. H. Sayadi, "Water treatment using ultrasonic assistance: A review," *Proceedings of the International Academy of Ecology and Environmental Sciences*, vol. 2, no. 2, pp. 96–110, 2012.

[109] S. Ameta, R. Ameta, and G. Ameta, *Sonochemistry: An Emerging Green Technology*. Apple Academic Press, 2018. [Online]. Available: https://books.google.pt/books?id=5jL3DwAAQBAJ

[110] A. H. Mahvi, "Application of ultrasonic technology for water and wastewater treatment," *Iranian J Publ Health*, vol. 38, no. 2, pp. 1–17, 2009.

[111] J. Carpenter, M. Badve, S. Rajoriya, S. George, V. Saharan, and A. Pandit, "Hydrodynamic cavitation: An emerging technology for the intensification of various chemical and physical processes in a chemical process industry," *Reviews in Chemical Engineering*, vol. 33, 01 2016.

[112] V. V. Goncharuk, V. V. Malyarenko, and V. A. Yaremenko, "Use of ultrasound in water treatment," *Journal of Water Chemistry and Technology*, vol. 30, no. 3, pp. 137–150, 6 2008.

[113] E. Nie, M. Yang, D. Wang, X. Yang, X. Luo, and Z. Zheng, "Degradation of diclofenac by ultrasonic irradiation: Kinetic studies and degradation pathways," *Chemosphere*, vol. 113, pp. 165–170, 2014.

[114] S. Merouani, O. Hamdaoui, Y. Rezgui, and M. Guemini, "Theoretical estimation of the temperature and pressure within collapsing acoustical bubbles," *Ultrasonics Sonochemistry*, vol. 21, no. 1, pp. 53–59, 2014.

[115] V. Misik, N. Miyoshi, and P. Riesz, "Epr spin-trapping study of the sonolysis of h2o/d2o mixtures: Probing the temperatures of cavitation regions," *The Journal of Physical Chemistry*, vol. 99, no. 11, pp. 3605–3611, 1995.

[116] M. Dular, T. Griessler-Bulc, I. Gutierrez-Aguirre, E. Heath, T. Kosjek, A. K. Klemenčič, M. Oder, M. Petkovšek, N. Rački, M. Ravnikar, A. Šarc, B. Širok, M. Zupanc, M. Žitnik, and B. Kompare, "Use of hydrodynamic cavitation in (waste)water treatment," *Ultrasonics Sonochemistry*, vol. 29, pp. 577–588, 3 2016.

[117] N. Matei and D. Scarpete, "Treatment of wastewater by ultrasound intensity and frequency effect: A review," *ARPN Journal of Science and Technology*, vol. 5, no. 11, 2015.

[118] M. P. Rayaroth, U. K. Aravind, and C. T. Aravindakumar, "Sonochemical degradation of coomassie brilliant blue: Effect of frequency, power density, ph and various additives," *Chemosphere*, vol. 119, pp. 848–855, 2015.

[119] E. A. Serna-Galvis, J. Silva-Agredo, A. L. Giraldo-Aguirre, O. A. Flórez-Acosta, and R. A. Torres-Palma, "High frequency ultrasound as a selective advanced oxidation process to remove penicillinic antibiotics and eliminate its antimicrobial activity from water," *Ultrasonics Sonochemistry*, vol. 31, pp. 276–283, 2016.

[120] E. Psillakis, D. Mantzavinos, and N. Kalogerakis, "Monitoring the sonochemical degradation of phthalate esters in water using solid-phase microextraction," *Chemosphere*, vol. 54, no. 7, pp. 849–857, 2004.

[121] A. Al-Bsoul, M. Al-Shannag, M. Tawalbeh, A. A. Al-Taani, W. K. Lafi, A. Al-Othman, and M. Alsheyab, "Optimal conditions for olive mill wastewater treatment using ultrasound and advanced oxidation processes," *Science of the Total Environment*, vol. 700, 1 2020.

[122] J.-W. Kang, H.-M. Hung, A. Lin, and M. R. Hoffmann, "Sonolytic destruction of methyl tertbutyl ether by ultrasonic irradiation: The role of o3, h2o2, frequency, and power density," *Environmental Science & Technology*, vol. 33, no. 18, pp. 3199–3205, 1999.

[123] R. Xiao, D. Diaz-Rivera, and L. K. Weavers, "Factors influencing pharmaceutical and personal care product degradation in aqueous solution using pulsed wave ultrasound," *Industrial & Engineering Chemistry Research*, vol. 52, no. 8, pp. 2824–2831, 2013.

[124] R. Xiao, Z. Wei, D. Chen, and L. K. Weavers, "Kinetics and mechanism of sonochemical degradation of pharmaceuticals in municipal wastewater," *Environmental Science & Technology*, vol. 48, no. 16, pp. 9675–9683, 2014, pMID: 25026248.

[125] V. S. Sutkar and P. R. Gogate, "Design aspects of sonochemical reactors: Techniques for understanding cavitational activity distribution and effect of operating parameters," *Chemical Engineering Journal*, vol. 155, no. 1, pp. 26–36, 2009.

[126] S. Goskonda, J. Catallo, and T. Junk, "Sonochemical degradation of aromatic organic pollutants," *Waste Management*, vol. 22, no. 3, pp. 351–356, 2002.

[127] Y. Jiang, C. Petrier, and T. D. Waite, "Sonolysis of 4-chlorophenol in aqueous solution: Effects of substrate concentration, aqueous temperature and ultrasonic frequency," *Ultrasonics Sonochemistry*, vol. 13, no. 5, pp. 415–422, 2006.

[128] J. Lorimer, T. Mason, T. Cuthbert, and E. Brookfield, "Effect of ultrasound on the degradation of aqueous native dextran," *Ultrasonics Sonochemistry*, vol. 2, no. 1, pp. S55–S57, 1995.

[129] Y. Zhang, Y. Hou, F. Chen, Z. Xiao, J. Zhang, and X. Hu, "The degradation of chlorpyrifos and diazinon in aqueous solution by ultrasonic irradiation: Effect of parameters and degradation pathway," *Chemosphere*, vol. 82, no. 8, pp. 1109–1115, 2011.

[130] K. Brabec and V. Mornstein, "Detection of ultrasonic cavitation based on low-frequency analysis of acoustic signal," *Central European Journal of Biology*, vol. 2, pp. 213–221, 2007.

[131] T. Rossing, R. Moore, and P. Wheeler, *The science of sound*, 3rd ed. Pearson Education Limited, 2001.

[132] G. Chatel, *Sonochemistry: New Opportunities For Green Chemistry*. World Scientific Publishing Company, 2016. [Online]. Available: https://books.google.pt/books?id=rkQyDwAAQBAJ

[133] D. Williams, "The physics of ultrasound," *Anaesthesia and Intensive Care Medicine*, vol. 13, no. 6, pp. 264–268, 6 2012.

[134] S. Głowniak, B. Szczęśniak, J. Choma, and M. Jaroniec, "Recent developments in sonochemical synthesis of nanoporous materials," *Molecules*, vol. 28, no. 6, 2023.

[135] A. Peshkovsky and S. Peshkovsky, *Acoustic Cavitation Theory and Equipment Design Principles for Industrial Applications of High-intensity Ultrasound*, ser. Physics research and technology. Nova Science Publishers, 2010. [Online]. Available: https://books.google.pt/books?id=seXFcQAACAAJ

[136] T. J. Mason and J. P. Lorimer, *Applied Sonochemistry - The Uses of Power Ultrasound in Chemistry and Processing*. Wiley, 4 2002.

[137] N. Matei and D. Scarpete, "The use of ultrasound in the treatment process of wastewater: A review," *The Annals Of "Dunarea De Jos" University Of Galati Fascicle IX. Metallurgy And Materials Science*, vol. Nª 2, pp. 45–50, 2015.

[138] C. Sikalidis, *Advances in Ceramics - Electric and Magnetic Ceramics, Bioceramics, Ceramics and Environment*. Rijeka: IntechOpen, Sep 2011. [Online]. Available: https://doi.org/10.5772/726

[139] M. Vijaya, *Piezoelectric Materials and Devices: Applications in Engineering and Medical Sciences*. CRC Press, 2016. [Online]. Available: https://books.google.pt/books?id=nBTSBQAAQBAJ

[140] C. Steinem and A. Janshoff, Eds., *Piezoelectric Sensors*. Springer Berlin Heidelberg, 2007, vol. 5.

[141] A. Roy, D. Dwari, M. K. Ram, and P. Datta, *Piezoelectric nanomaterials for biomedical applications*. Elsevier, 2022.

[142] A. Safari and K. Akdogan, *Piezoelectric and Acoustic Materials for Transducer Applications*. Springer New York, NY, 2008.

[143] J. Price, "Acoustic waveguides," 2008.

[144] Y. E. Kwon, H. J. Jeon, H. W. Kim, and Y. Y. Kim, "Waveguide tapering for beam-width control in a waveguide transducer," *Ultrasonics*, vol. 54, no. 3, pp. 953–960, 2014.

[145] H. Esmer Duruel, G. Kaymak, S. Tartar, and F. Kayhan, "An application of ultrasound for water treatment: A different approach to treatment methods." *Çanakkale Onsekiz Mart University, Journal of Graduate School of Natural and Applied Sciences.*, vol. 2, pp. 84–110, 05 2016.

[146] B. Verhaagen and D. F. Rivas, "Measuring cavitation and its cleaning effect," *Ultrasonics Sonochemistry*, vol. 29, pp. 619–628, 3 2016.

[147] E. C. Gelderblom, H. J. Vos, F. Mastik, T. Faez, Y. Luan, T. J. Kokhuis, A. F. van der Steen, D. Lohse, N. de Jong, and M. Versluis, "Brandaris 128 ultra-high-speed imaging facility: 10 years of operation, updates, and enhanced features," *Review of Scientific Instruments*, vol. 83, no. 10, p. 103706, 2012.

[148] A. Zijlstra, D. F. Rivas, H. J. Gardeniers, M. Versluis, and D. Lohse, "Enhancing acoustic cavitation using artificial crevice bubbles," *Ultrasonics*, vol. 56, pp. 512–523, 2015.

[149] A. Soare, R. Dijkink, M. R. Pascual, C. Sun, P. W. Cains, D. Lohse, A. I. Stankiewicz, and H. J. M. Kramer, "Crystal nucleation by laser-induced cavitation," *Crystal Growth & Design*, vol. 11, no. 6, pp. 2311–2316, 2011.

[150] J. R. Sukovich, S. C. Haskell, Z. Xu, and T. L. Hall, "A cost-effective, multi-flash, "ghost" imaging technique for high temporal and spatial resolution imaging of cavitation using "still-frame" cameras," *The Journal of the Acoustical Society of America*, vol. 147, no. 3, pp. 1339–1343, 03 2020.

[151] J. Fuchs and B. N. Ultrasonics, "Ultrasonic intensity measurement techniques," in *CleanTech Symposium Proceedings, Witter Publications*, 2002.

[152] C. D. Arvanitis and N. McDannold, "Integrated ultrasound and magnetic resonance imaging for simultaneous temperature and cavitation monitoring during focused ultrasound therapies," *Medical Physics*, vol. 40, no. 11, p. 112901, 10 2013.

[153] P. de Santis, D. Sette, and F. Wanderlingh, "Cavitation detection: The use of the subharmonics," *Journal of the Acoustical Society of America*, vol. 42, pp. 514–516, 1967.

[154] R. E. Apfel, "Acoustic cavitation," in *Ultrasonics*, ser. Methods in Experimental Physics, P. D. Edmonds, Ed. Academic Press, 1981, vol. 19, pp. 355–411. [Online]. Available: https://www.sciencedirect.com/science/article/pii/S0076695X08603385

[155] H. Puga, J. Barbosa, J. Gabriel, E. Seabra, S. Ribeiro, and M. Prokic, "Evaluation of ultrasonic aluminium degassing by piezoelectric sensor," *Journal of Materials Processing Technology*, vol. 211, no. 6, pp. 1026–1033, 2011.

[156] S. Rupitsch, *Piezoelectric Sensors and Actuators: Fundamentals and Applications*, ser. Topics in Mining, Metallurgy and Materials Engineering. Springer Berlin Heidelberg, 2018. [Online]. Available: https://books.google.pt/books?id=2JdmDwAAQBAJ

[157] J. Hujer and M. Müller, "Calibration of pvdf film transducers for the cavitation impact measurement," *EPJ Web of Conferences*, vol. 180, p. 02036, 6 2018.

[158] L. Htet, "Calibration of piezoelectric film sensors for the cavitation aggressiveness measurement," 6 2020.

[159] Y.-C. Wang and Y.-W. Chen, "Application of piezoelectric pvdf film to the measurement of impulsive forces generated by cavitation bubble collapse near a solid boundary," *Experimental Thermal and Fluid Science*, vol. 32, no. 2, pp. 403–414, 2007.

[160] G. Eskin and D. Eskin, *Ultrasonic Treatment of Light Alloy Melts*, ser. Advances in Metallic Alloys. CRC Press, 2017. [Online]. Available: https://books.google.ch/books?id=ePPctAEACAAJ

[161] O. V. Abramov, *High-Intensity Ultrasonics*, 1st ed. CRC Press, 1999.

[162] L. Bai, W. Xu, J. Deng, C. Li, D. Xu, and Y. Gao, "Generation and control of acoustic cavitation structure," *Ultrasonics Sonochemistry*, vol. 21, no. 5, pp. 1696–1706, 2014.

[163] A. Moussatov, C. Granger, and B. Dubus, "Cone-like bubble formation in ultrasonic cavitation field," *Ultrasonics Sonochemistry*, vol. 10, no. 4, pp. 191–195, 2003, selected papers from the Eighth Conference of the European Society of Sonochemistry.

[164] T. P. Silverstein, "The real reason why oil and water don't mix," *Journal of Chemical Education*, vol. 75, no. 1, p. 116, 1998.

[165] C.-C. He, C.-Y. Hu, and S.-L. Lo, "Integrating chloride addition and ultrasonic processing with electrocoagulation to remove passivation layers and enhance phosphate removal," *Separation and Purification Technology*, vol. 201, pp. 148–155, 2018.

[166] M. P. Rayaroth, U. K. Aravind, and C. T. Aravindakumar, "Degradation of pharmaceuticals by ultrasound-based advanced oxidation process," *Environmental Chemistry Letters*, vol. 14, no. 3, pp. 259–290, 9 2016.

[167] A. V. Karim and A. Shriwastav, "Degradation of amoxicillin with sono, photo, and sonophotocatalytic oxidation under low-frequency ultrasound and visible light," *Environmental Research*, vol. 200, p. 111515, 2021.

Appendix A - Piezoelectric Datasheet

The piezoelectric sensor was manufacture by the Hangzhou Altrasonic Technology Co., Ltd. that provided the sensor parameter table present on Figure A.1.

Model	Dimensions (mm)		Main performance		
	D	T	Fr (KHz)	Kp (%)	C (pF)
HS-PC40	50	2.0	40	40	11000

Main performance parameters:

1. Resonant frequency(Fr):
   Fr1=44±2KHz (Note 1)
   Fr1=1000±100KHz (Note 1)
2. Resonant impedance(Ro) :
   Ro=max. 10Ω (Note 1)
3. Direct capacitance(Cp):
   Cp=11000±20%pf (Note 2)
4. Electromechanical coupling coefficient (Kt, Kp):
   Kp=min. 40%
5. Mechanical quality factor (Qm):
   Qm=min. 100
6. Induced loss(tanδ):
   tanδ=max. 0.5%

7. Working voltage: VPP40~500V

8. Operating temperature range: -5°C~+80°C

Note1: Measured by Hp-4194A at 25°C 80%R.H
Note2: Measured by LCR meter at 1KHz,1Vrms

Figure A.1: Data-sheet of the piezoelectric device provided by the manufacturer.

Appendix B - Calibration Extended Data of Sensors 2 and 3

Table B.1: Experimental data of sensor 2 and corresponding calibration results with the 0.30 g sphere.

$\Delta t(\mu m)$	$V(V)$	$h2(mm)$	$h1(mm)$	$v1(m/s)$	$v2(m/s)$	$m(kg)$	$F_{avg}(N)$
36	0.43	18	50	0.99	0.59	0.30	13.43
36	0.42	20	50	0.99	0.63	0.30	13.70
36	0.43	15	50	0.99	0.54	0.30	12.99
36	0.40	16	50	0.99	0.56	0.30	13.14
36	0.45	17	50	0.99	0.58	0.30	13.28
36	0.80	45	100	1.40	0.94	0.30	19.83
36	0.80	45	100	1.40	0.94	0.30	19.83
36	0.75	43	100	1.40	0.92	0.30	19.65
36	0.78	43	100	1.40	0.92	0.30	19.65
36	0.75	42	100	1.40	0.91	0.30	19.56
36	0.91	48	170	1.83	0.97	0.30	23.69
36	0.90	47	170	1.83	0.96	0.30	23.61
36	0.96	49	170	1.83	0.98	0.30	23.78
36	0.97	46	170	1.83	0.95	0.30	23.52
36	0.93	50	170	1.83	0.99	0.30	23.86
36	1.25	54	270	2.30	1.03	0.30	28.22
36	1.23	50	270	2.30	0.99	0.30	27.89
36	1.24	54	270	2.30	1.03	0.30	28.22
36	1.21	48	270	2.30	0.97	0.30	27.72
36	1.22	48	270	2.30	0.97	0.30	27.72
36	1.40	53	370	2.69	1.02	0.30	31.47
36	1.48	63	370	2.69	1.11	0.30	32.25
36	1.41	54	370	2.69	1.03	0.30	31.55
36	1.48	65	370	2.69	1.13	0.30	32.39
36	1.45	58	370	2.69	1.07	0.30	31.86
36	1.64	65	500	3.13	1.13	0.30	36.10
36	1.69	62	500	3.13	1.10	0.30	35.88

Continued on next page

Table B.1 – continued from previous page

$\Delta t(\mu m)$	$V(V)$	$h2(mm)$	$h1(mm)$	$v1(m/s)$	$v2(m/s)$	$m(kg)$	$F_{avg}(N)$
36	1.66	68	500	3.13	1.16	0.30	36.32
36	1.65	66	500	3.13	1.14	0.30	36.18
36	1.65	64	500	3.13	1.12	0.30	36.03

Table B.2: Experimental data from sensor 2 and corresponding calibration results with the 2.02 grams sphere.

$\Delta t(\mu m)$	$V(V)$	$h2(mm)$	$h1(mm)$	$v1(m/s)$	$v2(m/s)$	$m(kg)$	$F_{avg}(N)$
60	1.46	12	50	0.99	0.49	2.02	49.68
60	1.46	13	50	0.99	0.51	2.02	50.35
60	1.49	14	50	0.99	0.52	2.02	50.99
60	1.45	12	50	0.99	0.49	2.02	49.68
60	1.42	10	50	0.99	0.44	2.02	48.26
60	1.46	12	50	0.99	0.49	2.02	49.68
60	1.46	13	50	0.99	0.51	2.02	50.35
60	1.49	14	50	0.99	0.52	2.02	50.99
60	1.45	12	50	0.99	0.49	2.02	49.68
60	1.42	10	50	0.99	0.44	2.02	48.26
60	4.12	50	170	1.83	0.99	2.02	94.83
60	4.17	45	170	1.83	0.94	2.02	93.12
60	4.25	48	170	1.83	0.97	2.02	94.16
60	4.10	48	170	1.83	0.97	2.02	94.16
60	4.15	52	170	1.83	1.01	2.02	95.49

Table B.3: Experimental data from sensor 2 and corresponding calibration results with the 0.88 grams sphere.

$\Delta t(\mu m)$	$V(V)$	$h2(mm)$	$h1(mm)$	$v1(m/s)$	$v2(m/s)$	$m(kg)$	$F_{avg}(N)$
36	1.84	46	100	1.40	0.95	0.88	57.14
36	1.88	48	100	1.40	0.97	0.88	57.63

Continued on next page

Table B.3 – continued from previous page

$\Delta t(\mu m)$	$V(V)$	$h2(mm)$	$h1(mm)$	$v1(m/s)$	$v2(m/s)$	$m(kg)$	$F_{avg}(N)$
36	1.80	42	100	1.40	0.91	0.88	56.11
36	1.78	48	100	1.40	0.97	0.88	57.63
36	1.82	46	100	1.40	0.95	0.88	57.14
36	1.27	21	50	0.99	0.64	0.88	39.67
36	1.16	22	50	0.99	0.66	0.88	40.04
36	1.13	24	50	0.99	0.69	0.88	40.75
36	1.25	19	50	0.99	0.61	0.88	38.91
36	1.25	20	50	0.99	0.63	0.88	39.30
36	2.58	75	170	1.83	1.21	0.88	73.87
36	2.50	72	170	1.83	1.19	0.88	73.28
36	2.75	73	170	1.83	1.20	0.88	73.48
36	2.80	76	170	1.83	1.22	0.88	74.07
36	2.75	72	170	1.83	1.19	0.88	73.28
36	3.82	100	270	2.30	1.40	0.88	89.99
36	3.61	92	270	2.30	1.34	0.88	88.60
36	3.79	95	270	2.30	1.37	0.88	89.12
36	3.61	94	270	2.30	1.36	0.88	88.95
36	3.88	96	270	2.30	1.37	0.88	89.30
36	4.87	150	370	2.69	1.72	0.88	107.18
36	4.86	142	370	2.69	1.67	0.88	106.06
36	4.60	145	370	2.69	1.69	0.88	106.48
36	4.83	145	370	2.69	1.69	0.88	106.48
36	4.79	140	370	2.69	1.66	0.88	105.77
36	5.52	160	500	3.13	1.77	0.88	119.19
36	5.42	165	500	3.13	1.80	0.88	119.86
36	5.24	162	500	3.13	1.78	0.88	119.46
36	5.45	163	500	3.13	1.79	0.88	119.59
36	5.36	168	500	3.13	1.82	0.88	120.25

Table B.4: Experimental data from sensor 3 and corresponding calibration results with the 0.30 grams sphere.

$\Delta t(\mu m)$	$V(V)$	$h_2(mm)$	$h_1(mm)$	$v_1(m/s)$	$v_2(m/s)$	$m(kg)$	$F_{avg}(N)$
36	0.287	13	50	0.990	0.505	0.30	12.670
36	0.241	12	50	0.990	0.485	0.30	12.502
36	0.235	15	50	0.990	0.542	0.30	12.987
36	0.296	10	50	0.990	0.442	0.30	12.144
36	0.254	11	50	0.990	0.464	0.30	12.327
36	0.423	18	100	1.401	0.594	0.30	16.902
36	0.497	23	100	1.401	0.672	0.30	17.558
36	0.401	20	100	1.401	0.626	0.30	17.174
36	0.476	21	100	1.401	0.642	0.30	17.305
36	0.465	23	100	1.401	0.672	0.30	17.558
36	0.655	32	170	1.826	0.792	0.30	22.186
36	0.759	35	170	1.826	0.829	0.30	22.494
36	0.603	30	170	1.826	0.767	0.30	21.973
36	0.625	36	170	1.826	0.840	0.30	22.593
36	0.707	30	170	1.826	0.767	0.30	21.973
36	0.937	38	270	2.302	0.863	0.30	26.815
36	0.986	40	270	2.302	0.886	0.30	27.005
36	0.901	38	270	2.302	0.863	0.30	26.815
36	0.985	45	270	2.302	0.940	0.30	27.460
36	0.935	42	270	2.302	0.908	0.30	27.191
36	0.903	48	370	2.694	0.970	0.30	31.049
36	0.856	52	370	2.694	1.010	0.30	31.384
36	0.852	52	370	2.694	1.010	0.30	31.384
36	0.926	56	370	2.694	1.048	0.30	31.708
36	0.886	50	370	2.694	0.990	0.30	31.218
36	1.428	93	500	3.132	1.351	0.30	37.980
36	1.456	100	500	3.132	1.401	0.30	38.403

Continued on next page

Table B.4 – continued from previous page

$\Delta t(\mu m)$	$V(V)$	$h_2(mm)$	$h_1(mm)$	$v_1(m/s)$	$v_2(m/s)$	$m(kg)$	$F_{\text{avg}}(N)$
36	1.466	96	500	3.132	1.372	0.30	38.163
36	1.405	90	500	3.132	1.329	0.30	37.794
36	1.435	102	500	3.132	1.415	0.30	38.521

Table B.5: Experimental data from sensor 3 and corresponding calibration results with the 2.02 grams sphere.

$\Delta t(\mu m)$	$V(V)$	$h_2(mm)$	$h_1(mm)$	$v_1(m/s)$	$v_2(m/s)$	$m(kg)$	$F_{\text{avg}}(N)$
60	1.800	8	100	1.401	0.396	2.02	60.495
60	1.966	13	100	1.401	0.505	2.02	64.160
60	1.728	12	100	1.401	0.485	2.02	63.493
60	1.816	10	100	1.401	0.443	2.02	62.070
60	1.925	10	100	1.401	0.443	2.02	62.070
60	1.323	6	50	0.990	0.343	2.02	44.896
60	1.227	5	50	0.990	0.313	2.02	43.890
60	1.237	8	50	0.990	0.396	2.02	46.683
60	1.103	5	50	0.990	0.313	2.02	43.890
60	1.359	5	50	0.990	0.313	2.02	43.890
60	3.622	20	170	1.826	0.626	2.02	82.575
60	3.658	25	170	1.826	0.700	2.02	85.064
60	3.365	24	170	1.826	0.686	2.02	84.588
60	3.326	21	170	1.826	0.642	2.02	83.096
60	3.483	17	170	1.826	0.578	2.02	80.929

Table B.6: Experimental data from sensor 3 and corresponding calibration results with the 0.88 grams sphere.

$\Delta t(\mu m)$	$V(V)$	$h_2(mm)$	$h_1(mm)$	$v_1(m/s)$	$v_2(m/s)$	$m(kg)$	$F_{\text{avg}}(N)$
36	1.586	47	100	1.401	0.960	0.88	57.385
36	1.424	42	100	1.401	0.908	0.88	56.109

Continued on next page

Table B.6 – continued from previous page

$\Delta t(\mu m)$	$V(V)$	$h_2(mm)$	$h_1(mm)$	$v_1(m/s)$	$v_2(m/s)$	$m(kg)$	$F_{\text{avg}}(N)$
36	1.550	45	100	1.401	0.940	0.88	56.883
36	1.457	41	100	1.401	0.897	0.88	55.845
36	1.565	40	100	1.401	0.886	0.88	55.577
36	1.001	21	50	0.990	0.642	0.88	39.675
36	1.052	21	50	0.990	0.642	0.88	39.675
36	1.167	23	50	0.990	0.672	0.88	40.401
36	0.946	18	50	0.990	0.594	0.88	38.518
36	1.888	24	50	0.990	0.686	0.88	40.752
36	2.097	75	170	1.826	1.213	0.88	73.873
36	1.965	73	170	1.826	1.197	0.88	73.478
36	1.976	75	170	1.826	1.213	0.88	73.873
36	2.102	72	170	1.826	1.189	0.88	73.278
36	2.065	70	170	1.826	1.172	0.88	72.874
36	3.036	90	270	2.302	1.329	0.88	88.240
36	2.955	92	270	2.302	1.344	0.88	88.597
36	3.124	84	270	2.302	1.284	0.88	87.145
36	2.906	96	270	2.302	1.372	0.88	89.299
36	2.569	90	270	2.302	1.329	0.88	88.240
36	3.365	140	370	2.694	1.657	0.88	105.770
36	3.659	146	370	2.694	1.692	0.88	106.624
36	3.257	152	370	2.694	1.727	0.88	107.461
36	3.545	142	370	2.694	1.669	0.88	106.057
36	3.254	144	370	2.694	1.681	0.88	106.341
36	4.563	152	500	3.132	1.727	0.88	118.101
36	4.215	159	500	3.132	1.766	0.88	119.057
36	4.127	161	500	3.132	1.777	0.88	119.326
36	4.157	156	500	3.132	1.749	0.88	118.650
36	4.456	165	500	3.132	1.799	0.88	119.859